studies in surface science and catalysis

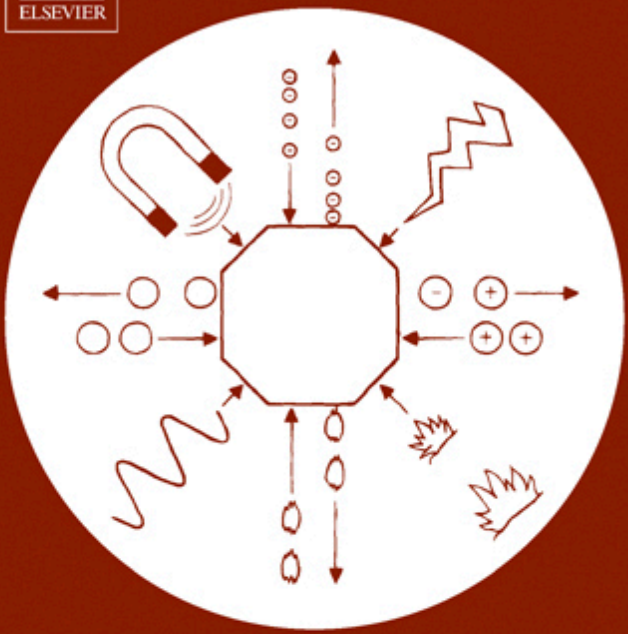

158 A

MOLECULAR SIEVES: FROM BASIC RESEARCH TO INDUSTRIAL APPLICATIONS

J. Čejka
N. Žilková
P. Nachtigall
(editors)

Studies in Surface Science and Catalysis 158 – Part A

MOLECULAR SIEVES: FROM BASIC RESEARCH TO INDUSTRIAL APPLICATIONS

This Page is Intentionally Left Blank

Studies in Surface Science and Catalysis

Advisory Editors: B. Delmon and J.T. Yates
Series Editor: G. Centi

Vol. 158

MOLECULAR SIEVES: FROM BASIC RESEARCH TO INDUSTRIAL APPLICATIONS

PART A

Proceedings of the 3rd International Zeolite Symposium (3rd FEZA), Prague, Czech Republic, August 23-26, 2005

Edited by

J. Čejka
N. Žilková
P. Nachtigall

J. Heyrovsky Institute of Physical Chemistry
Academy of Sciences of the Czech Republic
Prague, Czech Republic

2005

ELSEVIER

Amsterdam – Boston – Heidelberg – London – New York – Oxford – Paris – San Diego
San Francisco – Singapore – Sydney – Tokyo

ELSEVIER B.V.
Radarweg 29
P.O. Box 211, 1000 AE Amsterdam
The Netherlands

ELSEVIER Inc.
525 B Street, Suite 1900
San Diego, CA 92101-4495
USA

ELSEVIER Ltd
The Boulevard, Langford Lane
Kidlington, Oxford OX5 1GB
UK

ELSEVIER Ltd
84 Theobalds Road
London WC1X 8RR
UK

First edition 2005

Library of Congress Cataloging in Publication Data
A catalog record is available from the Library of Congress.

British Library Cataloguing in Publication Data
A catalogue record is available from the British Library.

ISBN: 0 444 52082 1 (Set)
ISBN: 0 444 51670 0 (Part A)
ISBN: 0 444 52083 X (Part B)

The paper used in this publication meets the requirements of ANSI/NISO Z39.48-1992 (Permanence of Paper).
Printed in The Netherlands.

PREFACE

We are pleased to present the Proceedings of the 3rd Conference of the Federation of European Zeolite Associations that has been held in Prague, Czech Republic, from August 23 to 26, 2005. The conference has been organized by The Czech Zeolite Group and the J. Heyrovský Institute of Physical Chemistry under the auspices of the Federation of European Zeolite Associations on the theme "Molecular Sieves: from Basic Research to Industrial Applications".

FEZA was founded in 1995 and included representatives from six European countries with Herman van Bekkum (the Netherlands) as its first president. Now FEZA involves fourteen national zeolite associations and this number is slowly but surely growing. The 1st FEZA Conference on Zeolites was organized by I. Kiricsi (Eger, 1999) followed by the 2nd FEZA Conference organized by R. Aiello and G. Giordano (Taormina, 2002). The number of participants has been substantially increasing from close to 200 (Eger) to more than 300 (Taormina) and to over 400 (Prague), which clearly shows the growing interest in molecular sieve chemistry.

It is a pleasure for us to present this collection of 265 papers from authors of 45 countries in which the latest developments in the research and application of porous materials are described. Papers were selected from 406 submitted contributions and 69 of them were chosen for oral presentation (including 4 plenary lectures and 1 keynote lecture). In order to maintain a high scientific standard, all contributions were subjected to peer-review evaluation. The editors would like to acknowledge the support of the Paper Selection Committee and many referees who carefully evaluated first the submitted two-page abstracts and later on the final manuscripts.

Papers are organized in these Proceedings into five sections only: *(i)* synthesis, *(ii)* characterization, *(iii)* adsorption, *(iv)* catalysis, and *(v)* novel applications and miscellaneous. We have opted for only a few categories, not distinguishing between zeolites and other porous materials and intentionally avoiding sections as, *e.g.*, modeling. Theoretical contributions are placed next to the experimental ones in particular section in order to show the increasing importance of the overlap between experimental and theoretical work. Each of these five sections is organized as follows: the plenary and keynote lectures first, followed by oral and poster contributions. We hope that this book will serve as a broad overview of the state-of-the-art for research on porous materials.

Jiří Čejka Naděžda Žilková Petr Nachtigall

This Page is Intentionally Left Blank

SUPPORT AND SPONSORING

(as of May 5, 2005)

The Organizers of the 3rd FEZA Conference on Zeolites wish to thank various Institutions and Companies for their support to this Conference. Their contributions allowed a reduced registration fee for students and a bursary program.

INSTITUTIONS

Czech Zeolite Group

J. Heyrovský Institute of Physical Chemistry,
Academy of Sciences of the Czech Republic, Prague

and

Ministry of Education, Sport, and Youth of the Czech Republic

COMPANIES

BASF
Bruker AXS
Česká rafinérská, a.s., Czech Republic
Elsevier
EniTecnologie
Eurosupport
ExxonMobil Chemical
Haldor Topsøe A/S
IFP
INEOS Silicas
Micromeritics
Quantachrome
Research Institute of Inorganic Chemistry, Czech Republic
Shell Chemicals
Sigma-Aldrich, Czech Republic
Total
Tricat Zeolites
UOP
Zeolyst

This Page is Intentionally Left Blank

ORGANIZING COMMITTEE

Chairman

J. Čejka	J. Heyrovský Institute of Physical Chemistry, Prague

Vice-chairman

P. Nachtigall	Institute of Organic Chemistry and Biochemistry, Prague

Secretary

N. Žilková	J. Heyrovský Institute of Physical Chemistry, Prague

Treasurer

J. Ondráčková	J. Heyrovský Institute of Physical Chemistry, Prague

Members

G. Košová	J. Heyrovský Institute of Physical Chemistry, Prague
I. Nekoksová	J. Heyrovský Institute of Physical Chemistry, Prague
J. Klisáková	J. Heyrovský Institute of Physical Chemistry, Prague
Z. Pavlačková	J. Heyrovský Institute of Physical Chemistry, Prague
J. Pawlesa	J. Heyrovský Institute of Physical Chemistry, Prague
P. Topka	J. Heyrovský Institute of Physical Chemistry, Prague
D. Nachtigallová	Institute of Organic Chemistry and Biochemistry, Prague
J. Kučera	Institute of Organic Chemistry and Biochemistry, Prague
J. Nedvědická	Orgit, Ltd.
Z. Mlýnská	Orgit, Ltd.
R. Halfar	Orgit, Ltd.
L. Blaž	Orgit, Ltd.

INTERNATIONAL SCIENTIFIC BOARD (Council of FEZA)

M. Derewinski (President)	Poland
A. Gedeon (Secretary)	France
P.A. Kooyman (Treasurer)	The Netherlands
P. Behrens	Germany
P. Carrot	Portugal
J. Čejka	Czech Republic
P. Ciambeli	Italy
K. Franklin	United Kingdom
P. Hudec	Slovak Republic
I. Kiricsi	Hungary
C. Minchev	Bulgaria
J. Perez-Pariente	Spain
R. Russu	Romania
G. Tsitsishvili	Georgia

PAPER SELECTION COMMITTEE

A. Alberti	(Ferrara, Italy)
J. Čejka	(Prague, Czech Republic)
C.S. Cundy	(Manchester, United Kingdom)
F. Fajula	(Montpellier, France)
P. Nachtigall	(Prague, Czech Republic)
F. Schüth	(Mülheim, Germany)

TABLE OF CONTENTS

SYNTHESIS OF MICROPOROUS AND MESOPOROUS MATERIALS

CHARACTERIZATION OF POROUS SOLIDS

CATALYSIS

SYNTHESIS OF MICROPOROUS AND MESOPOROUS MATERIALS

This Page is Intentionally Left Blank

Studies in Surface Science and Catalysis, volume 158
J. Čejka, N. Žilková and P. Nachtigall (Editors)

Strategies in developing routes to commercialization of novel high silica zeolites

S.I. Zones [a], H. Lee [b], M.E. Davis [b], J. Casci [c], A.W. Burton [a]

[a] ChevronTexaco Energy and Technology Company, Richmond, CA, USA 94802

[b] Department of Chemical Engineering, California Institute of Technology, Pasadena, CA USA 92115

[c] Johnson Matthey Catalysts, PO Box 1, Billingham, Cleveland TS23 1LB, UK

In this paper we will contrast the exciting initial work of finding new molecular sieves and the follow-up items needed to address moving forward with application development of a material. Principally, to arrive in the marketplace, the economics must be attractive for introducing new technology. A key hurdle in the production of high silica zeolites, metallophosphates, metalloorganic frameworks, and many novel silicogermantes, is the management of the costs concerning the guest organo-cations and amines used as structure directing agents (SDA's). In this discussion we will describe several novel routes attempting to create a positive impact on this issue.

1. INTRODUCTION

There has been a continuous trend in breakthroughs in creating new molecular sieve materials. It is an exciting frontier area for material science and nanotechnology as specific applications are envisioned. A recent report on the field shows the increase in discovered materials and the corresponding patent activity [1]. Even the increased diversity in the number of materials commercialized supports the quest for more new structures and compositions. The contrast of the number of three-dimensional frameworks recognized by the International Zeolite Association (IZA) and the subsequent commercial use runs about a 15 or 20-1 ratio. Only a small percent has had a chance to see commercial use.

Equally vital to the eventual commercial use will be the synthetic challenges of controlling crystallite size, possibly morphology, surface features and elemental composition. Another changing variable in determining the opportunity to commercialize a new molecular sieve can be the value of the end use. Here we can imagine something of a cost continuum along the lines of:

Adsorbents, FCC catalysts	←----------→	Pharmaceutical Catalysts
(1-8 Euro/Kg)		(50-100 Euro/Kg)

In this brief contribution we will highlight a few chemistries that have been particularly useful of late in finding novel structures. These will primarily be excursions into the use of novel guest molecules (SDA's) coupled with novel inorganic chemistry, focused on the use of

silicate systems with B, F and Ge as possible co-factors. The phosphate based molecular sieve syntheses had previously shown a great diversity in structures and compositions but in those systems, it was less clear that the SDA introduced as much of an influence on space-filling [2]. Even more recently metal-organic molecular sieves, developed around di and tri carboxylate ligands and metal centers (termed MOF) have produced an impressive array of structure types [3-5].

Moving on from initial structure discoveries, we will show several strategies designed to lower the cost of the synthesis. As we discuss these approaches we will occasionally interweave the effect some of these changes would have on the cost of producing zeolite SSZ-33 (**CON** in the structure code terminology used by the IZA). This zeolite is an intergrowth of two pure polymorphs and possesses both 10 and 12-ring pores. It is made as a borosilicate sieve [6]. The end member structures are CIT-1 [7] and ITQ-24 [8]. The structural details are in Fig. 1. An aluminosilcate version is also known via direct synthesis and is zeolite SSZ-26 [9]. However, this synthesis procedure requires several steps to produce the requisite dicationic propellane SDA that specifies this product. This material is of interest in our discourse of the more general problem of efficient synthesis developments because it has recently been shown to have desirable properties relative to commercially available beta zeolite as a hydrocarbon trap in automotive emission control technology. The recent work came from the labs of Davis at Caltech and Okubo at the University of Tokyo [10].

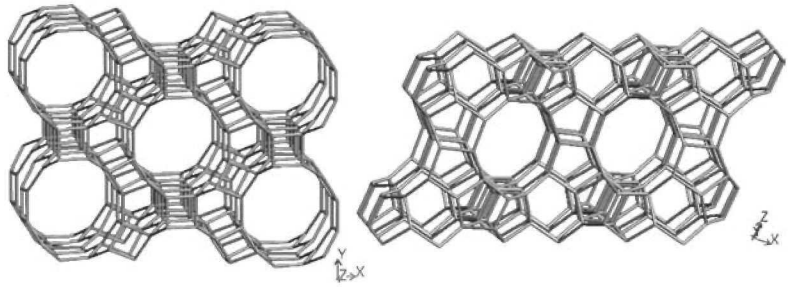

Fig. 1. The structure of CON

2. SOME ROUTES TO THE NEW CHEMISTRIES

We have been encouraged by the rich diversity of novel zeolite structures obtained through the use of boron as a substituting trivalent element inserted into the framework during synthesis of silicate guest using SDA hosts. Table 1 shows a representation of mostly large pore zeolites we have discovered using the borosilicate chemistry. More than half can also be made by direct synthesis with aluminum instead of boron, but there remains some that can only be made from borosilicate systems. In the list of materials, the 12/10 SSZ-33 appears as well as novel 14-ring zeolites SSZ-53 and 59, and the new intersecting 10-ring zeolite SSZ-58. Multidimensional 10-ring zeolites have proven to be very rare finds in this chemistry despite the early discoveries of ZSM-5 and 11 more than 30 years ago. References for these materials are given in Table 1. In our recent study of the synthesis of a selected system, SSZ-42 (**IFR**) showed the possibility that boron may be added from solution to the growing zeolite

Table 1
Synthesis of Large Pore Zeolites

Zeolite	*Aluminosilicate*	*Borosilicate*	*All SiO_2*	*D*	*IZA Code*	*Reference*
SSZ-24	—	+	+	1	**AFI**	11
SSZ-26	+	—	—	12/10	**CON**	11
SSZ-31	—	+	+	1	—	12
SSZ-33	—	+	—	12/10	**CON**	11
SSZ-37	+	+	—	10/12	—	13
SSZ-41	+	—	+	1	—	14
SSZ-42	+	+	+	1	**IFR**	11
SSZ-47	+	+	—	1	—	15
SSZ-48	—	+	—	1	**SFE**	11
SSZ-53	—	+	—	1	**SFH**	11
SSZ-55	+	+	+	1	**ATS**	11
SSZ-57	+	+	+	?	—	16
SSZ-58	+	+	—	10/10	**SFG**	11
SSZ-59	+	+	—	1, 14	**SFN**	11
SSZ-60	—	+	—	1, 12	**SSY**	11
CIT-5	+	—	+	1, 14	**CFI**	11
UTD-1	—	+	+	1, 14	**DON**	11

crystal and that the amorphous silicate gel material, when separated early in the reaction does not contain boron. This is a great contrast to aluminosilicate systems and we showed this for the synthesis kinetics of beta zeolite using the same SDA as for borosilicate SSZ-42 [17]. This may provide a key as to why some novel SDA produce new structures in the presence of borosilicate inorganic systems, but not when the chemistry is aluminosilicate.

For many catalytic and separations applications it is desirable to have Bronsted acid sites which are strong, as in the case of Al, and contrasted with the known weak acidity of boron sites. Fortunately, when the zeolite pores are large (> 6 A), it is possible to replace the boron with aluminum, within the lattice, once the guest SDA has been removed. Surprisingly, we have been able to carry out this substitution/re-insertion chemistry under acidic conditions

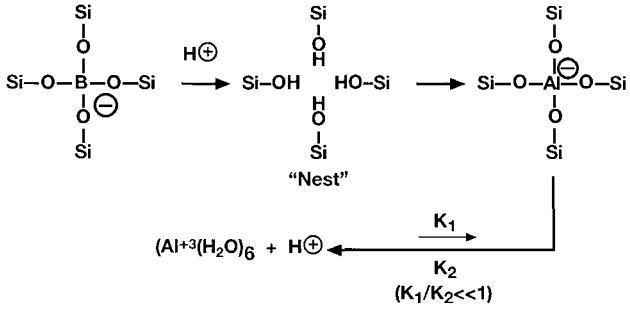

Fig.2. An advantage in synthesizing new large pore zeolites as borosilicates

with the Al+ cations kept soluble. Fig. 2 shows a schematic of such a reaction. This approach has been used to convert SSZ-33 into a material with strong acidic centers for use in such applications as the hydrocarbon trap [18].

The laboratory at the Instituto de Tecnología Química at the Universidad Polytécnica in Valencia, Spain, has pioneered the breakthrough of two great chemistry innovations in molecular sieve synthesis. The first, going back nearly a decade and building on the pioneering work of the groups of Flanigen [19] and Guth and Kessler [20], and others, Professor Corma's group (in Valencia) explored the use of fluoride anions in synthesis. But the great breakthrough came in looking at reaction systems with much lower-than-usual amounts of water. The reactions were very concentrated. This approach led to the discovery of a number of all-silica materials with low framework density and high microporosity. This had rarely been seen in silicate synthesis chemistry. The fluoride provides an important structure-determining factor under these concentrated conditions and it is found in the product [21, 22]. A number of these new phases and or compositions are listed in Table 2.

Table 2
Some novel structures from use of HF in molecular sieve synthesis

Structure	*Details*	*Reference*
ITQ-1	All SiO_2 **MWW**	23
ITQ-2	Exfoliated **MWW**	24
ITQ-7	Multidimensional large pore	25
ITQ-12	Multidimensional small pore	26
ITQ-13	Multidimensional 9, 10 rings!	27
ITQ-29	All SiO_2 **LTA**	28

We followed this lead of Professor Corma's group and using a large array of SDA we had developed we explored this reaction. Table 3 shows some of the novel silicate compositions we obtained in this chemistry. A greater discussion of these findings is contained in ref 29. Mainly we were finding that we could make some very open framework materials as all-silica for the first time. This has some impact on the use of silicates in membranes and in electronic materials [30].

Table 3
New all-silica phases

Phase	*Structure Code*	*Dimensionality*
SSZ-33	**CON**	Multi; 12x10 Rings
SSZ-50	**RTH**	Multi; 8x8 Rings
SSZ-55	**ATS**	1D, 12
EU-1	**EUO**	Multi; 10 Rings with Pockets
SSZ-37	**NES**	Multi; 10 Rings with 12-ring pockets
SSZ-61	+	At Least one Large Pore (TEM)

The second breakthrough came from using Germanium as a silica substituent, in the presence of Fluoride, and then later without it. With this approach, and trying a variety of SDA the

Corma group discovered a number of novel frameworks were produced. A key feature is the influence of Germanium to form double 4-rings within the structures [31]. This feature is almost never seen for silica alone. Some of the materials employed by this route are shown in Table 4. Amongst the highlights is the discovery of a **FAU** material with 6 portals into the cage instead of 4 (ITQ-22), and the first ever report of **LTA** as all-silica (ITQ-29).

Table 4
Some novel structures from use of Ge in molecular sieve synthesis

Structure	*Details*	*Reference*
ITQ-15	14 and 12 rings	32
IM-12	14 and 12 rings	33
ITQ-17	Multidimensional large pore	34
ITQ-21	Multidimensional large pore	35
ITQ-22	Multidimensional large pore	36

3. ATTEMPTS TO MAKE ZEOLITE REACTION REQUIRING SDA MORE ATTRACTIVE FOR SCALE-UP

3.1. The combination of less SDA and use of a pore-filler amine

One of the recognizable features of high silica zeolite syntheses is that most reactions require an excess of SDA over what is found in the void regions of the guest/host product. The pores are filled with guest molecule as the zeolite forms and this is necessary to stabilize the structure against re-dissolution and progression towards more condensed products like quartz (Ostwald Ripening reaction) [37]. A typical reaction is run with SDA/SiO_2 of 0.10 or higher and the product ratio will be closer to 0.04-0.02. Is the extra SDA needed to influence

SDA	SDA/SiO_2	Zeolite
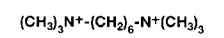	0.04	EU-1
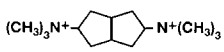	0.04	EU-1
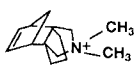	0.02	SSZ-35
	0.02	ZSM-11
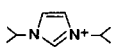	0.02	SSZ-32
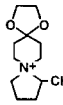	0.03	ZSM-12
	0.05	SSZ-28

Fig. 3. Zeolites made from mixed amine/SDA route

nucleation or support the formation of reaction equilibria such that SiO_2 units are not moved into a different kinetic product? One idea we had was to work at an SDA level near or even below the amount needed to fill the pores and then to supplement both our basicity (losing OH from SDA reduction) and pore-filling by adding a non-selective amine into the synthesis [38]. We had previously learned that for a number of high silica syntheses using SDA, the alkali content needed to be low enough that layered silicates didn't predominate [39]. The amines alone without the presence of small amounts of our specific SDA will often help to produce **MFI** in the presence of alkali cations [40]. In the presence of amines like isobutyl and cyclopentyl, a number of zeolites can be made as shown in Fig. 3. Even though our goal was to use the SDA in ratios of 1/10 to amine (and thus as low as 1/50 to SiO_2), NMR experiments showed that the SDA is found in the product. One can also imagine a synthesis system where the amine can be recycled through distillation.

Another side of this approach is that there may be important opportunities in the amine choice of this 2 component organic approach. One of the zeolites found in this approach and shown in Fig. 4 is SSZ-47. We noticed that the diffraction patterns for SSZ-47 bore some similarity to the family of materials **NES/EUO/NON** which are related through variations in sub-unit connection. A puzzle for us was why SSZ-47 often had lower micropore volumes than we expected for a large pore zeolite (catalysis data). We wondered if an intergrowth was closing off channels. This could come from Nonasil cages being developed (**NON**, a clathrate structure). By choosing an amine that was too large to fit in the cages and using it with a small amount of SDA, we greatly increased the micropore volume of the zeolite. The x-ray diffraction pattern also changed, indicating the loss of a peak attributable to **NON**. All these features are compared in Fig. 4. This solution yields (a) a more active interesting zeolite and (2) a cheaper route to making SSZ-47 (as B) over its invention circumstances.

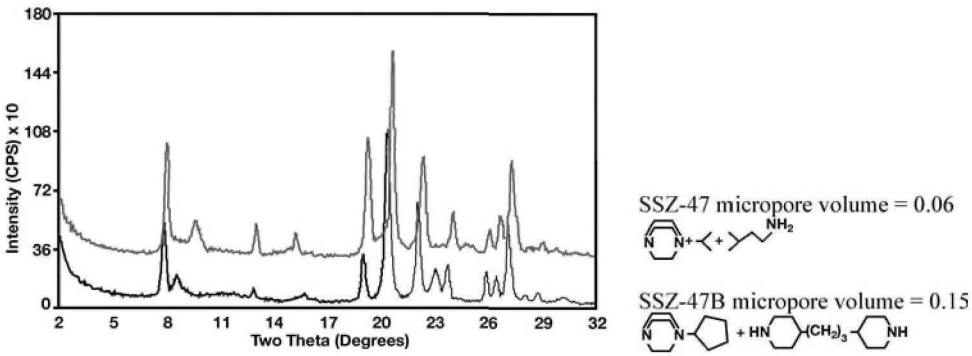

Fig. 4. X-ray diffraction patterns for SSZ-47 (top) and 47B (bottom)

3.2. Use of a recyclable SDA

A newer approach has been to consider if an SDA can be constructed so that it functions during zeolite synthesis (under basic pH conditions) and then can be broken into smaller fragments after the synthesis, removed from the pores and then re-combined for use again. This eliminates any waste material in the synthesis and this will be highlighted in the next section. The key work was carried out in the lab of Professor Mark Davis at Caltech with SDA built around combining a charged piperidine component and a ketal segment. Fig. 5 shows how the cycle would work [41].

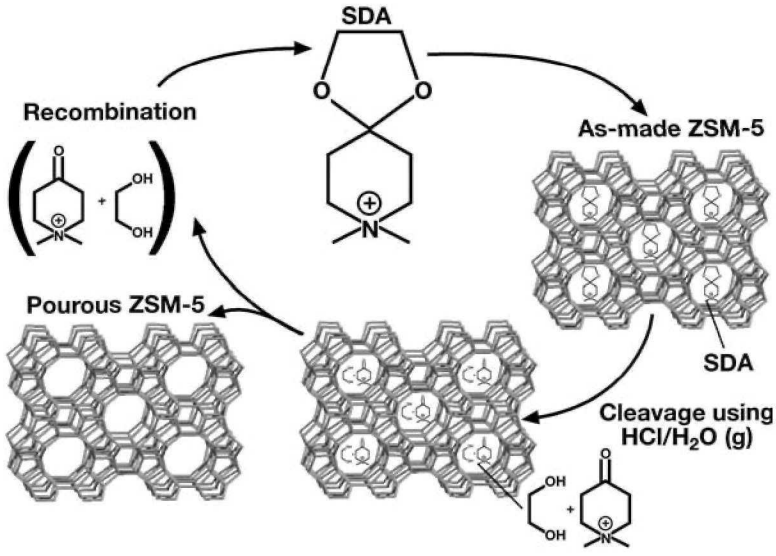

Fig.5. Proof of concept

An ancillary benefit for this approach will be that if the SDA can be removed by a solution (acidic) treatment, then a calcination step is avoided. This can have important consequences for the state of Al+3 sites in the zeolite as high temperature treatments can pop some of it out of the framework [42]. A solution treatment could avoid this.

In some more recent work Lee has made some interesting perturbations in the recyclable system. The SDA is combined with small, pore –filling amines. While this lowers the cost of the SDA, it also makes it easier to gain access to the pore system for the fragmentation step in the loop in Fig. 5 [43]. Lee has gone on to prepare a number of ketal derivatives (Fig. 6) and finds that multi-dimensional zeolite products have an easier time in fragmentation of the SDA as contrasted with some one-dimensional zeolites like VPI-8 (**VET**) which are of considerable interest [44].

4. SOME KEY ISSUES IN THE TRANSLATION TO MANUFACTURE

We use the term translation here because this is exactly what is needed. One takes the results from discovery, synthesis, testing and characterization successes and then asks whether it can be operable in a world of different parameters. Let's look at these translations by dividing our problem into several linear segments.

4.1. The SDA issues

As long as we need the SDA in our process there are some hurdles to clear. We need to know who can manufacture it. This is increasingly challenging in that more major chemical companies outsource so much that maintaining a steady supply of a material with constant specifications is very difficult. In our SSZ-33 example we've been using, the initial supplier of a key component for the SDA no longer exists. We obviously have cost-control issues. The hope is to use the least amount of SDA possible, but the economics of scale make it cheaper per unit at a larger order. Here an excellent strategy is to develop a zeolite for more than one application.

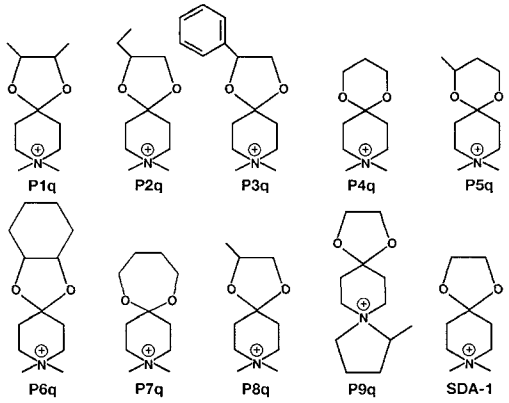

Fig. 6. Ketal SDAs

If one develops an SDA not previously commercialized, there will be permit and testing issues to be handled. These require both time and money. Even if we pass those checkpoints there is the need to verify plant compatibility including issues of worker exposure and corrosivity towards equipment.

4.2. Mixing and stirring

Changes in the competition for viable nuclei can result in response to moving to larger reaction scale. Tip speed changes in the process. Also the heat-up and cool down rates must be slower and the mode of heating changes entirely in using jacketed systems. Our reactor design must safeguard that pockets of inhomogeneity do not occur. These can be "breeding" sites for impurity phases forming in regions disproportionately rich in Al or Si. Also one wants to optimize the output per batch reactor. This becomes an issue of working in the most concentrated conditions possible. In turn the system is more viscous and transport issues of moving nutrients from the gel to solution become more challenging.

4.3. Batch time

Unlike the work one does in the invention steps, or preparing materials for testing in catalysis and other applications, the time in the batch reactor to crystallize the zeolite now becomes an important variable. Strategies that can shorten the induction time needed to get stable nuclei that proceed to crystal formation are needed. Also, because of the large mass, increases in the cool down rates can take longer in the use of the batch reactor. If one is attempting to develop a new zeolite that is intended to displace a commercial zeolite, each extra day in the crystallizing reactor can add as much as 10 euro/kg to the zeolite cost.

4.4. Filtration technology

In our inventive steps, collecting a product can be a matter of filtering the material and washing with plenty of water. If the crystals are quite small then it might be useful to switch to a centrifugation approach. Here the product is spun down and the solution decanted. Fresh water is added, the solids are dispersed and the centrifugation can be repeated until a low conductivity value is measured for the wash solution. At the larger scale, strategies must be devised to be able to use filtration to collect the product as a filter cake. Amongst the strategies that can be employed is the use of filter aids. These materials are surfactants or

organic polymers, which are either polar or charged and they serve to help aggregate crystals by interaction with the zeolite surface. After collection of the zeolite product, these components can be removed in the subsequent calcination steps that will follow.

4.5. Waste removal

The economics of making a zeolite product are now impacted at the commercial level by how one treats the supernatant from the batch reactions. In essence one now has a waste stream to manage. Here is where the extra SDA in the synthesis now generates an additional cost. Strategies which have been discussed in this paper, such as using a minor amount of SDA coupled with a larger amount of non-selective amine, could prove beneficial if (a) all the SDA is found in the pores of the product and (b) the amine can be distilled (or flashed) and used again. Likewise the impetus for the recyclable SDA approach (Davis lab) is the desire to be able to not only lower cost by re-use of the SDA, but also via the reduction in waste processing costs. Waste streams can be treated by a variety of approaches before the water can be released to the general sewage system. A recyclable approach could eliminate much of this.

The reader wishing to see more detail on some of these issues is referred to an excellent recent publication from Casci [45].

One other approach to cost saving in manufacture is worth noting here. Recently, an approach has been developed by Miller and co-workers to run a preparation of a zeolite gel at surprisingly concentrated conditions (H_20/SiO_2 = 3-6) and then form the seemingly dry solid mix into a pellet through extrusion[46]. Next the pellets are heated until they become crystalline zeolites, already retaining catalyst particle morphology. This eliminates some of the catalyst formation steps and of course greatly reduces the volumes of water employed in the synthesis. The batch "throughput" can jump significantly.

5. SUMMARY

In this short review we have attempted to point out some of the new areas where silicate based molecular structures are emerging. After doing so we concentrated on a range of approaches to lower the cost of bringing a material to the marketplace by making cost-impact changes concerning the most expensive component of the system, the SDA. Finally we touched upon the changes in concerns as the scales become large for the synthesis. We acknowledge the highly important contributions to this last step made by the chemists and engineers who solve these problems behind closed doors in industry.

REFERENCES

[1] S. Auerbach, K. Carrado, P. Dutta, Handbook of Zeolite Technology (Marcel Dekker) 2003.
[2] E.M. Flanigen, B.M. Lok, R.L. Patton, S.T. Wilson, Proc. 7th Int. Zeol. Conf., Tokyo (1986) 103.
[3] O. Yaghi, Science, 295 (2002) 469.
[4] M. Sanselme, G.M. Greneche, M. Riou-Cavellec, G. Ferey, Solid State Sciences, 6 (2004) 853.
[5] A.K. Cheetham, G. Ferey , T. Loiseau, Angew. Chemie Intl. Ed., 38 (1999) 3268.
[6] R.F. Lobo, M. Pan, I.Y. Chan, H-X. Li, R.C. Medrud, S.I. Zones, P.A. Crozier, M.E. Davis, Science (1993) 1543.
[7] R.F. Lobo, M. E. Davis, J. Am. Chem. Soc., 117 (1995) 3764.
[8] A. Corma, J. Am. Chem. Soc., 125 (2003) 7820.
[9] S.I. Zones, M.M. Olmstead, D.S. Santilli, J. Am. Chem. Soc. 114 (1992) 4195.

[10] S.P. Elangovan, M. Ogura, M.E. Davis, T. Okubo, J. Phys. Chem. B 108 (2004) 13059.
[11] http://www.iza-structure.org/databases/
[12] R.F. Lobo, M. Tsapatsis, C.C. Freyhardt, I. Chan, C.Y. Chen, S.I. Zones, M. Davis, J. Am. Chem. Soc., 119 (1997) 3732.
[13] M.M. Helmkamp, M.E. Davis, Ann. Rev. Mater. Sci., 25 (1995) 161.
[14] S.I. Zones, D.S. Santilli, US Patent 5,656,149 (1997).
[15] G.S. Lee, Y. Nakagawa, S.I. Zones, U.S. Patent 20020027935 (2001).
[16] S. Elomari, US Patent 20020081262 (2002).
[17] S.I. Zones, S-J. Hwang, Microporous Mesoporous Mater., 58 (2003) 263.
[18] C.Y Chen, S.I. Zones, Proc. Intl. Zeolite Assoc., Montpellier , France (Elsevier, Amsterdam) paper 11_P-16 on CD-ROM (2001).
[19] E.M. Flanigen, R.L. Patton, US Patent 4, 073, 865 (1978).
[20] J-L.Guth, H. Kessler, R. Wey, Stud. Surf. Sci. Catal., 28 (1996) 121.
[21] A. Corma. M.J. Diaz-Cabanas, J. Martinez-Triguero, F. Rey, J. Rius, Nature, 418 (2002) 514.
[22] G. Sastre, J. A.Vidal-Moya, T. Blasco, J. Rius, J.L. Lorda, M.T. Navarro, F. Rey, A. Corma, Angew. Chem. Intl. Ed., 41 (2002) 4722.
[23] M.A. Camblor, A. Corma, M.J. Diaz-Cabanas, J. Phys. Chem. B, 102 (1998) 44.
[24] A. Corma, V. Fornes, S.B. Pergher, T.L.M. Maesen, J.G. Buglass, Nature, 396 (1998) 353.
[25] http://www.iza-structure.org/databases/, + "Atlas of Zeolite Framework Types", + "ISV".
[26] P.A. Barrett, T. Boix, M. Puche, D.H. Olson, E. Jordan, H. Koller, M.A. Camblor, Chem. Comm. (2003) 2114.
[27] A. Corma, M. Puche, F. Rey, G. Sankar, SJ. Teat, Angew. Chem. Int. Ed., 42 (2003) 2702.
[28] A. Corma, F. Rey, J. Ruis, M.J. Sabater, S. Valencia, Nature, 431 (2004) 287.
[29] S.I. Zones, S-J. Hwang, S. Elomari, I. Ogino, M.E. Davis, A.W. Burton, Compt. Rend. –Chem. (2005) in press.
[30] A. Mitra, Z. Wang, T. Cao, H. Wang, L. Huang, Y. Yan, J. Electrochem. Soc., 149 (2002) B472.
[31] A. Corma, Proc. 14th International Zeolite Conf., Cape Town. South Africa, Plenary Lecture (2004).
[32] A. Corma, M.J. Diaz-Cabanas, F. Rey, S. Nicolopoulus, K. Boulahya, Chem. Comm. (2004) 1356.
[33] J.-L. Paillaud, B. Harbuzaru, J. Patarin, N. Bats, Science, 304, (2004) 990.
[34] A. Corma, M.T. Navarro, F. Rey, J. Rius, S. Valencia, Angew. Chem. Int. Ed., 40 (2001) 2277.
[35] A. Corma, M.J. Diaz-Cabanas, J. Marinez-Triguero, F. Rey, J. Rius, Nature, 418 (2002) 514.
[36] A. Corma, F. Rey, S. Valencia, J.L. Jorda, J. Rius, Nat. Mater., 2 (2003) 493.
[37] S.I. Zones, S-J. Hwang, M.E. Davis, Chem. Eur. J., 7 (2001) 1990.
[38] S.I. Zones, S-J. Hwang, Chem. of Mater., 14 (1) (2002) 313.
[39] S.I. Zones, Microporous Mater., 2 (1994) 281.
[40] R.M. Barrer, Hydrothermal Chemistry of Zeolites, Academic Press, (1982).
[41] H. Lee, M.E. Davis, S. I. Zones, Nature, 425 (2003) 385.
[42] H-K. Timken, G. Kuehl, Microporous Mesoporous Mater., 35-36 (2000) 521.
[43] H. Lee, M.E. Davis, S. I. Zones, J. Phys. Chem. B, 109 (2005) 2187.
[44] H. Lee, Ph.D Thesis, California Institute of Technology, 2005.
[45] J. Casci, Proceedings from the 2004 Summer School on Zeolites, "Zeolite Molecular Sieves: Preparation and Scale-up", Microporous and Mesoporous Materials, (2005) in press.
[46] http://www.chevron.com/prodserv/refiningtechnology/zeolite_plus_8a.shtm

Studies in Surface Science and Catalysis, volume 158
J. Čejka, N. Žilková and P. Nachtigall (Editors)

Colloidal LTL zeolite synthesized under microwave irradiation

M. Hölzl, S. Mintova*, T. Bein

Department of Chemistry and Biochemistry, Ludwig-Maximillians-University of Munich, Butenandtstr. 5-13 (E), 81377, Munich, Germany

The fast synthesis of zeolite L (LTL type structure) from a clear precursor solution (K_2O-Al_2O_3-SiO_2-H_2O) under microwave (MW) irradiation is described. The crystallization time of LTL zeolite under MW was decreased substantially in comparison to conventional hydrothermal heating, i.e., to 30 and 10 minutes at synthesis temperatures of 170° and 190 °C, respectively. The degree of crystallinity is as good as from conventional heating method and the size of particles is smaller. However the particle size distribution is increased with escalating the synthesis temperature. The crystallization process has been followed with various methods including XRD, DLS, TEM, nitrogen sorption, etc.

1. INTRODUCTION

A variety of crystalline framework type materials with pore diameters in the range of 0.3-1.2 nm have been prepared over the last few years by conventional hydrothermal treatment. In addition, periodic mesoporous materials have been synthesized via self-assembly of long-chain surfactant molecules and inorganic matrix components under quasi-ambient conditions. However, there are only few ordered micro- and mesoporous materials prepared from colloidal precursor solutions resulting in the formation of nanosized crystals with hydrodynamic diameters of 10-100 nm [1-9].

The recent trend to develop rational synthetic strategies for preparation of nanosized porous crystals with variable chemical compositions including pure silicates, aluminosilicates and aluminophosphates is illustrated by the extensive work on the synthesis from supersaturated precursor solutions containing always organic additives under specific synthesis conditions, i.e., long crystallization time at room temperature (RT) or short crystallization at elevated temperature under microwave radiation. The 'microwave-effect' is recognized with the uniform and increased heating rate of the reaction mixture and enhanced dissolution of the initial compounds leading to spontaneous nucleation and formation of nanosized crystals with equal particle sizes. Via applying microwave heating the possibility to synthesize zeolites for short crystallization times compared to classical synthesis route has been demonstrated. Several theories describing the effect of microwave heating on the zeolite crystallization process are discussed and being reviewed in the literature [10], however the so called 'microwave-effect' is mostly attributed to the uniformed heating and increased heating rate of the reaction mixture during the first several minutes. In addition, the superheating and hot spots in the reaction mixtures may explain the faster crystallization of the zeolites. Nevertheless, only some of the microporous materials have been synthesized under microwave radiation.

It is well known that the synthesis route for preparation of zeolites and related materials is govern by the formation of small amorphous entities in the precursor solutions or gels. The type of the initial precursor solution and the conditions for hydrothermal treatment are responsible for a high nucleation and crystallization rates, resulting in the formation of stable nanosized particles with zeolite crystalline structures. By applying microwave heating the microporous materials with structures such as EDI, LTA, MFI, FAU, BEA, AFI and AEI have been prepared within several minutes [11-15].

The interest in the synthesis of LTL type zeolite is based on its wide applications in conventional catalytic processes such as aromatization of *n*-hexane, chlorination of aromatic organic molecules, etc. [16,17]. On the other hand, zeolite L is also used as hosts for the incorporation of dyes and especially for light harvesting systems [18]. For most of these applications the size and shape of the zeolite crystals as well as the high crystalline yield are very important [19].

In this work we report the rapid synthesis of nanosized LTL zeolite using microwave heating that leads to the formation of fully crystalline particles in the nanometer range. Additional investigations concerning the crystallization process were performed, where the temperature and time were varied leading to formation of nanoparticles with mono- versus poly- modal particle size distribution.

2. EXPERIMENTAL

The initial precursor solutions used for further microwave treatment have the following chemical composition: 5 K_2O : 10 SiO_2 : 0.5 Al_2O_3 : 200 H_2O. The solutions have been prepared via dissolving 40.0 mmol aluminum hydroxide (3.9 g $Al(OH)_3$, type A2100, 80 wt. % Al_2O_3, 20 wt. % H_2O) and 0.4 mol potassium hydroxide (23.3 g KOH, Aldrich) in 86.0 g double distilled (dd) water, and to this solution 0.4 mol colloidal silica (83.1 g SiO_2 Ludox SM30, Aldrich) was added. The resulting mixtures were stored for one day on an orbital shaker and additionally were stirred for one more day to obtain water-clear precursor solutions.

All syntheses are performed in a QWave 3000 Questron microwave oven (1200 W); six Teflon lined autoclaves were filled with 25 ml initial precursor solutions. After the microwave heating all samples were purified using high-speed centrifugation (60 min, 20 000 rpm, 3 times) and then the particles were redispersed in distilled water using an ultrasonic bath. For simplicity, the samples abbreviated with L170-n′ (n= 20, 30 and 90) are corresponding to LTL samples exposed to MW irradiation at 170 °C for 20, 30 and 90 minutes, respectively. Samples L190-n′ (n= 5, 10 and 40) are corresponding to LTL zeolite synthesized at 190 °C for 5, 10 and 40 minutes.

Crystallinity and purity of the samples were determined with a STOE STADI-P X-ray diffractometer using Ge monochromated Cu K_α radiation. The change in the particle size of the zeolites during crystallization process was determined with dynamic light scattering (DLS) using a Malvern Zetasizer (Nano ZS) instrument in backscattering geometry; the surface charge of the particles and their stability were determined from the zeta-potential measurements. The transformation process of the amorphous into crystalline LTL particles was followed by HRTEM using a JEOL T2100 microscope. The chemical compositions of the final crystalline samples were determined based on inductively coupled plasma-atomic emission spectrometry (ICP-AES). In addition, the porosity of the samples is proved by the nitrogen sorption measurements performed with a Quantachrome Nova 4000e at liquid nitrogen temperature.

3. RESULTS AND DISCUSSION

The template- free alumininosilicate solutions were subjected to microwave heating at 170 °C and 190 °C in order to study the influence of both the type of heating and synthesis temperature on the main characteristic of LTL zeolites such as particle size, polydispersity, stability, and porosity. The crystallinity of the samples was confirmed by the XRD patterns collected from purified powders after heating for different times in the MW oven. As can be seen from Fig. 1a, the amorphous aluminosilicate matter has been converted into LTL zeolite within 30 min at 170 °C; no additional phase after longer time of microwave treatment was formed. The intensity, position and width of the all reflections for samples L170-30′ and L170-90′ are nearly the same. Even faster crystallization of LTL zeolite was observed at 190 °C (Fig. 1b). After five minutes of MW heating a broad Bragg reflection at 5.4° 2θ is appeared similar to the L170-20′ sample heated for 20 minutes. However, fully crystalline zeolite particles were obtained for 10 min at 190 °C. Further MW treatment for 40 min did not lead to any change in the intensity of the Bragg reflections in sample L190-40′ compared to sample L190-10′.

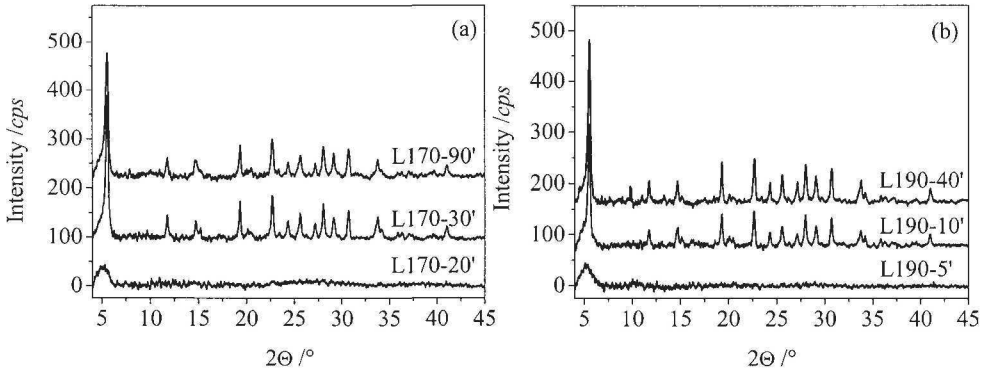

Fig. 1. XRD patterns of LTL samples synthesized at (a) 170 °C and (b) 190 °C.

The degree of crystallinity is an important factor for the zeolite nanoparticles in the final crystalline suspension. Moreover the particle size distribution in the colloidal suspensions during the entire crystallization process is a crucial point for the formation of zeolites with a different degree of polydispersity. DLS study has been performed for all samples subjected to MW treatment for various times and compared with the XRD data revealing the ratios between the amorphous and crystalline matters. The size of the X-ray amorphous particles in the initial solutions prior to crystallization varied from 40 nm to 180 nm. Approximately the same size of the particles is measured for the samples synthesized at 170 °C (see Fig. 2). As can be seen the sample L170-20′, which is mainly X-ray amorphous contains particles with a mean size of about 140 nm, and this value did not change significantly for the fully crystalline sample L170-30′. The final particle size of LTL zeolite is about 90 nm in diameter (Fig. 2a). Similar observations where made for the LTL prepared at 190 °C (Fig. 2b). Both sample L190-5′ that is X-ray amorphous and the fully crystalline sample L190-10′ have nearly the same mean particle size of ~210 nm. It is decreased negligibly up to 170 nm under prolonged heating i.e. 40 min (see sample L190-40′). This

indicates that the slow dissolution of the particles takes places during the prolonged MW treatment.

The DLS results reveal that LTL zeolite synthesized at 170 °C have smaller crystals with low degree of polydispersity in comparison to samples prepared at 190 °C. Similar observation has been made for LTL synthesized in conventional oven where the crystallization process took almost 4 days [9].

The surface charge of the individual amorphous particles formed in the solution is important for their stability during the entire synthesis process. DLS is used to resolve the electrophoretic mobility of the particles in the solutions. By applying the Huckel equation the zeta potential has been determined, and the magnitude of the zeta potential value corresponds to the stability of the colloidal particles in the suspensions. If the zeta potential is high (> ± 30 mV), the particles do not tend to agglomerate since the repulsive forces in-between the individual crystals are dominant. The zeta potential measurements were performed for all solutions with pH=7 after washing and redispersion in dd H_2O, while for the initial precursor solution the zeta potential was measured before (pH=14) and after washing (Fig. 3).

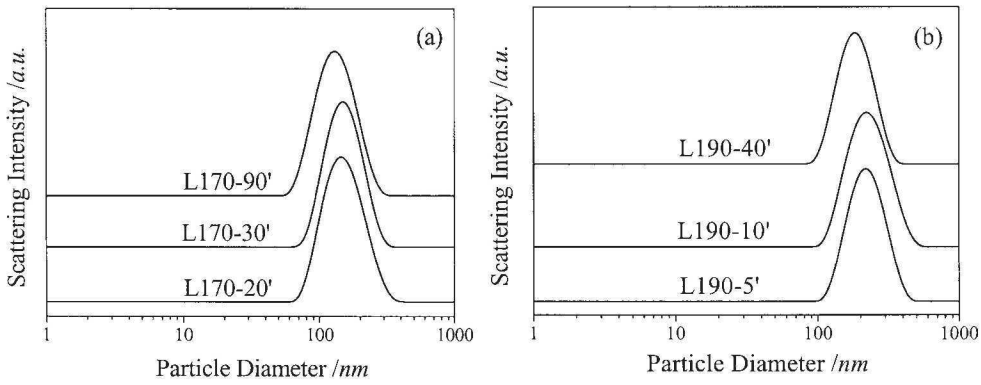

Fig. 2. DLS data of LTL samples synthesized at (a) 170 °C and (b) 190 °C.

The zeta potential value of the as prepared solution is varied from – 190 mV to + 170 mV, which is due to the presence of various amorphous aluminosilicate particles and excess of potassium hydroxide (Fig. 3a). The maximum of the zeta potential curve is at about zero, while in the purified solution the value is - 50 mV (Fig. 3b), which is reflecting the negative surface charge of the particles present in the initial precursor solution at pH=7. The negative surface charge of the amorphous particles stabilized in H_2O is conterminous with repulsive forces between the individual particles that explain their stability. An agglomeration of the particles was not observed for a period for at least three months. The zeta potential values of the fully crystalline samples L170-30′ and L190-10′ obtained after complete consumption of the amorphous particles were measured; the values for the crystalline LTL nanoparticles are always in the negative range, i.e., - 50 ÷ – 30 mV. However the LTL nanocrystals prepared at 170 °C have more negative zeta potential value and this probably explains the small particle size of the crystals synthesized at this temperature and lower degree of agglomeration. The zeta potential values of the completely crystalline LTL particles are similar to the one measured for particles in purified initial precursor solution demonstrating high stability and

high electrostatic forces of repulsion between the individual nanoparticles. However the particles synthesized at 170 °C have most negative zeta potential value in comparison with those synthesized at 190 °C. This might me due to the chemical composition of the different samples. Although the Si/Al ratio in the precursor solution was 10, then for the extracted amorphous particles from the solutions prior to MW heating was measured to be 3, while the K/Al ratio was shifted from 10 to 1.56 from non-purified to purified amorphous particles.
The low potassium amount in the initially formed amorphous particles demonstrates that the excess of potassium is removed after purification, and the high amount of KOH is needed only to adjust the pH of the solution and fully dissolve the initial reagents. However, it is interesting to note that the chemical composition of purified amorphous particles is comparable with that for the fully crystalline LTL zeolite. This result suggests that the amorphous agglomerates have not only the same particle size but also the same chemical composition as the crystalline LTL zeolite nanoparticles. The ratios Si/Al and K/Al were measured for the particles extracted from amorphous precursor solutions, for all intermediates having different degree of crystallinity and for the completely crystalline samples. It has been found that the Si/Al ratio is decreased from 2.86 to 2.55, and the K/Al from 1.38 to 1.14 for samples L170-20′ to L170-40′, respectively. It has been also observed that the synthesis temperature does not affect substantially on the Si/Al ratio in the crystalline LTL zeolite particles.

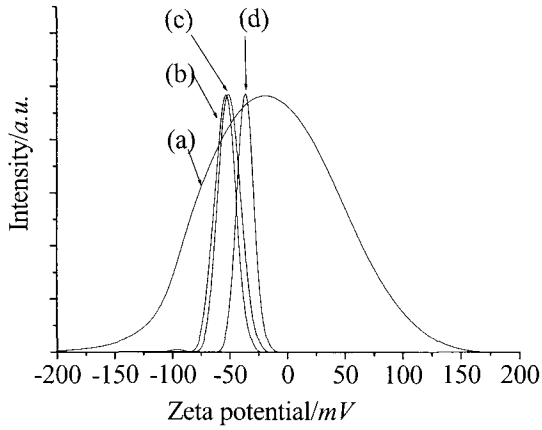

Fig. 3. Zeta potential measurements in initial precursor solution before (a) and (b) after purification, and in purified samples (c) L-170-30′ and (d) L-190-10′.

The nitrogen sorption data for the amorphous, intermediates and all crystalline samples were collected and depicted in Fig. 4. With increase the degree of crystallinity, the microporosity and the specific surface area of the samples are enlarged, i.e. the BET surface area calculated for the amorphous particles, L190-5′ and L-190-40′ were 237 m^2/g, 275 m^2/g and 345 m^2/g, respectively. Additionally, t-plot analysis of the nitrogen sorption data is performed; the shape of the t-plot curves where the adsorption isotherm is plotted in terms of the volume of gas adsorbed *vs* the statistical thickness of the adsorbate can be used to distinguish between microporous, non-porous and bi-modal micro/mesoporous solids (Fig. 4b). The extrapolation of these curves to y-axis gives volume occupied by the micropores. The samples L190-5′ and L-190-40′ show positive intercepts while the amorphous sample shows no microporous

adsorption. The presence of micropores is indicated by a positive intercept at the y-axis as shown in Fig. 4b, which is caused by a relatively large nitrogen uptake at a very low t-value that is due to the stronger adsorption of N_2 in the zeolite micropores.

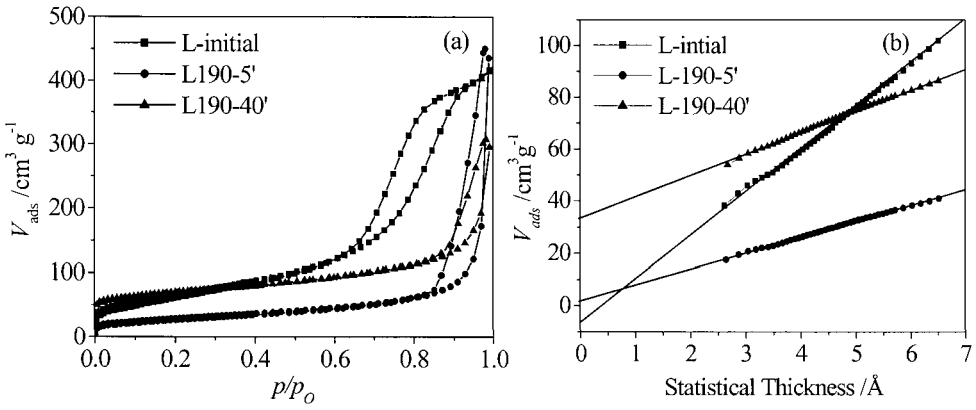

Fig. 4. (a) Nitrogen sorption isotherms and (b) T-plot data from purified amorphous particles, and samples L190-5′ and L-190-40′.

The crystallization process of LTL zeolite was followed with TEM, where was possible to distinguish between amorphous and crystalline areas in the individual particles formed spontaneously after mixing of all compounds. The dried amorphous nanoparticles in the precursor solution prior to MW treatment do not show any crystalline structures. Under MW heating, the amorphous nanoparticles do not change their morphology, however, some crystalline fringes that correspond to the LTL type structure occur (Fig. 5a). As can be seen the starting points for the nucleation are located inside of the amorphous agglomerates as well as at the periphery. The distance between the crystalline fringes is comparable with the channel diameter of LTL zeolite (~7.1 Å). Similar observations have been reported for zeolites synthesized from clear precursor solutions, where the nucleation has been observed in the middle and at the solid-liquid interface for LTA and FAU nanozeolite, respectively [20,21]. In addition, bigger agglomerates with separate parts having amorphous and crystalline appearances are recognizable in some of the intermediate samples (see Fig. 5b). The high degree of condensation/densification is observed in the aluminosilicate particles obtained after prolonged heating, where a total transformation of the amorphous particles into single and polycrystalline LTL zeolite is visible. The amorphous layers at the grain boundary between the individual LTL nanoclusters or amorphous shells have been seen only in the samples heated for very short time. In addition, the fully crystalline LTL samples synthesized at 190 °C consist of many aggregates composed of single nano-particles. The individual crystals have very rigid morphological appearance and cannot be described with one defined shaped. Under prolonged crystallization, the small nanoparticles are further growing and also formed bigger entities in which some of the crystalline fringes are well aligned or very randomly distributed.

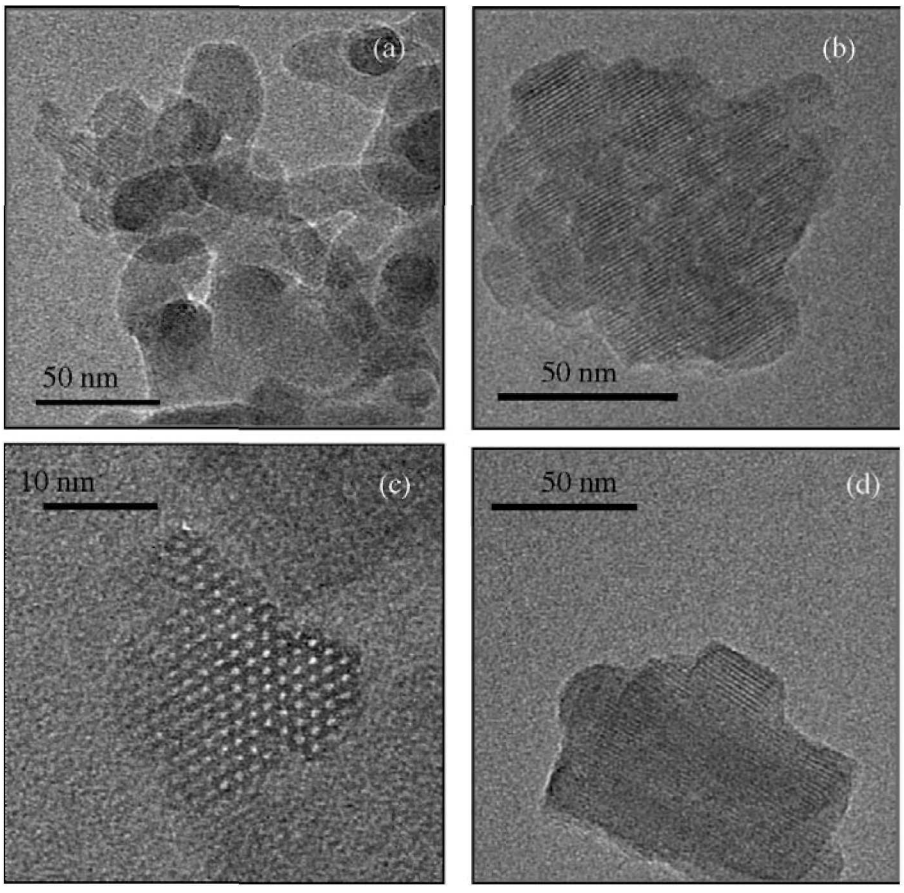

Fig. 5. HRTEM images of (a) L190-5′, (b) L190-10′ and (c) L170-30′ and (d) L190-40′.

The silica amorphous particles together with the aluminum and potassium are forming the amorphous agglomerates with a size of about 50-200 nm. After a short MW treatment, the first crystalline LTL zeolite nanoclusters are appearing in the amorphous aggregates having a size in the range of 5-10 nm. Further MW heating leads to the formation of bigger crystalline particles composed of partially aligned crystalline fringes and amorphous boundaries between. After prolonged MW heating almost a total transformation from amorphous into crystalline matter is observed. At a temperature of 170 °C, mainly single crystals are obtained, whereas at 190 °C the particles composed of nanosized multi-clusters are formed. The Si/Al and K/Al ratios in the amorphous and crystalline particles are very similar, however the excess of potassium is needed in order to keep the pH of the solution high and all the compounds dissolved in the clear solutions during the entire crystallization process, and to prevent the fast agglomeration and sedimentation of big particles.

4. CONCLUSIONS

Highly crystalline LTL zeolite was successfully synthesized via microwave heat treatment using potassium - aluminosilicate clear precursor solutions at temperatures 170 °C and 190 °C for 30 min and 10 min, correspondingly. Very fine and uniform single crystals are produced that appear to aggregate into polycrystals under prolonged crystallization time. The LTL zeolite synthesized at 170 °C has a narrow particle size distribution, and the increase of the microwave heating temperature yields crystals with different polycrystalline morphologies. However, the mechanism of crystallization for LTL zeolite prepared in conventional and microwave ovens is the same, and only the crystallization kinetics is different, i.e., the microwave heating decreases the time of synthesis in respect to the traditional heating under the same conditions. The reduction of the synthesis time was due to the uniformity of the heating stage by microwaves.

ACKNOWLEDGEMENT
his work was supported by the bilateral DFG/CNRS, BFHZ and Procope (DAAD).

REFERENCES

[1] B.J. Schoeman, J. Sterte, J.E. Otterstedt, Zeolites, 14 (1994) 208.
[2] J. Kecht, B. Mihailova, K. Karaghiosoff, S. Mintova, T. Bein, Langmuir, 20 (2004) 5271.
[3] A.E. Persson, B.J. Schoeman, J. Sterte, J.E. Otterstedt, Zeolites, 14 (1994) 557.
[4] A.E. Persson, B.J. Schoeman, J. Sterte, J.E. Otterstedt, Zeolites, 15 (1995) 611.
[5] Z. Guangyu, J. Sterte, B.J. Schoeman, Chem. Mater., 9 (1997) 210.
[6] S. Mintova, N. Petkov, K. Karaghiosoff, T. Bein, Mater. Sci. Eng., C19 (2002) 111.
[7] B.J. Schoeman, J. Sterte, J.E. Otterstedt, Zeolites, 14 (1994) 110.
[8] S. Mintova, M. Reinelt, T.H. Metzger, J. Senker, T. Bein, Chem. Commun., (2003) 326.
[9] M. Tsapatsis, M. Lovallo, T. Okubo, M.E. Davis, M. Sadakata, Chem. Mater., 7 (1995) 1734.
[10] C.S. Cundy, Collect. Czech. Chem. Commun., 63 (1998) 1699.
[11] X. Querol, A. Alastuey, A. Lopezosler, F. Plana, M.J. Andres, R. Juan, P. Ferrer, C.R. Ruiz, Environ. Sci. Technol., 31 (1997) 2527.
[12] a) L. Banaccorsi, E. Proverbio, Mater. Res. Innovat., 8 (2004) 53; b) Y. Han, H. Ma, S. Qiu, F.-S. Xiao, Microporous Mesoporous Mater., 30 (1999) 321.
[13] a) A. Arafat, J.C. Jansen, A. R. Ebaid, H. van Bekkum, Zeolites, 13 (1993) 162; b) O.G. Somani, A.L. Choudhari, B.S. Rao, S.P. Mirajkar, Mater. Chem. Phys., 82 (2003) 538; c) L. Banaccorsi, E. Proverbio, Mater. Res. Innovat., 8 (2004) 53.
[14] H. Katsuki, S. Furuta, S. Komarneni, J. Porous Mater., 8 (2001) 5.
[15] D.S. Kim, J.-S. Chang, J.-S. Hwang, S.-E. Park, J.M. Kim, Microporous Mesoporous Mater., 68 (2004) 77.
[16] R.M. Barrer, H.Z. Villinger, Z. Krsitallogr., 128 (1969) 352.
[17] a) G. Jacobs, W.E. Alvarez, D.E. Resasco, Appl. Catal. A: General, 206 (2001) 267; b) J.-L. Dong, J.-H. Zhu, Q.-H. Xu, Appl. Catal. A: General, 112 (1994) 105; c) M.J. Den Exter, H. van Bekkum, C.J.M. Rijn, F. Kapteijn, J.A. Mailijn, H. Schellevis, C.I.N. Beenakker, Zeolites, 19 (1997) 13.
[18] M.C. Hausladen, R.C. Cyganovich, H.Y. Huang, C.R.F. Lund, Appl. Catal. A: General, 219 (2001) 1.
[19] a) G. Calzaferri, S. Huber, H. Maas, C. Minkowski, Angew. Chem. Int. Ed., 42 (2003) 3732; b) H. Maas, A. Khatyr, G. Calzaferri, Microporous Mesoporous Mater., 65 (2003) 233; c) M. Yatskou, M. Meyer, S. Huber, M. Pfenniger, G. Calzaferri, Chem. Phys. Chem., 4 (2003) 567.
[20] S. Mintova, N.H. Olson, V. Valtchev, T. Bein, Science, 283 (1999) 958.
[21] S. Mintova, N.H. Olson, T. Bein, Angew. Chem. Int. Ed., 38 (1999) 3201.

Studies in Surface Science and Catalysis, volume 158
J. Čejka, N. Žilková and P. Nachtigall (Editors)

MCM-22 zeolite family and the delaminated zeolite MCM-56 obtained in one-step synthesis

Wieslaw J. Roth

ExxonMobil Research and Engineering Corp., Annandale, NJ 08801, USA
e-mail: wieslaw.j.roth@exxonmobil.com

Zeolite MCM-22 can form via a layered intermediate, which combines the potential of two classes of materials: zeolites and layered solids. Various discrete products with different arrangement of the MCM-22 monolayers have been recognized. A comprehensive overview of the resultant MCM-22 family is presented with the emphasis on synthetic routes and characterization, especially by X-ray diffraction, which allows identification of the various family members. One of the discussed materials, MCM-56, is identified as comprising a disordered collection of MCM-22 monolayers. It is the only delaminated zeolite available via a convenient one-step hydrothermal synthesis. MCM-56 may be a substrate for novel zeolitic materials with designed and tailored structures.

1. INTRODUCTION

A typical zeolite framework is assembled during hydrothermal synthesis by simultaneous growth in three dimensions. The product has a limited potential for post-synthesis structural modification. Zeolite MCM-22, which is an important industrial catalyst for ethylbenzene and cumene synthesis [1,2], showed unprecedented two synthetic pathways [3-5]. The framework was found to form via a layered intermediate in addition to the conventional direct route. Thus, the synthesis can produce a layered precursor (MCM-22-P) composed of 25 Å thick 'MCM-22 monolayers' [6], shown in Fig. 1. The complete 3-dimensional framework is obtained as the layers fuse with creation of T-O-T bridges upon calcination. MCM-22 monolayers have been found in different packing arrangements, giving rise to an unprecedented MCM-22 zeolite family with several distinct members. This unprecedented diversity generated synthetic and characterization challenges but also provided opportunities for new catalytic structures and expansion of basic knowledge and capabilities of zeolites.

2. EXPERIMENTAL

Hydrothermal syntheses of the MCM-22 materials with sodium hydroxide as base and hexamethyleneimine (HMI) as template were carried out in stirred stainless steel autoclaves under autogeneous pressure. The details of synthesis and characterization procedures have been described elsewhere [3-8]. Typical MCM-22-P synthesis mixture has the following molar composition: Si/Al =15, OH/Si=0.18, H_2O/Si= 45 and HMI/Si=0.35.

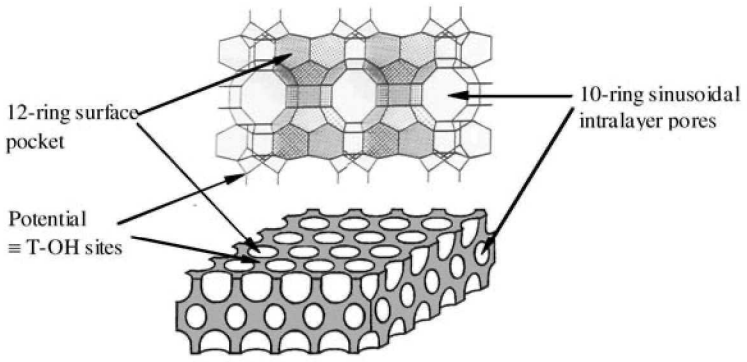

Fig. 1. Structure of the MCM-22 monolayer (top; side view) and its simplified representation showing the pore system and potential terminal TOH and interlayer bridging sites.

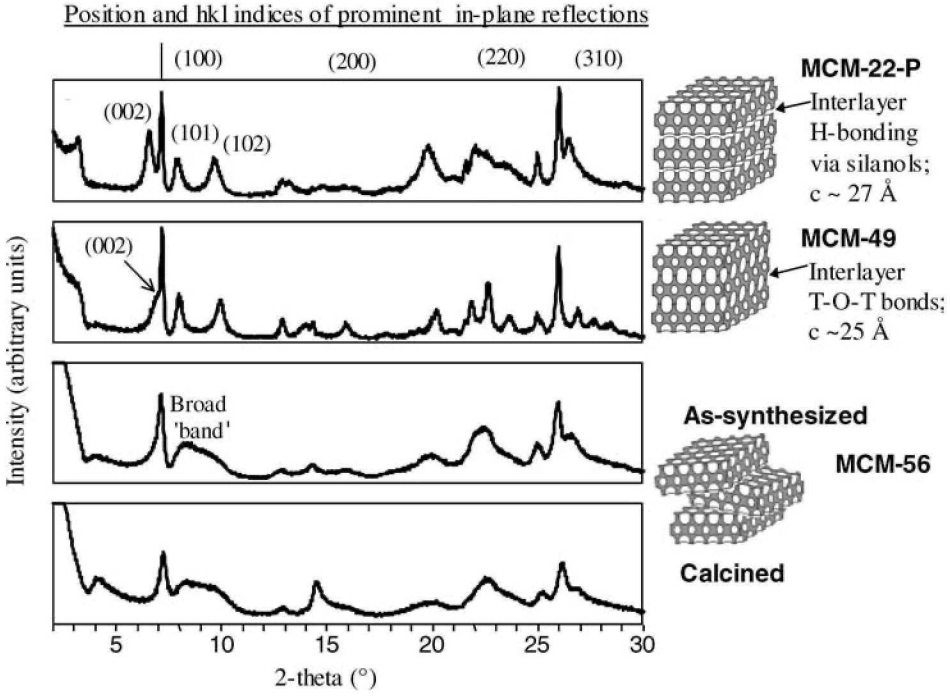

Fig. 2. XRD patterns and schematic structures of MCM-22-P, MCM-49 and MCM-56. The (hkl) Miller indices of selected reflections are provided.

3. RESULTS AND DISCUSSION

Hydrothermal synthesis of zeolite MCM-22 with sodium and hexamethyleneimine can result in two related but different end products, or their mixtures, depending on Si/Al ratio and

basicity [3-5]. Higher Si/Al favors a layered material, MCM-22 precursor (MCM-22-P), with a c lattice parameter ~27 Å. It consists of MCM-22 monolayers stacked and aligned in registry with hydrogen bonding between surface silanol groups. The precursor condenses into the 3-dimensional MCM-22 framework, designated MWW, upon calcination, which is accompanied by contraction of c to around 25 Å. The second possible end product, MCM-49, is the fully connected 3D zeolite framework (MWW) formed directly at lower Si/Al ratio of the synthesis mixture. Its lattice constants and consequently the XRD pattern are similar to those of calcined MCM-22. As shown in Fig. 2, both as-synthesized products (MCM-22-P and MCM-49) can be readily distinguished based on X-ray diffraction patterns.

The direct assembly of the MWW framework as MCM-49 proceeds via a distinct crystalline intermediate designated MCM-56 [7]. It is also layered and based on detailed characterization (see below) MCM-56 is identified as agglomerate of MCM-22 monolayers without in-registry alignment in the c direction and no interlayer links.

MCM-56 can be recognized as a discrete MCM-22 family member based on its unique XRD pattern (see Fig. 2). In the low angle region it resembles MCM-49 by having one distinct peak at 6-7.5° 2Θ due to coincidental overlap of (100) and (002) reflections. In contrast, for MCM-22-P the expanded unit cell results in (002) reflection located at 6.5° 2Θ and resolved from the (100) peak at 7.1° 2Θ. In the region around 26-29° 2Θ MCM-56 looks like MCM-22-P with only one distinct peak with a smooth descending tail, as shown in Fig. 4 in Ref. [5]. MCM-49 has 3 peaks with explicit (hkl) indices. The most significant feature of the MCM-56 XRD pattern is the peculiar broad peak stretching from 8 to 10° 2Θ (will be referred to as a 'band'). It replaces the resolved (101) and (102) interlayer reflections seen in MCM-22-P and MCM-49 and is attributed to lack of order in the corresponding c axis direction. This 'band' is crucial for identification of MCM-56 as a delaminated zeolite, which is shown in the section 1.4 below.

MCM-56 will be discussed further after presenting two topics concerning the MCM-22 family, i.e. preparation of the pillared derivative MCM-36 by exfoliation of the layered precursor and catalytic activity from the perspective of the MCM-22 monolayer structure.

3.1. Zeolite-based pillared molecular sieves from MCM-22-P

The layered nature of MCM-22-P was exploited to synthesize a zeolite-based pillared material, MCM-36, with interlayer pores having diameter in the range 25-30-Å [8]. These attributes make MCM-36 a unique mesoporous material due to its strong acid sites. Synthetically the pre-requisite separation of layers in MCM-22-P was challenging and not as facile as with previously studied layered solids [9]. The exfoliation was achieved using cationic surfactant in a hydroxide form (considered the evidence of strong hydrogen interlayer bonding). The potential pitfall of the high pH of the swelling environment is the possibility of partial dissolution of MCM-22-P and formation of mesoporous M41S [10]. The resultant M41S/MCM-22 mixture could be confused with MCM-36. This issue was discussed in detail in earlier publications [11,12].

In a separate study reported by others the surfactant swollen MCM-22-P was converted into a delaminated zeolite, ITQ-2, upon acid treatment, sonication and calcination [13,14]. MCM-56 and ITQ-2 are both disordered assemblies of MCM-22 monolayers but their exact relationship remains unclear. It was suggested that the latter has a 'house-of-cards' arrangement while the former may comprise stacked sheets in planar disorder [14]. For the time being to differentiate between the two materials we adopted graphic representations consistent with this proposal (Fig. 3), but the issue remains open.

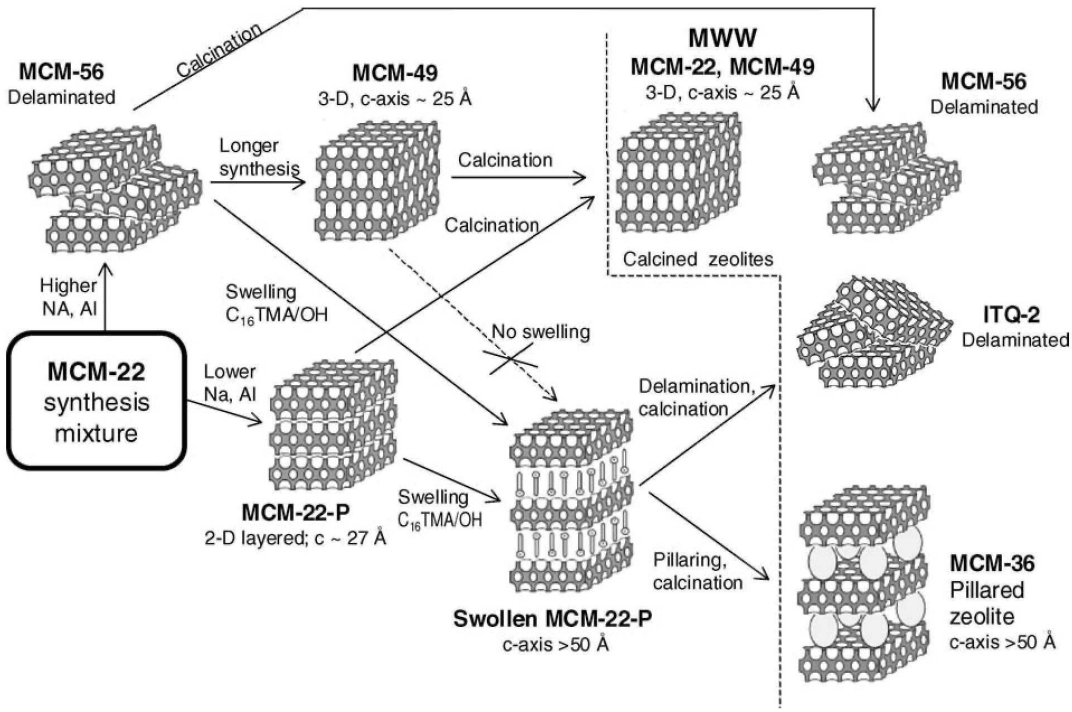

Fig. 3. MCM-22 family tree showing structural and synthesis relationships.

3.2. Pore system and catalytic activity of MCM-22 zeolite family.

The MCM-22 monolayer has two independent pore systems (see Fig. 1). One consists of 2-D interlayer sinusoidal channels with a medium size 10-ring aperture. On the surface there are 12-ring cavities (surface pockets), with about 7 Å diameter and 7 Å depth. Interestingly some T-atoms are common for both pore systems. The surface pockets are believed to be responsible for some of the unique catalytic behavior of the MCM-22 family zeolites, e.g. selectivity in EB and cumene synthesis with important commercial implications [1,2,15-17]. The condensation of MCM-22 monolayers with formation of T-O-T interlayer bridges creates 7 x 18 Å supercages from opposing surface pockets. The access to the supercages is constrained by 10-ring apertures, which limit access of larger molecules. Thus, keeping the MCM-22 monolayers separated may significantly increase the number of the surface pockets available for catalysis. MCM-36 represents one embodiment of this concept and indeed it shows improved catalytic performance in isoparaffin/olefin alkylation compared to MCM-22 and MCM-49 [18]. MCM-36 is a better catalysts in spite of lowered number of active sites per unit weight (and volume) stemming from the presence of inert amorphous silica as pillars (~ 50 % weight).

From the above perspective, MCM-56 offers special opportunities as a delaminated zeolite produced in a simple one-step synthesis. However, it also presents some novel challenges for synthesis, characterization and post-synthesis processing as discussed below [7,19].

3.3. MCM-56 synthesis

MCM-56 is an intermediate and has to be intercepted before or around the time it begins conversion to MCM-49. It is not known for certain when during MCM-56 crystallization the amorphous gel is consumed completely and formation of two or more fused monolayer structures commences. The optimal time window is presumed to last for about 2-3 hours. This onset of MCM-49 is indicated by emergence of a dip in the 8-10° broad peak, which can be interpreted as start of the resolution into separate interlayer reflections (101) and (102) (Fig. 4).

3.4. Identification of MCM-56 as a single layer zeolite

Electron microscopy can visualize single layers in delaminated zeolites like MCM-56 [20] but cannot prove their ubiquity. Among bulk techniques XRD provides the evidence supporting assignment of the monolayer structure. First, the prominent and the only well defined reflections are the in-plane ones with (hk0) indices (see Fig. 2). Second, the reflections equivalent to the interlayer ones for MCM-22/49 with non-zero l (hkl) indices, especially the (00l) series, cannot be located and assigned. A special program for calculating simulated XRD patterns factoring in a finite crystal size have been applied with the assumption of a one unit cell crystal thickness [21]. It confirmed the unusual features observed experimentally, in particular the broad 'band' at 8-10° 2Θ as well as non-Bragg reflections below 5° 2Θ. The 8-10° 'band' is critical for identification of MCM-56 and detection of the beginning of its conversion to multilayer species (MCM-49). It is notable that the same 'band' is also the diagnostic feature for layer exfoliation in MCM-36 [8], which as a pillared zeolite has disrupted and apparently misaligned layers.

MCM-56 demonstrates improved surface accessibility for larger molecules. It is manifested in enhanced adsorption capacity for larger hydrocarbon molecule and faster uptake rate compared to MCM-22 [7]. A rather unique manifestation of the enhanced accessibility of the external surface of the layers is revealed upon treatment with surfactants

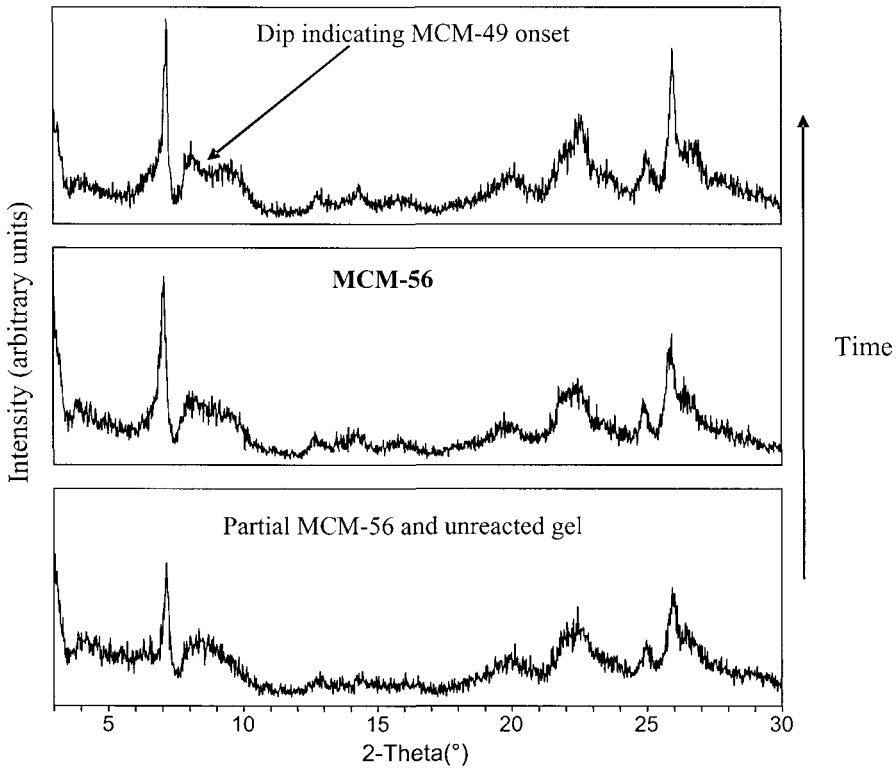

Fig. 4. XRD patterns during MCM-56 synthesis and the onset of conversion to MCM-49.

aimed to produce a composite analogous to swollen the MCM-22-P. As described in earlier publications swelling of MCM-22-P with surfactants required high pH and special circumstances [8,11,12]. Thus, no swelling was achieved with the combination of a small cation hydroxide, tetramethylammonium hydroxide, TMA-OH and the surfactant halide, hexadecyltrimethylammonium chloride, CTMA-Cl. It was rationalized by TMA diffusion into the interlayer region, which apparently prevented intercalation of CTMA and swelling of MCM-22-P. In contrast, when a base with much larger cation, i.e. tetrapropylammonium (TPA-OH) was used, the cation appeared too big for migration between layers and the surfactant intercalation with concomitant swelling was favored. In the case of MCM-56, the small base TMA-OH and CTMA-Cl combination does to generate the MCM-22 layer/surfactant bilayer (swollen) composite. The apparent absence of size exclusion effects supports more open and quite accessible surface in MCM-56.

3.5. MCM-56 - potential as a catalyst

MCM-56 can be processed and used as a catalyst in a manner similar to other zeolites. Often such standard approach does not result in MCM-56 showing advantage in comparison to MCM-22 and MCM-49. However, when strong active sites on the surface and an open structure may play an important role in a catalytic process MCM-56 is found desirable. An

example to this effect is observed with the ethylbenzene synthesis in liquid phase, where MCM-56 showed higher activity than both MCM-22 and MCM-49 [22].

Compared to other zeolites MCM-56 offers new opportunities but one must be aware of accompanying challenges and pitfalls. Typical zeolites have majority of active sites inside crystals, which provides a degree of protection and reduced sensitivity to the outside environment. MCM-56's unique activity potential is associated with the external surface, which is quite vulnerable to blockage (by detritus or layer overlap) or degradation, such as increased dealumination. In order to take advantage of the unique attributes of MCM-56 may require new post-synthesis processing methodology.

The biggest opportunity seems to lie with the post-synthesis structural and compositional modification of MCM-56. As indicated, conventional zeolites are not particularly amenable to structural improvements once crystallization is complete. For MCM-56 the manipulation of orientation and spacing of monolayers offers large pore and/or tailored structures with strong acid sites. The pillared MCM-36 [8,23] and the delaminated derivatives [13,14] illustrate this but other more refined and possibly better designed materials can be envisioned. Other zeolites, such as ferrierite, have been found to form layered precursors too. They can be delaminated, swelled and pillared, resulting in a zeolite family similar to MCM-22 [24]. However, MCM-56 remains unique as the only delaminated zeolite obtained by a direct one-step synthesis.

4. CONCLUSIONS

Three-dimensional MWW framework is obtained via layered precursors either directly (MCM-56 then MCM-49) or indirectly (MCM-22-P transforming upon calcination to MCM-22). The MCM-22 monolayers can adopt or be manipulated into different spatial arrangements as exemplified by MCM-36 (pillared derivative) and ITQ-2 (delaminated zeolite). MCM-56, as a delaminated zeolite obtained by facile one-step synthesis, offers novel opportunities for designed and/or tailored zeolite based catalysts.

REFERENCES

[1] (a) T.F. Degnan, Jr., C.M. Smith and C.R. Venkat, Applied Catalysis, A: General 221 (2001) 283. (b) J.S. Beck, A.B. Dandekar and T.F. Degnan, Jr., in M. Guisnet and J.-P. Gilson (eds.), Zeolites for Cleaner Technologies, Imperial College Press, London, 2002, 223.

[2] J. Čejka and B. Wichtlerová, Catal. Rev., 44 (2002) 375.

[3] M.K. Rubin and P. Chu, Composition of Synthetic Porous Crystalline Material, Its Synthesis and Use, US Patent No. 4 954 325 (1990).

[4] M.E. Leonowicz, J.A. Lawton, S.L. Lawton and M.K. Rubin, Science (Washington, DC) 264 (1994) 1910.

[5] S.L. Lawton, A.S. Fung, G.J. Kennedy, L.B. Alemany, C.D. Chang, G.H. Hatzikos, D.N. Lissy, M.K. Rubin and H.-K.C. Timken, J. Phys. Chem., 100 (1996) 3788.

[6] S.L. Lawton, M.E. Leonowicz, R.D. Partridge, P. Chu and M.K. Rubin, Microporous Mesoporous Mater., 23 (1998) 109.

[7] A.S. Fung, S.L. Lawton, W.J. Roth, Synthetic Layered MCM-56, Its Synthesis and Use, US Patent No. 5 362 697 (1994).

[8] W.J. Roth, C.T. Kresge, J.C. Vartuli, M.E. Leonowicz, A.S. Fung and S.B. McCullen, in H.K. Beyer, H.G. Karge, I. Kiricsi and J.B. Nagy (eds.), Catalysis by Microporous Materials, Stud. Surf. Sci. Catal. Vol. 94, Elsevier, New York, 1995, 301.

[9] S.M. Auerbach, K.A. Carrado and P.K. Datta, Hanbook of Layered Materials, Marcel Dekker, New York, 2004.

[10] C.T. Kresge, J.C. Vartuli, W.J. Roth and M.E. Leonowicz, in O. Terasaki (ed.), Mesoporous Crystals and Related Nano-structured Materials, Stud. Surf. Sci. Catal. Vol. 148, Elsevier, New York, 2004, 53.
[11] W. J. Roth and J. C. Vartuli, in A. Sayari, M. Jaroniec and T.J. Pinnavaia (eds.), Nanoporous Materials II, Stud. Surf. Sci. Catal. Vol. 129, Elsevier, New York, 2000, 501.
[12] W. J. Roth and J. C. Vartuli, in A. Sayari, and M. Jaroniec (eds.), Nanoporous Materials III, Stud. Surf. Sci. Catal. Vol. 141, Elsevier, New York, 2002, 273.
[13] A. Corma, V. Fornes, S.B. Pergher, T.L.M. Massen and J.G. Buglass, Nature 396 (1998) 353.
[14] A. Corma, U. Diaz, V. Fornes, J.M. Guil, J. Martinez-Triguero, E.J. Creyghton, J. Catal., 191 (2000) 218.
[15] G.R. Meima, M.J.M. Van der Aalst, M.S.U. Samson, J.M. Garces and J.G.Lee JG, Jahrgang, 112 (1996) 315.
[16] J.A. Horsley, Chemtech, October (1997) 45.
[17] H. Du and D.H. Olson, J. Phys. Chem. B, 106 (2002) 395.
[18] C.T.W. Chu, A. Husain, K.M. Keville and D.N. Lissy, Catalyst and Process for Isoparaffin-Olefin Alkylation, US Patent No. 5 354 718 (1994)..
[19] W.J. Roth and D. N. Lissy, 13th Int. Cong. Catal., Book of Abstracts, p. 118 (P1-050).
[20] N. Xu, T. Wu, D. Wang, P. Wu, Q. Kan, J. Sun, Gaodeng Xuexiao Huaxue Xuebao, 22 (2001) 1898.
[21] G.G. Juttu and R.F. Lobo, Microporous Mesoporous Mater., 40 (2000) 9.
[22] J.C. Cheng, A.S. Fung, D.J. Klocke, S.LK. Lawton, D.N. Lissy, W.J. Roth, C.M. Smith and D.E. Walsh, Process for Preparing Short-chain Alkylaromatic Compounds (with a Zeolite Catalyst). US Patent No. 5 453 554 (1995).
[23] J.-O. Barth, A. Jentys, J. Kornatowski and J.A. Lercher, Chem. Mater., 16 (2004) 724.
[24] A. Corma, U. Diaz, M.E. Domine and V. Fornes, J. Am. Chem. Soc., 122 (2000) 2804.

Studies in Surface Science and Catalysis, volume 158
J. Čejka, N. Žilková and P. Nachtigall (Editors)

Direct synthesis of mesoporous Fe-MFI zeolite

J.B. Taboada[a], A.R. Overweg and P.J. Kooyman[b]

[a]Department of Radiation, Radionuclides & Reactors, Faculty of Applied Sciences, Delft University of Technology, Mekelweg 15, 2629 JB Delft, The Netherlands

[b]DCT and NCHREM, Faculty of Applied Sciences, Delft University of Technology, Julianalaan 136, 2628 BL Delft, The Netherlands

A novel method for the direct synthesis of mesoporous Fe-MFI zeolite is reported. Mesopore formation was observed over a whole range of as-synthesised Fe-MFI zeolites with varying iron (0.075 – 0.6 wt%) and aluminium (0 – 1.1 wt%) concentrations. The main difference of this method to conventional synthesis of Fe-MFI zeolites is that instead of adding iron salts (eg $Fe(NO_3)_3$) to the solution gel, we prepared a synthesis gel starting from metallic iron foil that was dissolved in nitric acid. Transmission electron micrographs show a broad mesopore-size distribution in all as-synthesised Fe-MFI zeolite samples. The mesopores are retained after calcination as well as after subsequent mild steaming.

1. INTRODUCTION

Fe-MFI has attracted increasing attention due to its ability to catalyse various reactions such as the selective catalytic reduction (SCR) of NO_x [1,2], the direct decomposition of N_2O [3], and recently the one-step hydroxylation of benzene to phenol using N_2O as oxidant [4,5]. However, due to the microporous character of the zeolite, the presence of intracrystalline diffusion limitations sometimes limits its catalytic performance. Due to the limited zeolite micropore size (about 0.55 nm), even the reaction of small organic molecules is often hindered by diffusion limitations. To improve the efficiency of zeolite-based catalysts, diffusion-related problems can be minimised by introducing mesopores in the zeolite crystal. These mesopores improve access to the zeolite pore system by increasing diffusion velocities. A recently reported example of the use of such secondary mesopores is the improved performance of mesoporous MFI zeolite in the catalytic cracking and isomerisation of *n*-hexadecane [6].

Several methods have been investigated to alter the properties of zeolites to create additional porosity without destroying their intrinsic properties. A conventional method is by extraction of the tetrahedrally coordinated aluminium (dealumination) [7], from the zeolite framework by steam treatment followed by acid leaching. However, the dislodgement of framework aluminium unavoidably alters the acidic properties of the zeolite. A much better

method of introducing significant mesoporosity in MFI-type zeolites is by desilication in alkaline media (eg NaOH solution), which preferentially removes silicon from the zeolite framework [8 - 11]. Nevertheless, these well-established methodologies to create mesoporosity in zeolites require post-treatment steps of the parent zeolite. In order to avoid this kind of time-consuming and expensive post-treatments, it is of practical importance to develop a direct route to synthesise mesoporous zeolites. A relatively novel approach to introduce mesopore formation is by carbon templating, where porous carbon or carbon nanotubes are included during the synthesis of the zeolite. This creates mesopores in the zeolite matrix after combustion of the carbon at higher temperature [12 - 14]. Although substantial mesoporosity is obtained by this method, the crystallinity of the final material is often a major issue, which requires time-consuming optimisation of the synthesis parameters.
In this paper, we report a novel method for the direct synthesis of mesoporous Fe-MFI zeolites. Fe-MFI zeolites with varying iron (0.075 – 0.6 wt%) and aluminium (0 – 1.1 wt%) concentrations were synthesized. The as-synthesised Fe-MFI zeolites (which still contain the organic template) contain a substantial mesoporosity with a broad pore-size distribution as deduced from transmission electron microscopy (TEM). The mesopores are retained after calcination as well as after subsequent mild steaming.

2. EXPERIMENTAL

2.1. Fe-MFI synthesis

The appropriate amount of metallic iron foil was dissolved in excess 65% (14 N) nitric acid. The obtained iron solution was diluted to 20 ml with water (milliQ quality) and subsequently titrated with tetrapropylammonium hydroxide (TPAOH, Alfa Aesar, 40% w/w in H_2O) to pH = 2.3 (this is the equivalent pH of $Fe(NO_3)_3.9H_2O$, Merck, 99%, in 20 ml water). The appropriate amount of aluminium nitrate ($Al(NO_3)_3.9H_2O$, Merck, 98.5%) was added to the iron-containing solution. A zeolite synthesis gel was then prepared by adding in a drop-wise manner and under stirring a mixture of TEOS (Acros, 98%) as silica source, TPAOH (Alfa Aesar, 40% w/w in H_2O) as organic template, and sodium hydroxide to a well-stirred Fe solution. The nominal molar ratios of TPAOH/Si and NaOH/Si were kept constant at 0.1 and 0.2 respectively.

Hydrothermal synthesis was performed at 448 K for 5 days in a rotated (~20 rpm) Teflon-lined autoclave. The resulting as-synthesised zeolites were filtered and washed several times with demineralised water until the pH of the water was neutral. Finally, the materials were dried at 353 K overnight.

2.2. Characterisation

2.2.1. Elemental analysis

The elemental analysis of the as-synthesised materials was carried out by inductively coupled plasma optical emission spectroscopy (ICP-OES), using a Perkin-Elmer Plasma 40 (Si) and Optima 3000DV (axial).

2.2.2. Scanning electron microscopy

Scanning electron microscopy (SEM) was performed using a Philips XL 20 microscope on samples coated with gold to decrease charging.

2.2.3. Transmission electron microscopy

Transmission electron microscopy (TEM) was performed using either a Philips CM30T or CM30UT electron microscope with a LaB_6 filament or FEG as the source of electrons respectively, operated at 300 kV. Samples were mounted on Quantifoil® microgrid carbon polymer supported on a copper grid by placing a few droplets of a suspension of ground sample in ethanol on the grid, followed by drying at ambient conditions.

3. RESULTS AND DISCUSSION

Elemental analysis data for the as-synthesised Fe-MFI zeolites are given in table 1. Comparison of the molar ratios for Si/Fe and Fe/Al of the as-synthesised Fe-MFI samples to their corresponding synthesis gels shows that the ratio as weighed in into the synthesis gel is reproduced in the final Fe-MFI crystals. This indicates that our new synthesis method is efficient as well as reproducible.

Table 1
Elemental analysis of the as-synthesized Fe-MFI zeolites

sample	Si (w%)[a]	Al (w%)[a]	Fe (w%)[a]	Si/Al (zeolite)[b]	Si/Fe (zeolite)[b]	Si/Al (gel)[c]	Si/Fe (gel)[c]
Fe-MFI (1:4)	39.0	1.10	0.56	33	141	36	152
Fe-MFI (1:8)	39.0	1.16	0.28	33	279	36	300
Fe-MFI (1:16)	39.0	1.15	0.14	33	558	36	600
Fe-MFI (1:0)	39.7	0.00	0.50	∞	154	∞	152

[a] weight percent in the crystalline samples
[b] molar ratio in the crystalline samples
[c] molar ratio in the solution gel

X-ray diffraction measurements [15] of these samples show that all as-prepared zeolites have the MFI-type structure with a high degree of crystallinity. No other crystalline phases are detected in the X-ray diffractograms.

SEM images of the as-synthesised materials show morphologies as expected for MFI-type zeolites: almost spherical clusters of small rods and large twinned or multiple-twinned crystals. A typical SEM image for each sample is shown in Fig. 1.

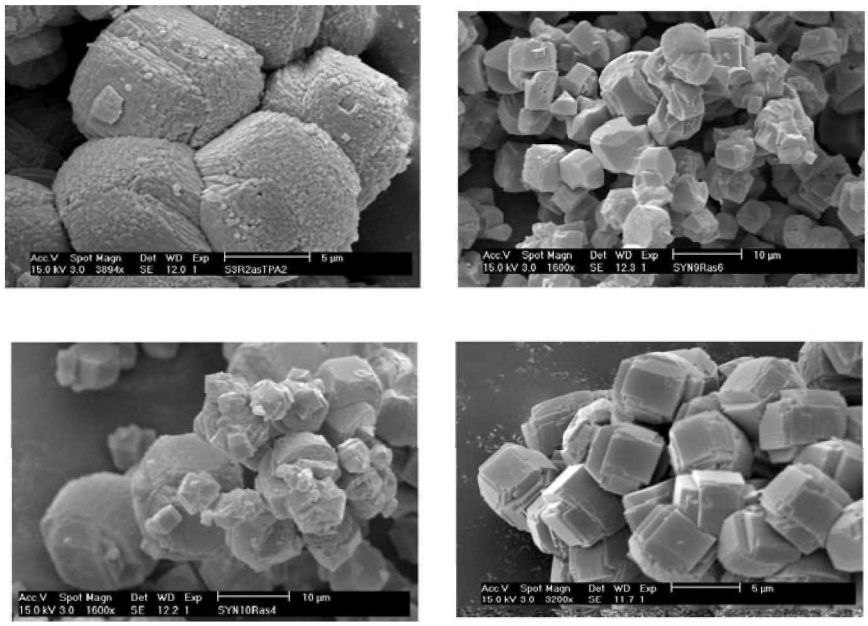

Fig. 1. SEM images of Fe-MFI. Top left: (1:4); top right: (1:8); bottom left: (1:16); bottom right: (1:0).

TEM shows that all as-prepared Fe-MFI samples contain a substantial amount of mesopores with a broad pore size distribution in addition to the ordinary MFI pore system. Next to zeolitic material, no amorphous debris was observed either in TEM or SEM investigation. Fig. 2 shows a representative TEM image of the 1:4 sample. It contains well-formed mesopores throughout the zeolite crystals. Fig. 3 shows a representative TEM image of the 1:8 sample. It contains less well-formed mesopores. Fig. 4 shows a representative TEM image of the 1:16 sample. This sample contains well-formed mesopores again. Fig. 5 shows a representative TEM image of the 1:0 sample. Even the Fe-only (ie, Al-free) material contains many well-formed mesopores. The mesopore size distribution is very broad for all samples, with pores ranging up to 100 nm.

In Fe-containing zeolites, one of the main concerns is the prevention of formation of crystalline clusters of iron oxide. These clusters are often formed upon severe steaming, as is required to obtain mesopores. However, mild steaming is already sufficient to activate the desired isolated iron species that give rise to catalytic activity. In our materials, the direct generation of mesopores in the zeolite crystals upon zeolite synthesis means that severe steaming to create mesopores is no longer necessary. A mild steaming treatment to activate the isolated iron species suffices and clustering of iron into inactive crystalline iron oxide nanoparticles is prevented.

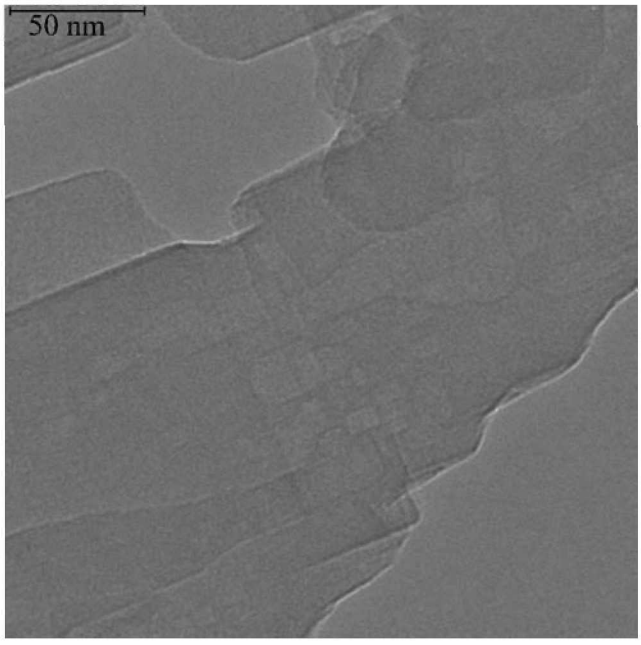

Fig. 2. Representative TEM image of Fe-MFI (1:4).

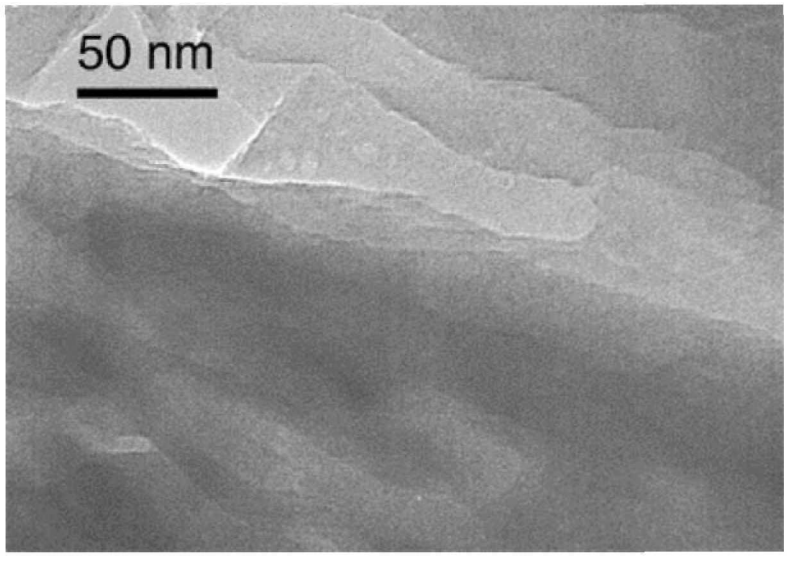

Fig. 3. Representative TEM image of Fe-MFI (1:8).

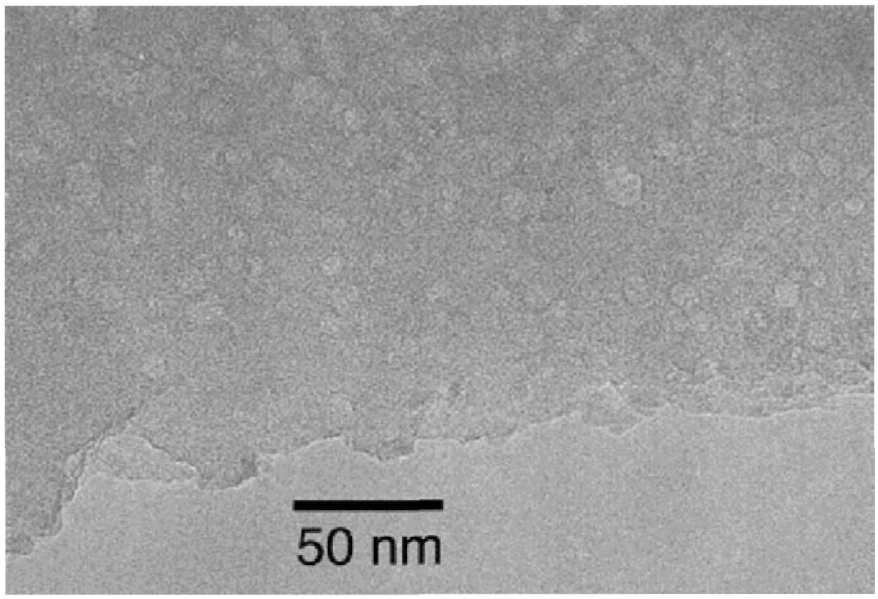

Fig. 4. Representative TEM image of Fe-MFI (1:16).

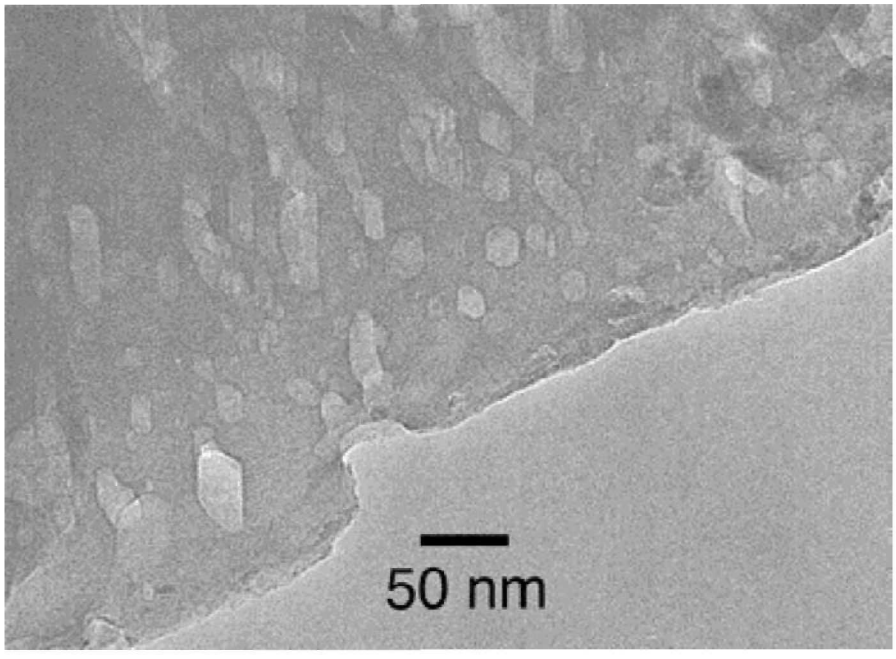

Fig. 5. Representative TEM image of Fe-MFI (1:0).

The presence of only isolated iron species in these samples without any discrete crystalline nanoparticles has been proven using Mössbauer spectroscopy [15]. The absence of crystalline nanoparticles in these materials is now also shown using TEM at very high magnification. Fig. 6 shows a representative TEM image of these materials. Only amorphised zeolite is visible for our samples. This is due to the fact that high magnification TEM imaging requires high electron beam intensity, which generally amorphises zeolite structures within seconds. For conventionally prepared Fe-MFI zeolites, however, crystalline nanoparticles are observed in high resolution TEM images [16]. This is due to the fact that occluded species such as metal particles or, in this case, possibly present iron oxide crystallites are embedded in the amorphous debris of the zeolite after amorphisation and are locked in at their original location in the zeolite pore system.

All samples described in this paper have been subjected to calcination followed by mild steaming. Both these treatments leave the pore system of the materials intact, opening up a world of possibilities for improved catalytic performance. Detailed characterisation of the calcined, H^+ and steamed forms of these materials is published elsewhere [17].

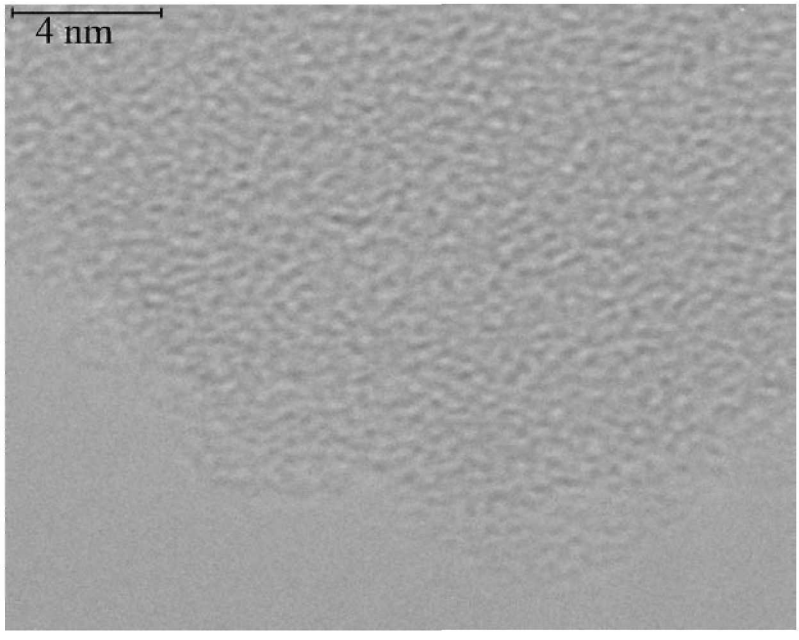

Fig. 6. Typical high magnification TEM image of Fe-MFI showing the absence of small crystallites of iron oxide.

4. CONCLUSIONS

A new synthesis method for iron-containing MFI zeolite yields a hierarchical pore system of large mesopores in addition to zeolite micropores by direct synthesis. As mesopores are already present in the as-synthesised materials, standard calcination to remove the template

followed by mild steaming to activate the isolated iron species suffices to obtain catalytically active materials. The previously required severe steaming in order to create mesopores to overcome diffusion limitations during catalytic processes is no longer necessary and thus sintering of iron species into iron oxide crystalline nanoparticles can be prevented.

REFERENCES

[1] A.A. Battiston, J.H. Bitter, D.C. Koningsberger, Catal. Lett. 66 (2000) 75.
[2] L.J. Lobree, I. Hwang, J.A. Reimer, A.T. Bell, Catal. Lett. 63 (1999) 233.
[3] F. Kapteijn, G. Marbán, J. Rodríguez-Mirasol, J.A. Moulijn, J. Catal. 167 (1997) 256.
[4] G.I. Panov, Cattech 4 (2000) 18.
[5] A. Ribera, I.W.C.E. Arends, S. de Vries, J. Pérez-Ramírez, R.A. Sheldon, J. Catal. 195 (2000) 287.
[6] C.H. Christensen, I. Schmidt, C.H. Christensen, Catal. Comm. 5 (2004) 543.
[7] M. Müller, G. Harvey, R. Prins, Microporous Mesoporous Mater. 34 (2000) 135.
[8] J.C. Groen, J.C. Jansen, J.A. Moulijn, J. Pérez-Ramírez, J. Phys. Chem. B 108 (2004) 13062.
[9] J.C. Groen, L.A.A. Peffer, J.A. Moulijn, J. Pérez-Ramírez, Microporous Mesoporous Mater. 69 (2004) 29.
[10] T. Suzuki, T. Okuhara, Microporous Mesoporous Mater. 43 (2001) 83.
[11] M. Ogura, S.H. Shinomiya, J. Tateno, Y. Nara, E. Kikuchi, M. Matsukata, Chem. Lett. (2000) 882.
[12] I. Schmidt, A. Boisen, E. Gustavsson, K. Ståhl, S. Pehrson, S. Dahl, A. Carlsson, C.J.H. Jacobsen, Chem. Mater. 13 (2001) 4416.
[13] Y. Tao, H. Kanoh, K. Kaneko, J. Am. Chem. Soc. 125 (2003) 6044.
[14] A.H. Janssen, I. Schmidt, C.J.H. Jacobsen, A.J. Koster, K.P. de Jong, Microporous Mesoporous Mater. 65 (2003) 59.
[15] J.B. Taboada, A.R. Overweg, M.W.J. Crajé, I.W.C.E. Arends, G. Mul, A.M. van der Kraan, Microporous Mesoporous Mater. 75 (2004) 237.
[16] J. Perez-Ramirez, G. Mul, F. Kapteijn, J.A. Moulijn, A.R. Overweg, A. Domenech, A. Ribera, I.W.C.E. Arends, J. Catal. 207 (2002) 113.
[17] J.B. Taboada, A.R. Overweg, P.J. Kooyman, I.W.C.E. Arends, G. Mul, J. Catal. (2005) (in press).

Studies in Surface Science and Catalysis, volume 158
J. Čejka, N. Žilková and P. Nachtigall (Editors)

Control of zeolite surface nucleation

J.R. Agger,[a] L.I. Meza,[b] C.S. Cundy,[b] R.J. Plaisted[b] and M.W. Anderson.[b]

[a]Department of Chemistry, University of Leeds, Leeds LS2 9JT, United Kingdom.

[b]School of Chemistry, University of Manchester, P.O. Box 88, Manchester M60 1QD, United Kingdom.

A semi-continuous flow reactor was used to mimic gel supersaturation conditions at both intermediate and terminal stages of zeolite batch synthesis. Flow of nutrient into the reactor was repeatedly switched on and off. Analysis of the crystals by atomic force microscopy (AFM) reveals that samples removed under simulated conditions of gel depletion are topographically similar to samples prepared by normal batch synthesis, with very low levels of surface nucleation. Samples removed under conditions of high gel supersaturation appear to be growing by the same mechanism however rates of surface nucleation are increased by up to two orders of magnitude. Crystal growth resumes unperturbed upon reconnection of the nutrient feed. Ability to exert control over surface nucleation rates has important ramifications for the potential control of defect inclusion.

1. INTRODUCTION

In recent years great progress has been made towards improving our understanding of zeolite crystal growth mechanisms using the techniques of AFM [1-11], SEM [12-14], TEM [15,16], and simulation [16,17]. Crystal growth most probably occurs via the condensation of monomeric and small oligomeric species until a surface energy minimum is reached, resulting in terrace formation. Surface energy minima and thus terrace heights are generally commensurate with some aspect of the unit cell. Analysis of experimental data reveals lateral terrace spreading rates are far greater than successive terrace nucleation rates – this concurs with our general perception of zeolite crystal facets as being effectively flat. However, it is important to note that the wealth of data published to date has been acquired from batch synthesised crystals.

SEM studies of sizes of zeolite crystals prepared by batch synthesis reveal an initial induction period followed by a sustained period of linear growth [18] which eventually tails off, as shown in Fig. 1. Linear growth occurs under conditions of high gel supersaturation when the rate of nutrient dissolution is greater than the rate of nutrient uptake onto the crystals. Over time, decrease of the former coupled to increase of the latter, as the crystals grow in surface area, results in decreasing supersaturation levels, gel depletion and the slow down and ultimate cessation of crystal growth.

In this paper we present a comparative AFM study of crystals recovered from gels under carefully controlled conditions of high and low supersaturation. The principle aims are to provide insight into earlier stages of zeolite crystal growth and to assess the possibility of using gel supersaturation as a means of influencing crystal growth.

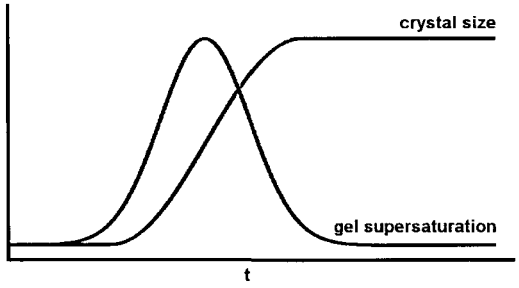

Fig. 1. The evolution of crystal size and gel supersaturation during batch synthesis of a zeolite.

2. EXPERIMENTAL

2.1 Synthesis

1.6 μm long, un-twinned, lozenge-shaped silicalite seed crystals were synthesised as detailed elsewhere [19]. Seed crystals at a concentration of 9.5 g L^{-1} in their spent mother liquor were placed in a specially modified 1 L autoclaved reactor stirred at 300 rpm. The slurry was heated to 130 °C over a period of 30 mins and then left to equilibrate for 3 h, after which nutrient feed was switched on at an initial rate of 90 mL h^{-1}. The nutrient feed comprised silica sol, tetrapropylammonium bromide and sodium hydroxide with the following composition [Si] = 0.48M, Si:OH = 8.72 and Si:TPA = 10.00. Samples were removed at regular intervals in order to maintain an effectively constant working volume in the reactor. In the absence of secondary nucleation, the assumption of effective stirring to create homogeneous crystal distribution enabled calculation and monitoring of the required nutrient feed to produce constant linear crystal growth rates of 0.4 μm h^{-1}. Three times during the course of the reaction the nutrient feed was disconnected for periods of *ca.* 16 h allowing gel depletion akin to the latter stages of a normal batch synthesis. Quoted reaction times refer to the total period for which the nutrient feed was switched on. Periods of disconnection are not quantified, however, with reference to samples withdrawn prior to and immediately after such periods of disconnection an asterisk is used to distinguish the latter.

2.2 Atomic force microscopy

Atomic force micrographs were recorded with a Veeco Multimode Microscope and Nanoscope IIIa controller operating in contact mode, recording height and deflection information at 1 Hz scan rates, with 0.58 N m^{-1} force constant cantilevers. Sample preparation involves pipetting one drop of an ethanolic suspension of the crystals onto an AFM stub with a flat coating of CrystalBond™ thermoplastic (Agar Scientific Ltd) preheated to 50 °C. After 45 seconds the disk is removed from the heat source and allowed to cool, thus fixing the crystals.

3. RESULTS AND DISCUSSION

Solution and gel silica concentrations were measured by chemical means for each sample removed from the reactor. Solution silica comprises reactive monomeric and small oligomeric species. Gel silica comprises larger oligomeric and polymeric silica that may be present as

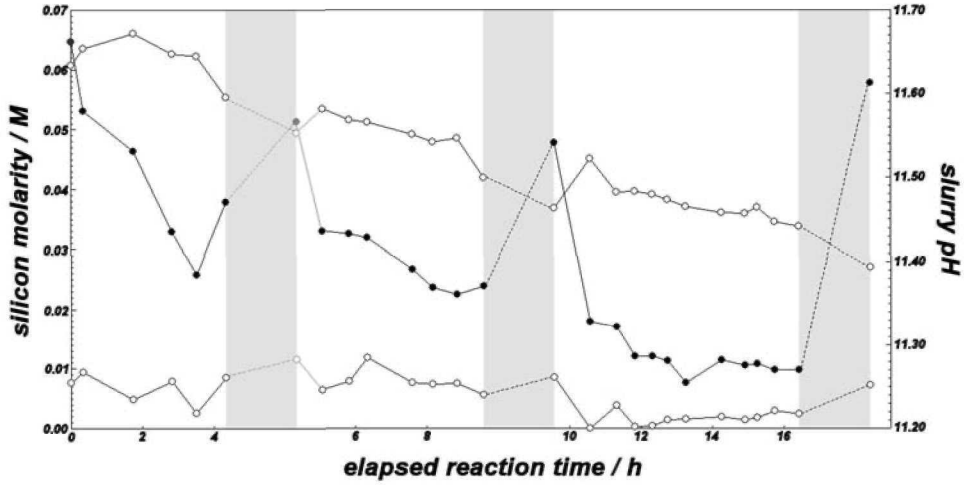

Fig. 2. Reaction monitoring. The solid circle trace records pH. The upper hollow circle trace records the concentration of solution silica whilst the lower one records the concentration of gel silica. The grey sections (not shown to scale) represent times at which the feed was disconnected i.e. at 4.3, 9.6 and 16.4 h. No readings were recorded immediately prior to reconnection of the feed after the first disconnection, consequently only estimated values are shown.

visible gel in a separable solid phase or as colloid dispersed in the form of a sol. Extensive details of these measurements are quoted elsewhere[20]. Sample pH was also recorded and all the data is plotted in Fig. 2. The gradual drop in sample pH as the reaction proceeds may be attributed to mineralisation of the silica out-stripping condensation of silica onto the crystals. This trend is reversed during each period of gel depletion as much of the silica condenses onto the crystals.

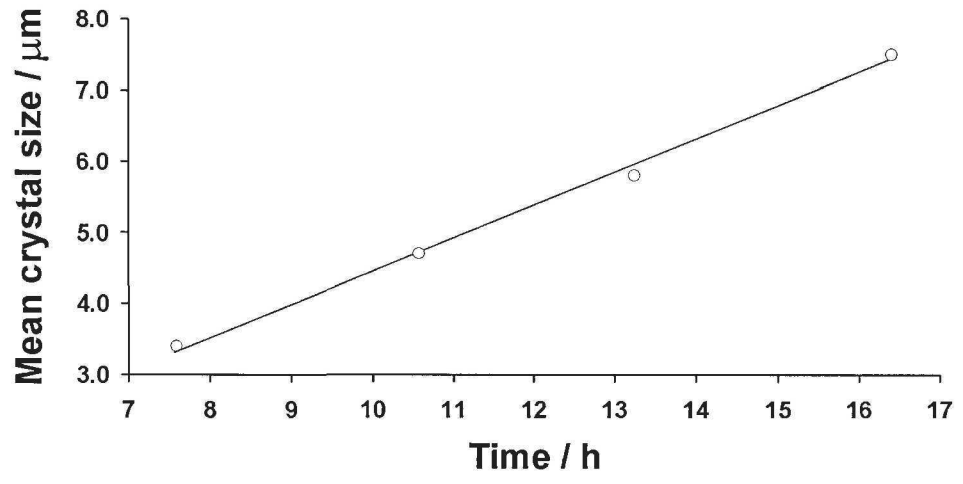

Fig. 3. Mean sample crystal sizes, estimated from scanning electron micrographs, plotted against growth time.

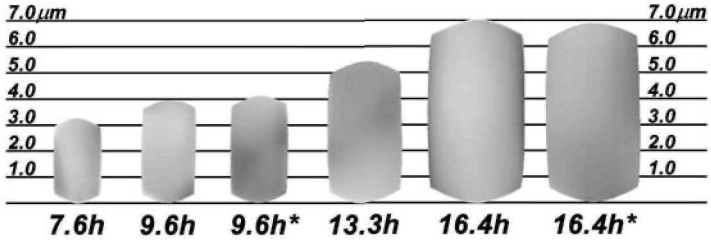

Fig. 4. Mean sample crystal sizes estimated from scanning electron micrographs. Asterisks denote samples removed after periods of disconnected nutrient feed.

Nutrient feed rates were calculated from Eq. (1) with further modification to correct for the finite concentrations of silica in the exit stream. Symbols are defined as follows: x is the [001] crystal length and A is the total surface area of the crystal population, both at time t, u is the mass feed rate (e.g. mass SiO_2 / unit time) and k is a constant dependent on crystal geometry and density. A full derivation of the equation is given elsewhere [19].

$$\frac{dx}{dt} = k\frac{u}{A} \tag{1}$$

A simple computer program was used to calculate approximate values for A as the reaction progressed, from known seed crystal size and experimental mass balance data. The crystal growth rate was thus kept fairly constant at 0.4 μm h^{-1}, as shown in. Fig. 3. Fig. 4 further reveals pauses in growth each time the nutrient feed is switched off, as evidenced by height similarity between the asterisked crystals and their non-asterisked counterparts. This result is of great significance as it reveals that very little volume is added to the growing crystals in the latter stage of a typical zeolite batch synthesis, when supersaturation levels in the gel are very low.

Fig. 5 shows AFM deflection images of typical (010) crystal surfaces. The two images of crystals removed from the reactor after periods of gel depletion, (c) and (f), show multiply-nucleated, approximately circular terraces that get closer together towards the edge of the crystal, with inherent parabolic height cross-sections. The terraces are clearly randomly positioned however each terrace necessarily nucleates on one below with the effect of drawing the most recent nucleation points towards the centre of the crystal. Terrace heights are generally 1.0 ± 0.1 or 2.0 ± 0.1 nm corresponding to the height of one and two pentasil chains respectively. Double height terraces are a product of the random nature of terrace fronts and their ever diminishing separation towards the edge of the crystal. Detailed examination of the images reveals many instances of pairs of consecutive terraces merging to create double height steps. Essentially, these images correspond well with those of 15 μm crystals also recovered from depleted gels, published elsewhere [10]. Furthermore, in terms of the number of nucleations given the size of the crystal, these images are typical of all images of synthetic zeolites published to date [1-11]. This owes to the generally accepted practice of zeolite batch synthesis whereby crystals are recovered by filtration from depleted gels.

There is however, one small difference that provides a link to discussion of the other four images shown in Fig. 5. The difference, which may be seen in both images though it is marginally clearer in image (c), is speckling of the surface. Cross-sectional analysis of the speckled areas reveals the height of these small features to be identical to the height of the

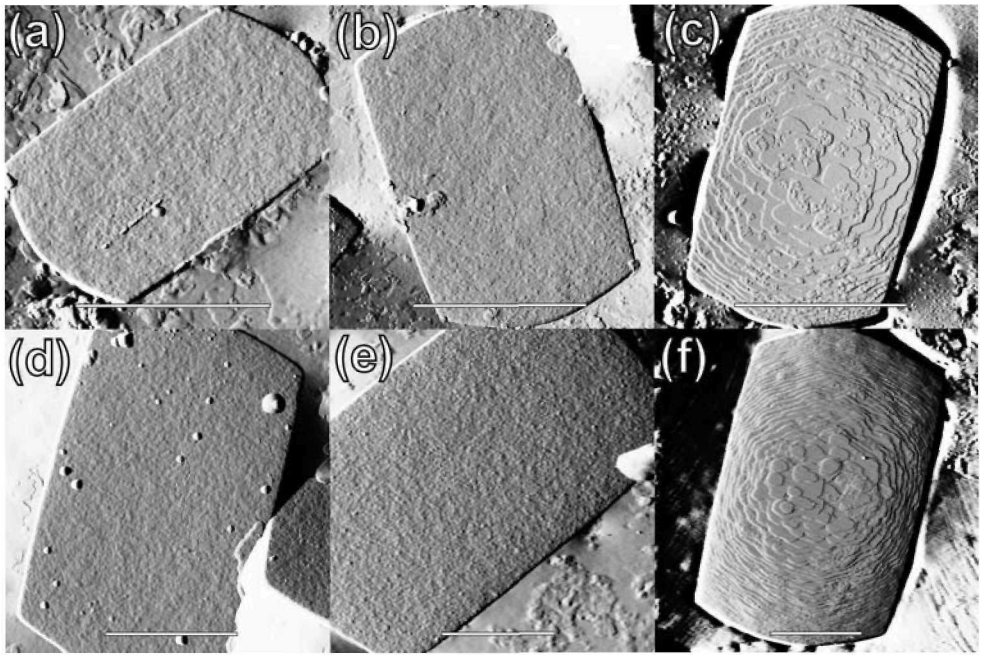

Fig. 5. AFM deflection images of (010) faces of the series of silicalite crystals synthesised in the constant nutrient feed reactor. Crystals shown in (a), (b), (d) and (e) were recovered from the reactor after 7.6, 9.6, 13.3 and 16.4 h of nutrient feed respectively. Crystals shown in (c) and (f) were recovered from the reactor after periods of cessation of nutrient feed and are denoted 9.6 h* and 16.4 h*. The scale bars represent 2 μm.

terraces strongly suggesting these small features are individual terrace nucleations and not amorphous surface debris.

Examination of images (a), (b), (d) and (e) of fig 5. reveals four similar surface topographies. In each case, the surface of the crystal is covered in a plethora of tiny, randomly shaped, though approximating to circular lumps, similar in nature to the speckles observed on the two previously discussed images. Once again, cross-sectional analysis reveals the height of these lumps to be 1 nm leading to the conclusion that each one is a separate terrace nucleation. Initial analysis indicates nucleation rates are between one and two orders of magnitude higher on these crystals, removed from nutrient fed gels, with elevated supersaturation rates.

Fig. 6 shows AFM deflection images of typical (100) crystal surfaces. These images mirror the phenomena observed on the (010) faces. Fig. 6 (c) and (f) show low levels of nucleation with the terraces present on the surface getting closer together as they approach the edge of the crystal. Figures 6 (a), (b), (d) and (e) show high levels of nucleation similar to those observed on the (010) face.

During zeolite synthesis, high levels of gel supersaturation cause high surface nucleation rates. These nuclei then spread rapidly and coalesce into completed layers. Terrace spreading rates are much faster than terrace nucleation rates and consequently it is surface nucleation rates that govern how quickly a crystal grows in a given direction. Towards the end of a synthesis, as the gel becomes depleted, crystal growth rates will decelerate. Being the

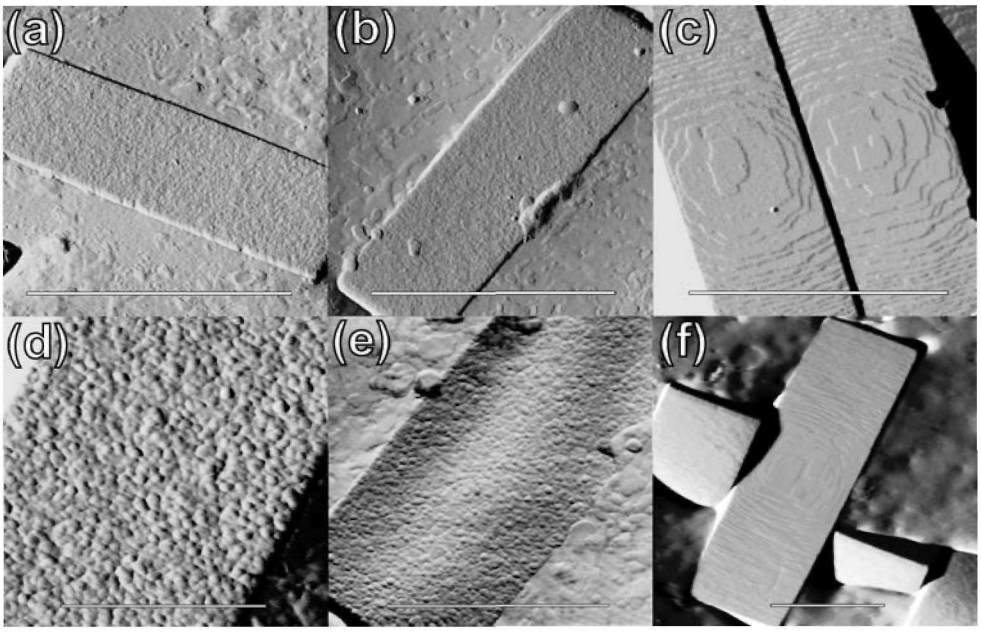

Fig. 6. AFM deflection images of (100) faces of the series of silicalite crystals synthesised in the constant nutrient feed reactor. Letter assignments correspond identically with those of Fig. 4. The scale bar in (d) represents 1 μm, all others represent 2 μm.

most energetically unfavourable, surface nucleation rates will tail off faster than terrace spreading rates, leading to the wealth of previously published images showing relatively low degrees of surface nucleation.

Of great interest is the ability of the crystal growth process to recover from periods of quenching caused by gel depletion. In this present study the nutrient feed was stopped three times. Crystal growth recovered unperturbed each time, with surface nucleation rates rapidly jumping back to their previous high levels. Each period of gel depletion was accompanied by a virtual halt in crystal growth, providing further evidence to link surface nucleation rates with crystal growth rates. It is thus appears possible to control the degree of surface nucleation, and hence crystal growth rate, by controlling gel supersaturation – even in the limiting case where growth is completely stopped and restarted. Thus the growth may be repeatedly switched on and off. One obvious goal of attempts to further understanding of crystal growth phenomena in microporous materials is to exert control over a crystal growth process. This has now been achieved.

The potential benefit of exerting control over such a fundamental aspect of zeolite crystal growth may best be highlighted by example. The porous titanosilicate material ETS-10 contains the narrowest known quantum wires, in the form of titanate chains that run through the material [21]. These titanate chains grow parallel to one another forming orthogonally stacked layers. There are two possible nucleation sites for any new chain. The inherent probability of chains in two separate, coalescing nuclei connecting correctly is only 50%. Failure to connect correctly results in chain discontinuity and the generation of a structural

line defect. An ability to reduce surface nucleation rates for ETS-10 synthesis should result in a decrease of such line defects and thus enhanced optoelectronic performance.

4. CONCLUSIONS

Design of a high pressure, semi-continuous flow reactor has enabled the controlled growth of a range of silicalite crystals. Analysis of the surface of these crystals by atomic force microscopy supports previously proposed mechanisms for zeolite crystal growth, based on imaging of batch synthesised crystals. However, it reveals dramatic differences in growth kinetics. Images of batch synthesised silicalite and other zeolites reveal a layer upon layer growth mechanism whereby the rate of terrace nucleation on a crystal face dictates the rate of growth of that face. Terrace spreading rates are significantly higher, with the area of any given terrace being proportional to the time for which it has been growing. This leads to commonly observed parabolic crystal faces. For batch synthesised crystals terrace nucleation rates are generally quite low – apparent mononucleation is sometimes observed. Images of silicalite crystals removed from highly supersaturated gels (designed to mimic those at intermediate stages of batch synthesis) reveal far higher surface nucleation rates (between one and two orders of magnitude higher). Cross-sectional analysis indicates that these surface nuclei are essentially identical to, but far smaller versions of, the terraces observed during the latter stages of growth.

When the nutrient supply to the reactor is cut, to mimic gel depletion during the final stage of batch growth, the rate of surface nucleation, and hence crystal growth, is curtailed. Being less energetically unfavourable, terrace spreading rates do not tail off as quickly, resulting in spreading and coalescence of the nuclei present on the surface, such that surface nucleation rates appear low. All previously published AFM images of zeolite crystals fall into this category. After reconnection of the nutrient supply evelated supersaturation levels cause a resumption of crystal growth and the zeolite surface is once again covered in nuclei. This process of switching growth on and off may be repeated. It is therefore possible to control surface nucleation rates by controlling gel supersaturation levels.

REFERENCES

[1] M.W. Anderson, J.R. Agger, J.T. Thornton and N. Forsyth, Angew. Chem., Int. Ed., 35 (1996) 1211.

[2] S. Sugiyama, S. Yamamoto, O. Matsuoka, T. Honda, H. Nozoye, S. Qiu, J. Yu and O. Terasaki, Surf. Sci., 377 (1997) 140.

[3] J.R. Agger, N. Pervaiz, A.K. Cheetham and M.W. Anderson, J. Am. Chem. Soc., 120 (1998) 10754.

[4] M.W. Anderson, J.R. Agger, N. Pervaiz, S.J. Weigel and A.K. Cheetham (M.M.J. Treacy, B.K. Marcus, M.E. Bisher and J.B. Higgins) Proc. 12th Int. Zeol. Conf., Baltimore, MRS, 1998, pp1487.

[5] S. Sugiyama, S. Yamamoto, O. Matsuoka, H. Nozoye, J. Yu, G. Zhu, S. Qiu and O. Terasaki, Microporous Mesoporous Mater., 28 (1999) 1.

[6] J. Warzywoda, M. Valcheva-Traykova, G.A. Rossetti Jr., N. Baç, R. Joesten, S.L. Suib and A. Sacco Jr., J. Crystal Growth, 220 (2000) 150.

[7] M.W. Anderson, N. Hanif, J.R. Agger, C.-Y.Chen and S.I. Zones, (A. Galerneau, F. Di Renzo, F. Fajula and J. Vedrine) Stud. Surf. Sci. Catal., Elsevier, Amsterdam, 2001,135, pp 141.

[8] J.R. Agger, N. Hanif and M.W. Anderson, Angew. Chem. Int. Ed., 40 (2001) 4065.

[9] S. Dumrul, S. Bazzana, J. Warzywoda, R.R. Biederman and A. Sacco Jr, Microporous Mesoporous Mater., 54 (2002) 79.
[10] J.R. Agger, N. Hanif, C.S. Cundy, A.P. Wade, S. Dennison, P.A. Rawlinson, and M.W. Anderson, J. Am. Chem. Soc., 125 (2003) 830.
[11] T. Wakihara, A. Sugiyama, T. Okubo, Microporous Mesoporous Mater. 70 (2004) 7.
[12] S. Bazzana, S. Dumrul, J. Warzywoda, L. Hsiao, L. Klass, M. Knapp, J.A. Rains, E.M. Stein, M.J. Sullivan, C.M. West, J.Y. Woo and A. Sacco Jr. (R. Aiello, G. Giordano, F. Testa) Proc. 2nd Int. FEZA Conf., Taormina, Elsevier, Ámsterdam, 2002, 142A, pp117.
[13] J. Warzywoda, B. Yilmaz, P.Q. Miraglia and A. Sacco Jr., Microporous Mesoporous Mater., 71 (2004) 177.
[14] B. Yilmaz, P.Q.Miraglia, J. Warzywoda and A. Sacco Jr., Microporous Mesoporous Mater., 71 (2004) 167.
[15] O. Terasaki, J. Electron Microsc., 43 (1994) 337.
[16] B. Slater, C.R.A. Catlow, Z. Liu, T. Ohsuna, O.Terasaki, and M.A. Camblor, Angew. Chem. Int. Ed., 41 (2002) 1235.
[17] T. Ohsuna, B. Slater, F.F. Gao, J.H. Yu, Y. Sakamoto, G.S. Zhu, O. Terasaki, D.E.W. Vaughan, S.L. Qiu and C.R.A. Catlow, Chem. Eur. J., 10 (2004) 5031.
[18] S.P. Zhdanov, ACS Adv. Chem. Ser. 101 (1971) 20.
[19] C.S. Cundy, M.S. Henty and R.J. Plaisted, Zeolites, 15 (1995) 353.
[20] C.S. Cundy, M.S. Henty and R.J. Plaisted, Zeolites, 15 (1995) 343.
[21] A. Damin, F.X. Llabre´s i Xamena, C. Lamberti, B. Civalleri,C.M. Zicovich-Wilson, and A. Zecchina, J. Phys. Chem. B, 108 (2004) 1328.

Studies in Surface Science and Catalysis, volume 158
J. Čejka, N. Žilková and P. Nachtigall (Editors)

Design of visible light sensitive (Cr,Ti)-containing mesoporous silica photocatalyst using a photo-assisted deposition (PAD) method

H. Yamashita[a]*, O. Chiyoda[a], Y. Masui[a], S. Ohshiro[a], K. Kida[b] and M. Anpo[b]

[a]*Department of Materials Science and Processing, Graduate School of Engineering, Osaka University, 2-1 Yamada-oka, Suita, Osaka 565-0871, Japan.
Tel&Fax: +81-6-6879-7457 E-mail: yamashita@mat.eng.osaka-u.ac.jp

[b] Department of Applied Chemistry, Graduate School of Engineering, Osaka Prefecture University, 1-1 Gakuen-cho, Sakai, Osaka 599-8531, Japan

It is vital to develop a visible light sensitive photocatalyst. In this study, (Cr,Ti)-binary oxide containing mesoporous silica (Cr/Ti-HMS) photocatalyst was prepared by an application of a photo-assisted deposition (PAD) technique and characterized by XAFS and photoluminescence studies. Using the PAD method, the tetrahedrally coordinated Cr-oxide moieties can be anchored on Ti-HMS forming the direct interaction between Cr-oxide and Ti-oxide moieties. The Cr/Ti-HMS exhibited the high efficiency and selectivity in the photoepoxidation of propene with O_2 under visible light irradiation. The charge transfer excited state of the Cr-oxide moieties anchored on Ti-oxide moieties play a significant role in photocatalytic reactions under visible light irradiation.

1. INTRODUCTION

The unique and fascinating properties of zeolites and mesoporous silica involving transition metals within their cavities and framework have opened new possibilities for many application areas not only in catalysis but also for various photochemical processes [1-5]. The transition metal ions in these catalysts are considered to be highly dispersed at the atomic level and also to be well-defined catalysts which exist in the specific structure of the zeolite and mesoporous silica framework. Especially the titanium oxide species prepared within the frameworks of mesoporous silica have revealed a unique local structure as well as a high selectivity in various catalytic reactions. These Ti-containing mesoporous silica can also exhibit efficient photocatalytic reactivity and high selectivity for NO decomposition [6], CO_2 reduction with H_2O [7-9], and partial oxidation of alkenes and alkanes [10]. However, these Ti-contaning catalysts can operate as the photocatalysts only under UV-light irradiation. Recently, we have found that Cr-containing mesoporous silica can demonstrate the

photocatalytic reactivity even under visible light irradiation [11,12], while the selectivities were not sufficient. To establish the clean photocatalysis system it is vital to develop the photocatalysts which can operate efficiently under visible light irradiation with high selectivity [5,13,14].

In the present study, the (Cr,Ti)-binary oxide containing mesoporous silica photocatalyst was prepared by the application of a photo-assisted deposition (PAD) technique which can realize the direct interaction between Cr-oxide and Ti-oxide moieties. The photocatalytic reactivity of (Cr,Ti)-containing mesoporous silica under visible light irradiation for the epoxidation of propene with O_2 has been investigated.

2. EXPERIMENTAL

2.1. Preparation of catalysts

Ti and Cr containing mesoporous silica catalysts, Ti-HMS (Si/Ti=50) and Cr-HMS (Si/Cr=50), were synthesized using tetraethylorthosilicate, titaniumisopropoxide and $Cr(NO_3)$ as the starting materials and dodecylamine as template [15]. To remove organic template molecules, the sample were calcined under a flow of dry air at 823 K for 6 hours. (Cr,Ti)-binary oxide containing mesoporous silica, Cr/Ti-HMS, was prepared using the PAD method: Cr-oxide was deposited on Ti-HMS from aqueous solution of $Cr(NO_3)$ under UV light irradiation using a high-pressure Hg lamp at 295 K. The samples were dried at 378 K and calcined under a flow of dry air at 823 K for 6 hours.

2.2. Photocatalytic reaction under visible light irradiation

The photocatalytic oxidation of propene (16 μmol) with O_2 (32 μmol) under visible light and UV light irradiation ($\lambda > 450$ nm, 270 nm) was carried out with the catalysts (50 mg) in a quartz cell with a flat bottom (88 ml) connected to a vacuum system (10^{-4} range) using a high-pressure Hg lamp through a UV cut filter at 295 K [10]. Prior to the photoreactions and spectroscopic measurements, the catalysts were degassed at 725 K, heated in O_2 at 725 K for 2 hours and finally evacuated at 473 K for 2 hours. The products collected in the gas phase and after heating of catalysts at 573 K were analyzed by g.c.

2.3. Characterization

The diffuse reflectance absorption spectra were recorded with a Shimadzu UV-2200A spectrometer at 295 K. The photoluminescence spectra were measured at 77 K using a Shimadzu RF-5000 spectrophotofluorometer. The X-ray absorption fine structure (XAFS) spectra, X-ray absorption near edge structure (XANES) and extended X-ray absorption fine structure (EXAFS), were measured at the BL-9A facility [16] of the Photon Factory at the National Laboratory for High-Energy Physics, Tsukuba. A Si(111) double

crystal was used to monochromatize the X-rays from the 2.5 GeV electron storage ring. The Ti K-edge and Cr K-edge absorption spectra were recorded in the fluorescence mode at 295 K. The normalized spectra were obtained by a procedure described in previous literature [17] and Fourier transformation was performed on k^3-weighted EXAFS oscillations in the range of 3-10 $Å^{-1}$.

3. RESULTS AND DISCUSSION

3.1. Characterization

Fig. 1 shows the diffuse reflectance UV-VIS absorption spectra of original Ti-HMS and Cr/Ti-HMS prepared by the PAD method. Ti-HMS exhibit absorption band in the wavelength regions of 220-260 nm, shifting into the shorter wavelength regions as compared to the bulk TiO_2 catalyst. This absorption band is attributed to the LMCT (ligand-to-metal charge transfer) band of the highly dispersed Ti-oxide moieties having a tetrahedral coordination [18,19]. As shown in Fig. 1, Cr/Ti-HMS can absorb visible light in the range of 400-600 nm, while Ti-HMS absorbs only UV light shorter than 300 nm. The absorption bands observed with Cr/Ti-HMS at around 270, 350, 450 nm can be assigned to the charge transfer from O^{2-} to Cr^{6+} of the tetrahedrally coordinated Cr-oxide moieties [5,11,12]. The absorption bands assigned to the absorption of the dichromate of Cr_2O_3 cluster cannot be observed above 550 nm [12], indicating that tetrahedrally coordinated Cr-oxide moieties exist in the isolated state on Cr/Ti-HMS. The intensity of absorption band at around 220-260 nm assigned to the LMCT band of the tetrahedrally coordinated Ti-oxide moieties become weaker with Cr/Ti-HMS than that of Ti-HMS indicating that Cr-oxide was deposited on the Ti-oxide moieties by the PAD method.

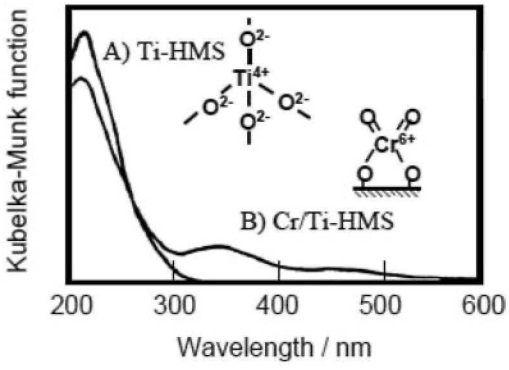

Fig. 1. UV-Vis spectra of (A) Ti-HMS and (B) Cr/Ti-HMS prepared by the PAD method.

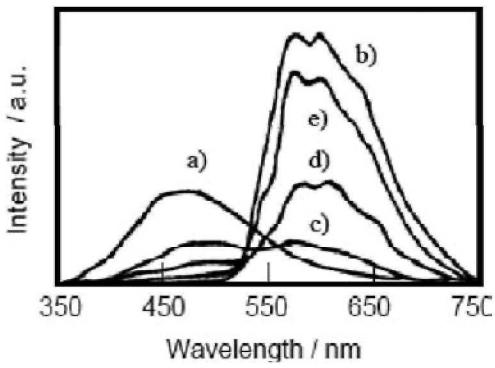

Fig. 2. Photoluminescence spectra of (a) Ti-HMS (b) Cr-HMS and (c-e) Cr/Ti-HMS prepared by the PAD method. Excited at (a) 260 nm, (b) 500 nm, (c) 260 nm, (d) 290 nm, (e) 500 nm.

Fig. 2 show the photoluminescence spectra observed on Ti-HMS, Cr-HMS and Cr/Ti-HMS. These photoluminescence bands can be assigned to the emission process from the charge transfer excited state of the tetrahedrally coordinated Cr-oxide and Ti-oxide moieties [18,19], as follows.

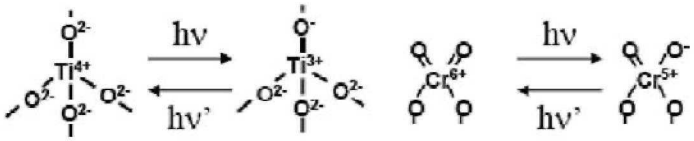

Cr/Ti-HMS exhibits photoluminescence band at around 640 nm under not only UV light irradiation (260, 290, 370 nm) but also visible light irradiation (415, 500 nm), while Ti-HMS exhibits photoluminescence band at 470 nm only under UV irradiation (260 nm). Even under visible light irradiation the photoluminescence bands on Cr/Ti-HMS were easily quenched by the addition of the reactant gas (propylene and oxygen). These results indicated that Cr/Ti-HMS can be excited not only under UV light irradiation but also under visible light irradiation, while Ti-HMS can be excited only under UV light irradiation.

Fig. 3 shows the XANES spectra of the original Cr-HMS and Ti-HMS catalysts and the Cr/Ti-HMS and Ti/Cr-HMS prepared by the PAD method. The XANES spectra of the Ti and Cr containing compounds at the Ti K-edge and Cr- K-edge show several well-defined preedge peaks that are related to the local structures surrounding the Ti atom and Cr atom, respectively. These relative intensities of the preedge peaks provide useful information on the coordination number surrounding the Ti atom and Cr atom [5,20,21]. As shown in Fig. 3, these catalysts exhibit a single preedge peak, while its intensity depends on the catalysts.

Because tetrahedrally coordinated Ti and Cr was found to exhibit an intense single preedge peak due to the lack of an inversion center in the regular tetrahedron structure [5,20,21], the observation of an intense single preedge peak indicates that the tetrahedrally coordinated Ti-oxide and Cr-oxide were incorporated within the framework of mesoporous silica in Ti-HMS and Cr-HMS, respectively. In the case of Cr-oxide moieties, two terminal Cr=O bonding is included in the tetrahedral coordination [5,11,12]. Although the Ti-HMS exhibits an intense preedge peak at Ti K-edge spectra indicating the presence of the tetrahedrally coordinated Ti-oxide moieties, the intensity observed with the Cr/Ti-HMS becomes much smaller. In the case of Cr K-edge, the intensity of preedge peak with Cr/Ti-HMS is as strong as that of Cr-HMS. These results indicate that the terahedrally coordinated Cr-oxide moieties having two terminal Cr=O bonds was deposited on Ti-oxide moieties making distorted Ti-oxide moieties by the direct interaction between Cr-oxide and Ti-oxide moieties. On the other hand, the intensity of preedge peaks with Ti/Cr-HMS prepared by the PAD method are very small indicating that tetrahedrally coordinated Ti-oxide and Cr-oxide are heavily distorted.

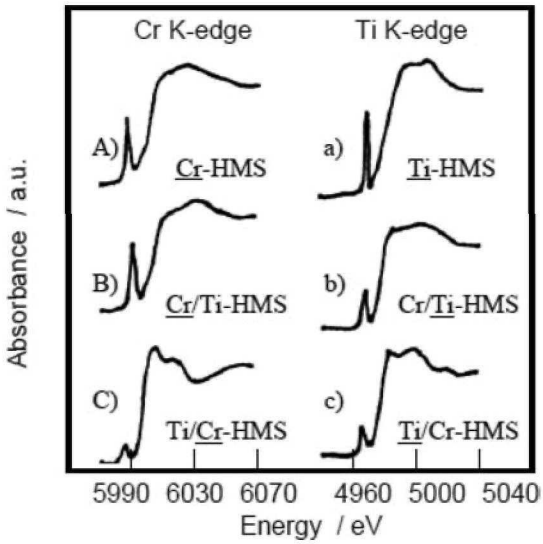

Fig. 3. XANES spectra at Cr K-edge (left) and Ti K-edge (right) of (A) Cr-HMS, (a) Ti-HMS, (B,b) Cr/Ti-HMS, (C,c) Ti/Cr-HMS.

These spectroscopic studies indicate that in the Cr/Ti-HMS prepared using the PAD method the tetra-Cr-oxide moieties was anchored on the tetra-Ti-oxide included in the frameworks of mesoporous silica having the direct interaction between the Cr-oxide and Ti-oxide moieties as shown in Scheme 1. In this scheme, the tetrahedrally coordinated Cr-oxide moieties are deposited on the Ti-oxide tetrahedral moieties excited under the UV light irradiation.

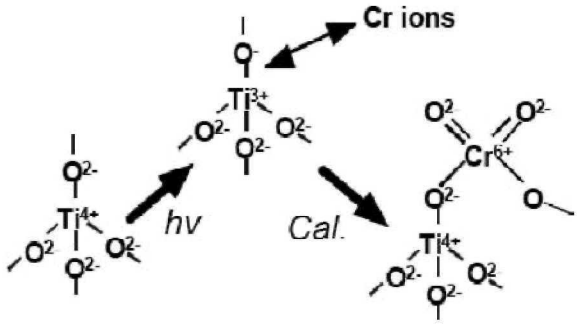

Scheme 1. Design of Cr, T binary oxide by the PAD method.

3.2. Photocatalytic reaction

Table 1 shows the results of the photocatalytic oxidation of propene with O_2 under UV light ($\lambda > 270$ nm) and visible light ($\lambda > 450$ nm) irradiation on Cr-containing silicalite (CrS-1), Cr-HMS and Ti-HMS. Under visible light irradiation ($\lambda > 450$ nm), the photoepoxidation of propene with O_2 to form propene oxide (PO) proceeded on the Cr-HMS, while CrS-1 exhibited very small reactivity. No reaction occurred on the Ti-HMS under visible light irradiation, although photoepoxidation occurred efficiently under UV light irradiation. These results suggested that it is vital application to design visible light sensitive catalyst by the combination of Ti-oxide and Cr-oxide moieties in HMS mesostructure.

Table 1
The products in the photocatalytic oxidation of propene with O_2 on Cr-oxide and Ti-oxide containing catalysts under light irradiation (λ>270 nm, λ>450 nm).

Catalyst	λ	Conv.	PO-yield	Selectivity / %						
	/nm	/%	/%	PO	AL	PA	AC	AA	CH	COx
CrS-1	450	3	0.1	4	45	2	14	8	2	25
Cr-HMS	450	10	1	12	18	11	10	24	4	21
Ti-HMS	250	7	1.5	22	14	12	26	5	11	10
Ti-HMS	450	0	-	-	-	-	-	-	-	-

PO: propylene oxide, AL: acrolein, PA: propanal, AC: acetone, AA: acetaldehyde, CH: hydrocarbon, COx: $CO + CO_2$

The results of Table 2 shows that the photoepoxidation of propene with O_2 proceeded efficiently and selectively under visible light ($\lambda > 450$ nm) irradiation on Cr/Ti-HMS prepared by the PAD method. The reactivity and selectivity to form epoxide on Cr/Ti-HMS were much higher than Cr-HMS and Cr/HMS catalysts, while Cr-HMS and Cr/HMS also exhibited reactivity for photoepoxidation even under visible light irradiation.

The charge transfer excited state of the tetrahedrally coordinated Cr-oxide moieties anchored on Ti-oxide moieties and the large pores of the mesoporous silica play a significant role in these highly selective and effective photocatalytic reactions. On the other hand, Ti/Cr-HMS hardly exhibited reactivity. The formation of distorted coordination of Cr-oxide and Ti-oxide moieties observed on Ti/Cr-HMS by the spectroscopic techniques is not suitable for the photocatalytic reaction.

Table 2
The products in the photocatalytic oxidation of propene with O_2 on Cr-oxide and Ti-oxide containing catalysts under visible light irradiation (λ>450 nm).

Catalyst	Conv.	PO-yield	Selectivity / %						
	/%	/%	PO	AL	PA	AC	AA	CH	COx
Cr-HMS	10	1	12	18	11	10	24	4	20
Cr/HMS	4	1	19	17	19	12	23	4	6
Cr/Ti-HMS	40	5	44	15	11	8	13	1	8
Ti/Cr-HMS	1	0	0	0	34	31	23	11	1

PO: propylene oxide, AL: acrolein, PA: propanal, AC: acetone, AA: acetaldehyde, CH: hydrocarbon, COx: CO + CO_2

4. CONCLUSION

Using the photo-assisted deposition method, the tetrahedral Cr-oxide moieties can be anchored on Ti-HMS forming the direct interaction between Cr-oxide and Ti-oxide moieties. It has been found that the Cr/Ti-HMS exhibited the higher efficiency and the higher selectivity in the photoepoxidation of propene with O_2 under visible light irradiation.

ACKNOWLEDGMENT

This work was supported by the Grant-in-Aid Scientific Research from the Ministry of Education, Science, Culture, and Sports of Japan (Grants 16656251). This work is also partly performed under the project of collaborative research at the Joining and Welding Research Institute (JWRI) of Osaka University with helpful advice from Prof. H. Fujii. The X-ray adsorption experiments were performed at the Photon Factory of KEK (2004G295) with helpful advice from Prof. M. Nomura.

REFERENCES

[1] B. Notari, Adv. Catal., 41 (1996) 253.
[2] A. Corma, Chem. Rev., 97 (1997) 2373.
[3] T. Tatsumi and N. Jappar, J. Phys. Chem., B, 102 (1998) 7126.
[4] M. Anpo and M. Che, Adv. Catal,. 44,119 (1999).

[5] H.Yamashita and M. Anpo, Current Opinion in Solid State & Maters. Sci., 7 (2004) 471.

[6] H. Yamashita, Y. Ichihashi, M. Anpo, C. Louis and M. Che, J. Phys. Chem., 100 (1996) 16041.

[7] M. Anpo, H. Yamashita, Y. Ichihashi, Y. Fujii and M. Honda, J. Phys. Chem. B, 101 (1997) 2632.

[8] K. Ikeue, H. Yamashita, M.Anpo and T. Takewaki, J. Phys. Chem. B, 105 (2001) 8350.

[9] H. Yamashita, K. Ikeue, T. Takewaki and M. Anpo, Top. Catal., 18 (2002) 95.

[10] H. Yamashita, K. Kida, K. Ikeue, Y. Kanazawa, K. Yoshizawa and M. Anpo, Stud. Surf. Sci. Catal., 146 (2003) 597.

[11] H. Yamashita, K. Yoshizawa, M. Ariyuki, S. Higashimoto, M. Che and M. Anpo, Chem. Commun., 435 (2001).

[12] H. Yamashita, M. Ariyuki, K. Yoshizawa, K. Kida, S. Ohshiro and M. Anpo, Res. Chem. Intermed., 30 (2004) 235.

[13] E.P. Reddy, L. Davydov and P. G. Smirniotis, J. Phys. Chem. B., 106 (2002) 3394.

[14] H. Yamashita and M. Anpo, Catal. Suv. Asia, 8 (2004) 35.

[15] W. Zhang, P. T. Tanev and T. J. Pinnavaia, J. Chem. Soc., Chem. Commun., (1996) 979.

[16] M. Nomura and A. Koyama, J. Synchrotron Rad., 6 (1999) 182.

[17] H. Yamashita, M. Matsuoka, K. Tsuji, Y. Shioya and M. Anpo., J. Phys. Chem., 100 (1996) 397.

[18] H. Yamashita, S. Kawasaki, Y. Ichihashi, M. Harada, M. Anpo, G. Stewart, M. A. Fox, C. Louis and M. Che, J. Phys. Chem. B, 102 (1998) 5870.

[19] H. Yamashita, M. Honda, M. Harada, Y. Ichihashi, M. Anpo and Y. Hatano, J. Phys. Chem. B, 102 (1998) 10707.

[20] J.M. Thomas and G. Sankar, Acc. Chem. Res., 34 (2001) 571.

[21] G. Sankar and J.M. Thomas, Top. Catal., 8 (1999) 81.

Studies in Surface Science and Catalysis, volume 158
J. Čejka, N. Žilková and P. Nachtigall (Editors)

1-Benzyl-1-methyl-hexamethylenammonium and some of its fluorine-containing derivatives as structure directing agent for the synthesis of all-silica zeolites

M. Arranz[a], J. Pérez-Pariente[a], T. Blasco[b]

[a]Instituto de Catálisis y Petroleoquímica. C/ Marie Curie Campus Cantoblanco. 28049 Cantoblanco. Madrid. Spain. E-mail; jperez@icp.csic.es.

[b]Instituto de Tecnología Química, UPV – CSIC. Avda. de los Naranjos s/n. 46022 Valencia. Spain.

The 1-benzyl-1-methyl-hexamethylenammonium (BMHM) cation under the appropriate synthesis conditions is a good structure directing agent (SDA) for the synthesis of pure silica zeolite beta in fluoride media. The chemical properties of this cation change with the replacement of a fluorine atom by a hydrogen atom in the aromatic ring and the nature and morphology of the crystal phases thus obtained are affected. The 1-orthofluorobenzyl-1-methyl-hexamethylenammonium allows the crystallization of all-silica beta zeolite but the morphology of crystals is very different from that of beta obtained with the all-hydrogen counterpart. The meta-F derivative leads to a mixture of three phases, Beta, nonasil (NON) and a characteristic unidentified phase, whereas by using the para-F cation only nonasil is obtained.

1. INTRODUCTION

Tailored zeolite synthesis which would make feasible the design of specific microporous topologies for specific applications is a much wanted objective in zeolite science. This is due to the fact that the macroscopic properties of zeolites materials are narrowly tied to the microscopic topology of ordered pores. Nevertheless, nowadays the crystallisation mechanism is insufficiently understood for this purpose. Commonly, searching for new structures and different chemical compositions is carried out by using a wide variety of synthesis conditions and different structure-directing agents (SDA).

The SDA establish no-bonding interactions with the zeolite and with inorganic species present in the gel [1, 2], the nature and strength of which depends on the chemical properties of the SDA. Hereby it would be possible to change these interactions by modifying the chemical properties of the organic species acting as SDA. A way to explore the effect of modifying the organic-inorganic interactions is provided by the use of fluorinated compounds, which allow to change the physicochemical properties of the SDA without changing its geometry and size [3, 4]. We have reported a first study of this type by using dibenzyldimethylammonium cation and its fluorinated derivatives [5].

In this work a new type of SDA, the 1-benzyl-1-methyl-hexamethylenammonium (BMHM) cation and its fluorinated derivatives have been used for the synthesis of all-silica zeolite materials in fluoride media. This study shows that fluorine-containing organic

compounds can be considered as a new family of SDA which can help in the search of new zeolite topologies or improve the synthesis of known phases.

2. EXPERIMENTAL

Table 1
Synthesis conditions and phases obtained; FX: unidentified phase.

SDA	Exp.	T	SDAOH	HF	SiO_2	H_2O	Result*
BMHM	H-1-A	150	0.53(+0.26**)	0.54	1	4.62	Beta NON
M-FBMHM	M-1-A	150					Beta NON FX
M-FBMHM	M-1-B	135	0.54(+0.26)	0.54	1	4.91	Beta NON FX
M-FBMHM	M-1'-A	150	0.80	0.80	1	4.90	Beta NON FX
BMHM	H-2-A	150	0.54	0.54	1	4.60	Beta
BMHM	H-2-B	140					Beta
O-FBMHM	O-2-A	150	0.54	0.54	1	4.61	Beta
M-FBMHM	M-2-A	150	0.54	0.54	1	4.68	Beta NON FX
P-FBMHM	P-2-A	150	0.54	0.54	1	4.55	NON
BMHM	H-3-A	150	0.44	0.44	1	4.72	Beta
BMHM	H-3-B	135					Beta
BMHM	H-4-A	150	0.44	0.44	1	7.93	Beta↓
BMHM	H-4-B	135					Beta
O-FBMHM	O-4-B	135	0.44	0.44	1	7.92	Beta↓
M-FBMHM***	M-5-A	150	0.54	0.54	1	7.93	NON

* All samples obtained at 30d, except, H-1-A, P-2-A, M-5-A at 36d, and H-4-A, H-4-B, O-4-B at 63d.
** Iodide is added to increase the SDA content without increasing fluoride content.
***Contains hexamethylenimine as impurity, because ternary amine not was distilled

Tertiary amines, 1-benzyl-hexamethylemimine (BHM) and their fluorine-containing derivatives, ortho-, meta- and para-fluorobenzyl-hexamethylenimine (o-FBHM, m-FBHM, p-FBHM respectively) were synthesised by the reaction of hexamethylenimine (50% exc. Sigma-Aldrich) with the corresponding benzyl chloride or 2-fluoro, 3-fluoro, or 4-fluorobenzyl chloride (Avocado) in ethanol at 90 °C for 2 d, in presence of K_2CO_3. The reaction mixture was filtered and washed three times with ethanol, the solvent was removed under vacuum at 60 °C, and the resulting solution was purified by vacuum distillation. BHM and FBHM were distilled at 17 mmHg and 135-140°C (~90% yield). The purity of these amines was assessed by thin layer chromatography (hexane/ ethyl acetate as solvent) and chemical analysis.

The synthesis of quaternary ammonium cations was carried out by methylation of the tertiary amines obtained previously with a solution of CH_3I (50% exc., Fluka) in ethanol. This solution was stirred for 5d at room temperature, the ethanol was removed under vacuum at 60°C, and the solid products obtained, iodide of 1-benzyl-1-methyl-hexamethylenammonium (BMHMI) (~70% yield) and iodide of 1-fluorobenzyl-1-methyl-hexamethylenammonium (o-FBMHMI, m-FBMHMI, p-FBMHMI) (~ 90% yield) were washed with ethyl ether and characterized by ^{13}C NMR and chemical analysis. These iodide salts were converted into the corresponding hydroxide, BMHMOH or FBMHMOH, by ion-exchange with an Amberlyst IRN78 resin (exc. cap: 4 me/g, Supelco). The BMHMOH and FBMHMOH solutions were titrated with HCl 1N (Panreac) and phenolphthalein (Aldrich).
Finally, the synthesis gel was prepared by adding tetraethylorthosilicate (TEOS, Merck) on a BMHMOH or FBMHMOH solution under continuous stirring. Once the ethanol is evaporated, HF (48 wt%, Panreac) is added drop by drop. The resulting thick gel is then introduced into 20ml Teflon-lined stainless steel autoclaves which were heated statically at 135-150°C for selected periods of time. The obtained solid product was filtered, washed and dried overnight at 70°C. Chemical composition and temperature of different synthesis gels are given in table 1. Where in the nomenclature employed the first letter correspond to the cation, H of hydrogenated or fluorinated in O, ortho-, M, meta- or P, para- position, number correspond the gel composition, and last letter differences the temperature of synthesis.

The solid products were characterized by XRD, TGA, SEM, MAS-NMR.

3. RESULTS AND DISCUSSION

3.1. X-Ray powder diffraction

The behavior of BMHM as SDA is deeply influenced by different synthesis conditions and the presence and position of fluorine in the cation. Fluoride has been used as mineralizing agent for its advantages in the synthesis of pure silica zeolites. Zeolite beta was obtained with BMHM cation at low H_2O/SiO_2 ratio and medium and low SDA content, Fig.1, experiment H-2-A. If the concentration of SDA increases, then nonasil and beta co-crystallise. The o-FBMHM cation also leads to beta zeolite. The m-FBMHM cation leads to the simultaneous crystallisation of Beta and nonasil, either at high or intermediate cation concentration, whereas at long crystallisation time a unidentified phase is also detected, which is characterised by an intense low-angle XRD reflection at $2\theta \sim 6.8$, Fig. 1. Only nonasil is also obtained with m-FBMHM cation at high water content, experiment M-5-A. Finally, the use of p-FBMHM in the conditions of experiment H-2-A only leads to nonasil.

If the SDA content is decreased, BMHM also leads to zeolite beta, experiment H-3-A. This zeolite is also obtained from more diluted gels, experiment H-4-B, and in these conditions the ortho-fluorinated cation also crystallises beta, but a lower rate, experiment O-4-B.

It can be concluded that the BMHM cation is an adequate SDA for the synthesis of all-silica zeolite beta, while the formation of nonasil seems to be linked either to a low crystallisation rate of beta, or to a high concentration of this cation in the gel. In both cases, a higher concentration of the BMHM favours the competitive phenomenon, Hoffmann degradation [6] of N-benzyl bond of the quaternary cation, which takes place at long crystallisation time. In this case, the resulting methyl-hexamethylenimine may act as a good SDA for nonasil phase [7].

The presence of fluorine in the BMHM molecule strongly affects the ability of this cation for the nucleation of zeolite beta, and a new not yet identified phase appears if the meta-F derivative is used.

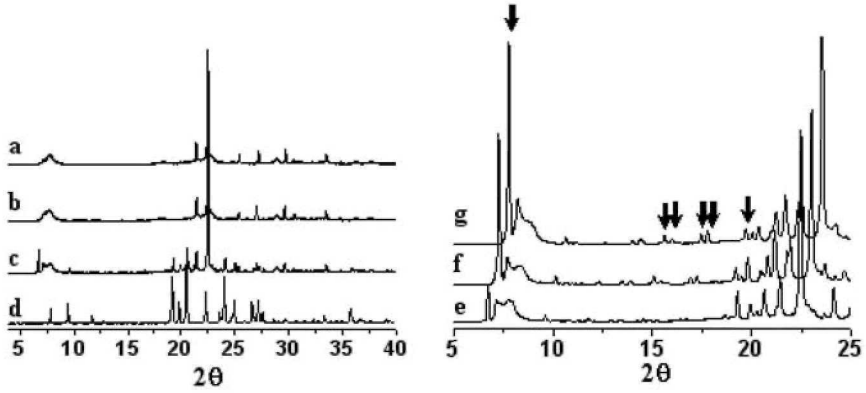

Fig. 1. XRD patterns of samples a) H-2-A, b) O-2-A, c) M-2-A, d) P-2-A, Enlargement of the diffractogram region 2θ=5°-25°: e) of M-2-A, f) of M-1-B, g) of M-1'-A. The arrows show the peaks corresponding to unidentified phase.

3.2. Scanning electron microscopy

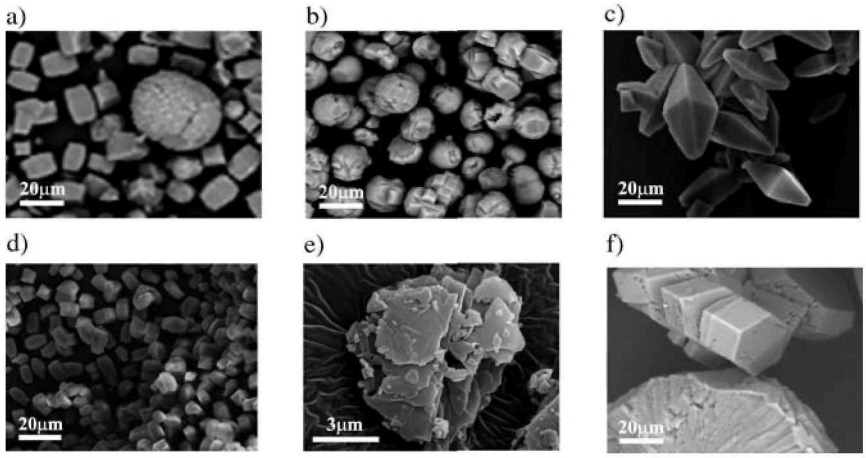

Fig. 2. SEM of samples synthesised with BMHM a) beta and nonasil H-1-A, b) beta H-2-A, c) beta H-4-B, d) beta crystals O-2-A, e) M-1-A, unidentified phase, f) M-5-A, nonasil phases, spherical aggregates and crystal with hexagonal faces.

The crystal morphology of beta is influenced by the SDA content in the synthesis gel. The most concentrated gel gives isolated crystal of nearly prismatic shape, H-1-A (average length 18μm, aspect ratio 1.4), Fig 2. Diluted gel leads to longer isolated crystal of well-defined sharp-pointed truncated bipyramid typical of beta, H-4-B (average length 32μm, aspect ratio 2.6). Therefore the growth rate of beta along a, b and c axes varies differently according to the crystallisation conditions. In addition, there is a noticeable change in the

morphology of beta crystals due to the presence of fluorine, since H-2-A shows unusual spherical aggregates whereas O-2-A shows isolated crystals.

Nonasil appears both as spherical aggregates and as isolated crystals with hexagonal morphology, and lamellar aggregates belonging to the unidentified phase are observed.

3.3. Thermogravimetry and chemical analyses

Beta phases obtained with BMHM or o-FBMHM show about 21% weight loss between 200-475°C, Fig. 2a, which agree with the organic content obtained by chemical analyses. The C/N ratio (13.7 for H-2-A and 14.2 for O-2-A) suggests that the both cations, BMHM and o-FBMHM, around four per unit cell are intact within the zeolite channels.

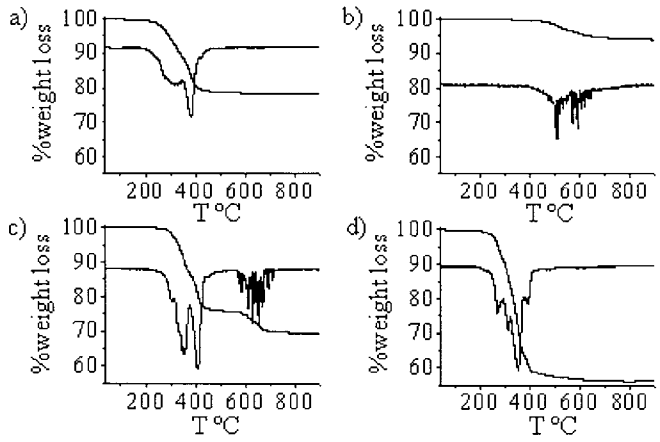

Fig. 3. Thermogravimetry analyses of a) beta H-3-A b) nonasil P-2-A, c) beta, nonasil and unidentified phase M-2-A, and d) beta, nonasil and unidentified phase M-1-A, samples.

Nonasil phase, Fig. 3b, shows a Thermogravimetry pattern with a weight loss between 400-674°C, and at 900°C not all the organic has been removed, since chemical analyses shows an organic content (~10%) higher than the weight loss up to 900°C. In addition, the C/N ratio (7.3 for P-2-A, 7.7 for M-5-A) indicates that cation fragments such as methyl-hexamethylenimine, might occupy the $[5^8\ 6^{12}]$ nonasil cages. Indeed, the carbon content (4 molec. /u.c.) suggests a full occupancy of these cavities by the amine.

Thermogravimetry of the samples that contain beta, nonasil and the unidentified samples, Fig. 3c and 3d, are very interesting because the weight loss occur in the same T range of beta and nonasil, but the total weight loss is higher. This suggests a high content of organic material occluded into the unidentified phase. In addition, the C/N ratio (12.3 for M-2-A, 12.5 for M-1-A, 13.4 for M-1-B, 12.1 for M-1'-A) indicates that most of the occluded organic material would correspond to the unaltered cation. The similarity of the TG patterns of beta and the sample containing the unidentified phase suggests that these cations would occupy large channels or voids also in the latter.

3.4. MAS NMR

3.4.1. ^{13}C NMR

$^{1}H/^{13}C$ CP MAS NMR spectra confirm the integrity of the cations incorporated into the zeolite cavities. The spectrum of sample H-3-B is similar to that of the BMHM iodide salt. They consist of signals of methylene groups in the 20-66 ppm range, methyl group at 50 ppm, and of aromatic carbons between 125-135ppm [8]. The spectra of sample O-2-A and the iodide salt of o-FBMHM, shown in Fig. 4i and ii, give an additional peak at 160 ppm due to the carbon bonded to F. This later signal is also present in the spectra of m-FBMHM iodide Fig. 4iii and samples M-1-A and M-2-A synthesised with this cation Fig. 4 iv and 4 v; but, in this case, the spectrum in the region corresponding to the aromatic ring is more complex than that of the iodide salt. The spectrum of M-5-A sample (NON) Fig. 4 vi confirms the presence of methyl-hexamethylenimine, in agreement with chemical analysis.

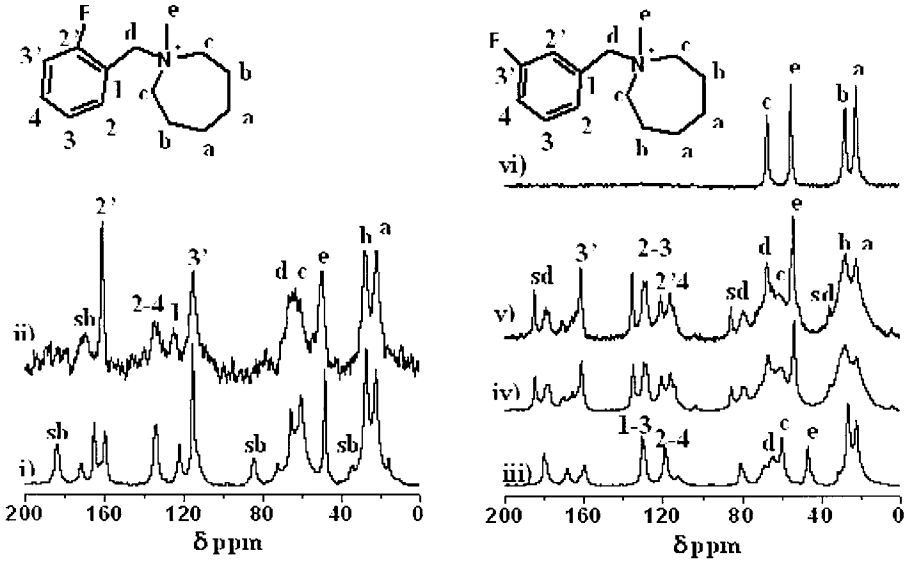

Fig. 4. $^{1}H/^{13}C$ CP MAS NMR spectra of, i) o-FBMHMI, ii) O-2-A, iii) m-FBMNMI, iv) M-1-A,v) M-2-A, and vi) M-5-A.

3.4.2. ^{19}F NMR

The ^{19}F MAS NMR spectrum of zeolite beta synthesised with BMHM, shown in Fig. 5a, gives three signals at -37, -59 and -70 ppm, of fluoride acting as "counterion" of the organic cation [9]. The peak at -37 ppm, characteristic of fluoride anions located at double four member ring cages (D4R) indicates the presence of the beta polymorph C[10]. The two other peaks are attributed to fluoride anions within the $[4^35^4]$ cages of the BEA structure. The spectrum of the beta sample O-2-A, synthesised with o-FBMHM, shows signals at -113 ppm, of fluorine in aromatic ring [11], -37, and –70. The absence of the resonance at -59 ppm suggests that the presence of fluorine in the organic cation can exercise an influence in the distribution of fluoride among the different zeolite cages. . The ^{19}F spectrum of sample M-5-A with the nonasil structure shows two signals at c.a. -80 ppm, Fig. 5i, which are assigned to fluorine atoms placed within the $[4^15^46^2]$ cages. The spectra of samples M-1'-A and M-1-A, mixture of beta, nonasil and unidentified phase, give various signals between –30 ppm and -

90 ppm of fluoride anions in different cages, and an intense signal at -114ppm of fluorine in aromatic ring Fig.5iv and 5v. But the most noticeable feature is the presence of a very intense resonance signal at -119 ppm, most probably due to F^- anions compensating the organic cations [12]. However, this signal might arise as well from F atoms of the ring interacting with the framework, since the incorporation of the cation inside the zeolite cavities modifies the chemical shift of the aromatic carbon atoms.

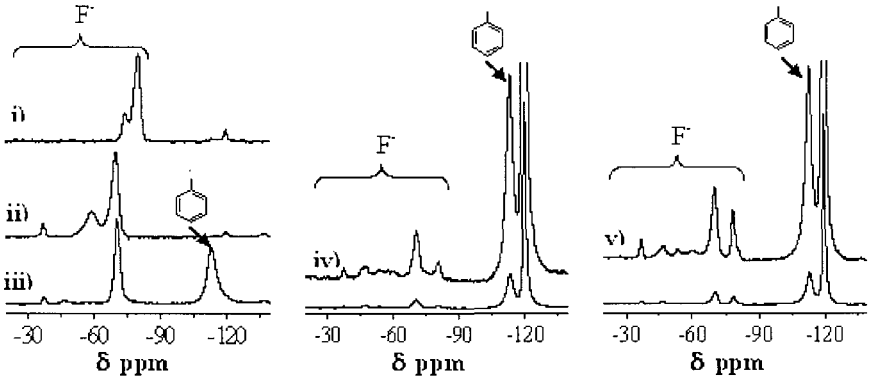

Fig. 5. ^{19}F MAS NMR spectra of samples: i) Nonasil M-5-A, ii) beta H-2-A, iii) beta O-2-A, iv) beta, nonasil, unidentified phase M-1'A at 30d, enlargement on top, v) beta, nonasil, unidentified phase M-1-A, enlargement on top.

3.4.3. ^{29}Si NMR

Fig. 6 shows the ^{29}Si MAS NMR spectra of pure beta (sample H-3-B, Fig. 6 i) and nonasil, sample M-5-A, Fig. 6 iv) zeolites, as well as those of mixed phases (samples M-2-A and M-1-A in Fig. 6 ii and iii, respectively), The spectra of the samples containing a mixture of beta, nonasil and unknown phase can be essentially accounted for by the combination of beta and nonasil spectra. Therefore, no characteristic signal that could eventually be assigned to the unknown phase can be clearly distinguished in the spectra. We must note the presence of signals at –145.3 and –147.8 ppm in the spectrum of nonasil, which can be assigned to five-fold coordinated Si atoms [13].

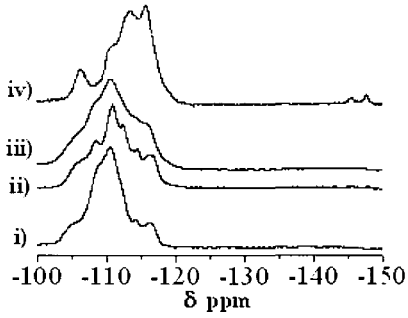

Fig. 6. ^{29}Si MAS NMR as prepared zeolites, i) beta sample H-3-B, ii) beta, nonasil, unidentified phase M-2-A, iii) beta, nonasil, unidentified phase M-1-A iv) nonasil M-5-A.

4. CONCLUSIONS

The BMHM cation is an efficient structure directing agent for the synthesis of pure silica beta zeolite, but a narrow set of conditions are required to avoid degradation of the cation and the crystallisation of nonasil. The behaviour of BMHM as structure directing agent is affected by the substitution of only one hydrogen atom by fluorine in the aromatic ring, and this effect also depend upon the fluorine position in the ring. Changes of crystal size and morphology and the crystallisation of a unidentified open phase occur by using fluorinated BHMH cations.

All-hydrogenated as well as fluorine-containing derivatives are found unbroken within the zeolite cavities, and the C-F bond stability under the synthesis conditions used in this work has been evidenced by ^{13}C and ^{19}F MAS NMR

Therefore, the change in the chemical character of the SDA brought about by the replacement of H by F atoms, which implies a change in the interactions between organic species and the zeolite framework, is a new factor that it is necessary bear in mind in zeolite synthesis.

ACKNOWLEDGEMENTS

Financial support of CICYT (project MAT 2003-07769-C02-02) is acknowledged. M. Arranz acknowledges the Spanish Ministry of Science and Technology for a PhD. grant.

REFERENCES

[1] A. V. Goretsky, L. W. Beck, S. I. Zones, M. E. Davis, Microporous Mesoporous Mater., 28 (1999) 387.
[2] S. L. Burkett and M. E. Davis, Chem. Mater., 7 (1995) 1453.
[3] R. N. Haszeldin and, A.G. Sharpe, Fluorine and its compounds, Methuen John Wiley, London, (1951).
[4] M. Hudlicky, Chemistry of organic fluorine compounds: a laboratory manual with comprehensive literature coverage, Ellis Horwood cor., New York, (1992).
[5] J. Pérez-Pariente, L. Gómez-Hortigüela, M. Arranz, Chem. Mater., 16 (2004) 3209.
[6] K. P. C. Vollhardt, Neil E. Schore, Organic Chemistry, W. H. Freeman and company, New York, (2003).
[7] B. Marler, H. Gies, Zeolites, 15 (1995) 517.
[8] E. Pretsch, J. Seibl, W. Simon, T. Clerc, Tables of spectral data for structure determination of organic compound, Springer-Verlag, Berlin, (1989).
[9] M. A. Camblor, Philip A. Barrett, M. J. Díaz-Cabañas, L. A. Villaescusa, M. Puche, T. Boix, E. Pérez, H. Koller, Microporous Mesoporous Mater., 48 (2001) 11.
[10] J. M. Newsam, M. M. J. Treacy, W. T. Koetsier, C. B. Gruyter, Proc. R. Soc. London A., 420 (1988) 375.
[11] C. H. Dungan, J. R.Van Waser, Compilation of reported F19 NMR chemical shifts 1951, to Mid-1967, Wiley-Interscience, New York, (1970).
[12] L. Delmotte, M. Soulard, F. Guth, A. Seive, A. Lopez, J. L. Guth, Zeolites, 10 (1990) 778.
[13] H. Koller, A. Wölker, L. A. Villaescusa, M. J. Díaz-Cabañas, S. Valencia, M. A. Camblor, J. Am. Chem. Soc., 121 (1999)3368.

Studies in Surface Science and Catalysis, volume 158
J. Čejka, N. Žilková and P. Nachtigall (Editors)

Synthesis and characterization of novel zeolites MCM-58 and MCM-68

G. Košová

J. Heyrovský Institute of Physical Chemistry, Academy of Sciences of the Czech Republic, Dolejškova 3, CZ-182 23 Prague, Czech Republic

Synthesis and catalytic properties of zeolites MCM-58 and MCM-68 were investigated. The MCM-58 was synthesized using N-benzylquinuclidinium bromide (BQ) as a structure directing agent (SDA) in a wide range of initial ratios n_{Si}/n_{Al} = 20 - 40 and n_{Si}/n_{Fe} = 20 - 40. The MCM-68 was synthesized with N,N,N',N'-tetraethylbicyclo[2.2.2]oct-7-ene-2,3:5,6-dipyrrolidinium diiodide as a SDA in the range of initial n_{Si}/n_{Al} ratios from 9 to 20. The catalytic properties of zeolites were tested in the isopropylation of toluene. Relatively high amounts of n-propyltoluenes were observed over Al-MCM-58 and Al-MCM-68, however, Fe-MCM-58 possesses nearly 100 % selectivity to cymenes.

1. INTRODUCTION

The alkylation reactions are widely used in chemical industry for the production of important alkyl aromatic intermediates (ethylbenzene, *p*-ethyltoluene, *p*-xylene, cumene, cymene) [1-3]. Many industrial alkylation processes are still performed with classical catalysts (HF, solid phosphoric acid) showing drawbacks (handling, safety, corrosion and waste disposal). In order to avoid these problems many efforts have been devoted to search catalysts more selective, safe and environmentally friendly, regenerable, and reusable. These problems of classical catalysts can be avoided when zeolites are used as catalysts [4]. Zeolites constitute a very important group of inorganic microporous materials subservient to applications like adsorption, ion exchange and especially heterogeneous catalysis [5,6]. The catalytic activity and selectivity of zeolites is attributed to the large internal surface with active sites that are accessible through uniformly sized pores. Acid strength is one of the most important factors for controlling reactivity and selectivity of zeolite catalysts. Properties like geometry, chemical composition and aluminum distribution can be correlated with acid strength of zeolites [7]. Thus, reactions are classified from the point of view of acid strength needed (alkylation requires sites of medium-strong acidity). To optimize the acid strength and geometry of zeolites strong effort is devoted to the synthesis of new structural types of zeolites with tailored pores systems. Accurate preparation of synthesis using novel types of SDA resulted recently in a successful synthesis of new types of zeolites (ITQ-15 [8] with 14- and 12-membered rings, SSZ-58 [9] zeolite with previously unseen double 5-ring subunits, and micro/mesoporous composite molecular sieves [10].

In this contribution, synthesis and characterization of zeolites MCM-58 [11] as an Al- and Fe-silicates (IFR) and aluminosilicate MCM-68 [12] was carried out. The MCM-58 topology is characterized by an undulating, one-dimensional channel system with 12- membered rings. MCM-68 has a unique crystal structure, which contains one channel system, in which each

channel is defined by a 12-membered ring and two further channels, in each of which the channel is defined by a 10-membered ring. MCM-58 and MCM-68 were characterized using XRD, XRF, FTIR and SEM. Catalytic properties of these zeolites were tested in the alkylation of toluene with isopropylalcohol. The desired product *p*-cymene is the starting material for production of some fungicides, pesticides, and flavors.

2. EXPERIMENTAL

2.1. Catalysts preparation

Aluminosilicate and ferrisilicate MCM-58 was synthesized using N-benzyl-1,4-diazabicyclo[2.2.2] octane cation (BQ) as a SDA. The BQ was prepared by refluxing an equimolar mixture of benzyl bromide (Fluka) and quinuclidine (Fluka) in ethanolic solution for 24 h. Crystalline template was recovered after cooling the reaction mixture in an ice bath. Chemical composition and structure of the template was confirmed by elementary analysis and NMR. Al-MCM–58 was synthesized with n_{Si}/n_{Al} ratios in the initial synthesis gel ranging from 20 to 40 and n_{Si}/n_{Fe} ratio ranging from 20 to 40. The molar composition of initial synthesis gel was as follow: (0.016–0.025) Al_2O_3: SiO_2: 38 H_2O: 0.30 K_2O: 0.10 BQ for Al–MCM–58 and (0.0125–0.025) Fe_2O_3: SiO_2: 38 H_2O: 0.30 K_2O: 0.20 BQ for Fe–MCM–58. In a typical synthesis of Al–MCM–58, 3.69 g of $Al_2(SO_4)_3.18H_2O$ (Fluka) was dissolved in 88.00 g of distilled water. To this solution, 3.24 g of KOH (Lachema, CZ) and subsequently 4.02 g of BQ (as made) were added under stirring. Later on, 30.00 g of colloidal silica sol (30 wt. % SiO_2 in water, Ludox AS–30, Aldrich) was slowly blended with the reaction mixture under vigorous stirring, which was finally homogenized for 2 min. The resulting gel was loaded into 90 ml Teflon–lined stainless steel autoclaves. The synthesis was carried out under rotation at 170 °C for Al–MCM–58 and at 155 °C for Fe–MCM–58 for 4 to 9 days. For the synthesis of Fe–MCM–58, the aluminum source was replaced by $Fe(NO_3)_3.9H_2O$ (Fluka) and instead of Ludox AS–30, Levasil VP 4038 (30 % SiO_2 in water, Bayer AG) was used. After crystallization, the autoclaves were cooled down to the room temperature in cold water; the solid product was filtered, washed with distilled water, and dried at 80 °C overnight.

For the synthesis of aluminosilicate MCM-68 a novel polycyclic organic cation N,N,N',N'-tetraethylbicyclo[2.2.2]oct-7-ene-2,3:5,6-dipyrrolidinium diiodide was used as a SDA. The synthesis of SDA was performed as follow: to 70 % water solution of ethylamine was added under vigorous stirring bicyclo[2.2.2]oct-7-ene-2,3,5,6-tetracarboxylic-dianhydride. The resulting product N,N,N',N'-tetraethylbicyclo[2.2.2]oct-7-ene-2,3,5,6-diamide was reduced with $LiAlH_4$ in THF to form the amine N,N,N',N'-tetraethylbicyclo[2.2.2]oct-7-ene-2,3,5,6-dipyrrolidine. This amine was then alkylated with iodomethane to give the template N,N,N',N'-tetraethylbicyclo[2.2.2]oct-7-ene-2,3,5,6-dipyrrolidiniumdiiodide. Al-MCM-68 was synthesized in a range of initial n_{Si}/n_{Al} ratios in the gel from 9 to 20. The molar composition of reactants was: SiO_2 : 0.0278-0.0556 Al_2O_3 : 0.1 SDA : 0.375 KOH : 30 H_2O. In a typical synthesis 14 g of colloidal silica sol (30 wt. % SiO_2 in water, Ludox SM–30, Aldrich), and 22.1 g H_2O were mixed with 0.606 g of $Al(OH)_3$. To this solution 7.354 g KOH (20 wt. % solution) and then 3.912 g of SDA was added. The mixture was put in an autoclave and heated at 160 °C under static conditions for 13 days. The product was then filtered, washed with water and dried overnight at the ambient temperature.

To remove the template, all as–synthesized zeolites were heated up to 200 °C in a stream of nitrogen with a temperature ramp of 1 °C/min and kept at the same temperature for 4 h.

Thereafter, zeolites were heated to 540 °C with the same heating rate and kept for 2 h at this temperature. Finally, the material was calcined for 24 h in a stream of air at 540 °C.

The ammonium forms of both zeolites were prepared by four times repeated ion exchange of the zeolite in 0.5 *M* aqueous solution of ammonium nitrate at ambient temperature.

2.2. Characterization of catalysts

XRD patterns of synhesized and calcined zeolites were collected on a Bruker D8 X–ray powder diffractometer equipped with a graphite monochromator and positron sensitive detector (Avantage) using CuKα radiation in Bragg–Brentano geometry. The shape and size of zeolites crystals were determined by scanning electron microscopy (JEOL, JSM–03). X–ray fluorescence spectroscopy (Philips PW 1404) was employed to estimate the chemical composition of zeolites.

The concentrations of Broensted and Lewis acid sites were determined after adsorption of probe molecules, followed by FTIR spectroscopy using a Nicolet FTIR Protégé 460 spectrometer. D_3-acetonitrile was used for characterization of acid sites of alumosilicates (Al-MCM-58 and Al-MCM-68), while pyridine for Fe-MCM-58. For this purpose, the zeolite powders were pressed binder–free into self–supporting wafers with a density from 4.0 to 10.0 mg/cm^2. D_3–acetonitrile and pyridine were degassed by repeated freezing and thawing cycles before its use. Prior to the adsorption of probe molecules, the zeolites were activated "in–situ" by overnight evacuation at 500 °C. Adsorption of d_3-acetonitrile was carried out at laboratory temperature (25 °C) for 30 min, pyridine interacted with acid sites of Fe-MCM-58 at 170 °C for 30 min. The adsorption in both cases was followed by 20 min of desorption. All measured spectra were recalculated to a normalized wafer thickness of 10 mg/cm^2. For a quantitative characterization of Broensted acid sites (B), the C≡N–B vibration at about 2296 cm^{-1} was used with an extinction coefficient of $\varepsilon_B = 2.05 \pm 0.1$ cm/μmol^{-1}. For a quantitative evaluation of Lewis acid sites (L), the C≡N–L vibration at 2323 cm^{-1} was used with an extinction coefficient of $\varepsilon_L = 3.6 \pm 0.1$ cm/μmol^{-1}. From integral intensities of individual bands at 1545 cm^{-1} (Broensted sites) and at 1448 cm^{-1} (Lewis sites) and using extinction coefficients of $\varepsilon_L = 1.67 \pm 0.1$ and $\varepsilon_B = 2.22 \pm 0.1$ cm/μmol, respectively, concentrations of both types of acid sites were calculated according to ref. [13]. The infrared spectra of skeletal vibrations were recorded using KBr pellet technique [14].

Catalytic tests (isopropylation of toluene) were performed in a vapor phase continuous glass down flow microreactor at atmospheric pressure and *WHSV* = 10 h^{-1} based on toluene. Nitrogen was used as a carrier gas, toluene to isopropanol molar ratio was 9.6. Zeolites (0.4 g) in their granulated form were pretreated in an oxygen stream at 500 °C for 1 hour and then the reactor was cooled to a reaction temperature 250 °C. The reaction products were analyzed by on-line gas chromatograph HP 6890A.

3. RESULTS AND DISCUSSION

The Al- and Fe-MCM–58 zeolites were synthesized from the reaction gel with following molar compositions: (0.016–0.025) Al_2O_3: SiO_2: 38 H_2O: 0.30 K_2O: 0.10 BQ for Al–MCM–58 and (0.0125–0.025) Fe_2O_3: SiO_2: 38 H_2O: 0.30 K_2O: 0.20 BQ for Fe–MCM–58. The BQ, which is used as a structure directing agent in the MCM–58 synthesis, is relatively expensive. Thus the amount of BQ in the reaction mixture for Al–MCM–58 was lowered from the original molar ratio BQ : SiO_2 = 0.2 to 0.1. By optimizing the synthesis conditions and time at 170 °C it was possible to reproducibly synthesize highly crystalline zeolite Al–MCM–58 (Fig. 1A) with initial n_{Si}/n_{Al} ratios from 20 to 40. In the case of Fe–MCM–58 it was not possible to

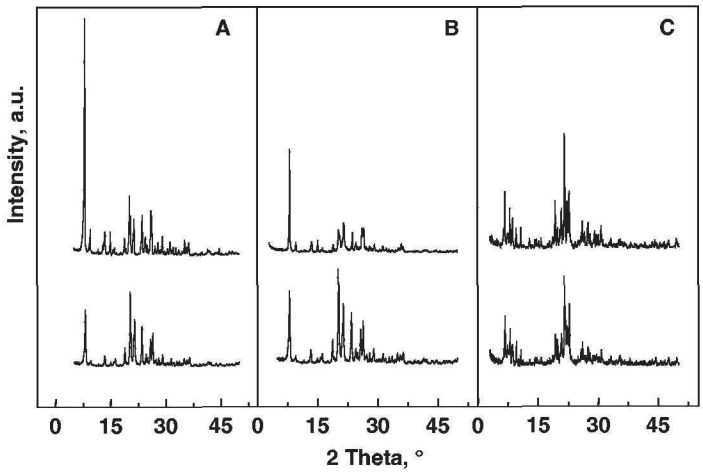

Fig. 1. X-ray powder diffraction patterns of as-made (a) and calcined (b) zeolites Al-MCM-58, n_{Si}/n_{Al} = 26 (A), Fe-MCM-58, n_{Si}/n_{Fe} = 26 (B), and Al-MCM-68, n_{Si}/n_{Al} = 9 (C).

synthesize this zeolite as a pure phase under the same conditions used for Al-MCM-58. The sample was always contaminated with α-quartz. To prevent the formation of α -quartz, the reaction temperature for the synthesis of Fe–MCM–58 was lowered to 155 °C and the synthesis time was optimized.

The optimum synthesis time was found to be between 4.5 and 5.5 days independent of the n_{Si}/n_{Fe} ratio in the gel (Fig. 1B). Al-MCM-68 was readily synthesized after 13 days at 160 °C. The powder X-ray diffraction pattern of as-synthesized and calcined Al-MCM-68 are depicted on the Fig. 1C.

The scanning electron micrographs (Fig. 2) of Al–MCM–58 (n_{Si}/n_{Al} = 26), Fe–MCM–58 (n_{Si}/n_{Fe} = 26), and Al-MCM-68 (n_{Si}/n_{Al} = 11) show that no amorphous phase is present. Crystals of Al–MCM–58 (Fig. 2A) are represented by elongated particles with length from 1 to 5 μm depending on the n_{Si}/n_{Al} ratio in the synthesis gel. The size of crystals increased with decreasing amount of aluminum in the reaction mixture.

The crystals of Fe–MCM–58 (Fig. 2B) are smaller in comparison with Al–MCM–58 with sizes between 0.5 and 3.0 μm. Some agglomeration of Fe–MCM–58 crystals to form stars was found, which is also typical for Fe–ZSM–12 [15].

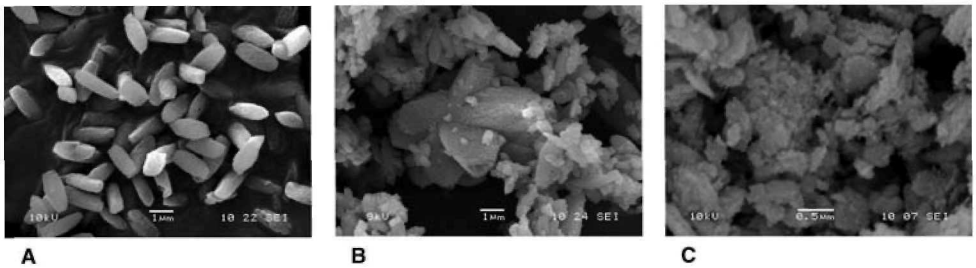

Fig. 2. Scanning electron micrographs of zeolites Al-MCM-58 with n_{Si}/n_{Al} ratio = 26 (A), Fe-MCM-58 with n_{Si}/n_{Fe} ratio = 26 (B) and Al-MCM-68 with n_{Si}/n_{Al} ratio = 11 (C).

Al-MCM-68 crystals appear like agglomerates of particles smaller then 0.5 μm (Fig. 2C).

The type and concentration of the acid sites were determined after adsorption of probe molecules such as d_3–acetonitrile and pyridine on the activated aluminum and iron zeolites, respectively. Spectra of Al–MCM–58 and Al-MCM-68 in the region of OH groups before and after adsorption of d_3–acetonitrile are depicted in Fig. 3A,a and Fig. 5A,a, respectively. The absorption bands at 3746 and 3745 cm^{-1} belong to terminal Si–OH groups of Al MCM-58 and Al-MCM-68, respectively, and two bands at 3630 and 3564 cm^{-1} for Al-MCM-58 and 3610 and 3575 cm^{-1} for Al-MCM-68 are characteristic for bridging OH groups. The band at 3676 cm^{-1} in the spectra of Al-MCM-68 (Fig. 5A,a) was ascribed to OH groups on nonframework aluminum species. After adsorption of d_3-acetonitrile this band vanished. After the interaction with d_3–acetonitrile, new bands of Lewis sites at 2327 cm^{-1}, and Broensted sites 2297 cm^{-1} (Al-MCM-58) and 2298 cm^{-1} (Al-MCM-68) are formed (Fig. 3B,b and Fig. 5B,b).

In the case of Fe–MCM–58, absorption bands with maxima at 3746 cm^{-1} for terminal Si–OH groups and 3646 cm^{-1} and 3520 cm^{-1} for bridging Si–OH–Fe groups (Fig. 4A,a) were detected. Pyridine adsorption leads to the consumption of all bridging Si–OH–Fe groups (Fig. 4A,b) and to the formation of a band at 1545 cm^{-1} characteristic for the presence of the pyridinium ion, which reflects the interaction of pyridine with Broensted sites. The band at 1448 cm^{-1} originates from coordinatively bonded pyridine on Lewis sites (Figure 4B,b). The determined concentrations of Broensted and Lewis acid sites for Al– and Fe–MCM–58, and Al-MCM-68 are summarized in Table 1.

The concentration of the Broensted acid sites in Al–MCM–58 and Al-MCM-68 is practically constant despite the n_{Si}/n_{Al} ratio, while it slightly decreases with increasing n_{Si}/n_{Fe} ratio. In other words, the higher the concentration of trivalent atoms in the zeolite, the higher the concentration of Lewis sites. The concentration of Broensted sites strongly depends on the type of the trivalent cation.

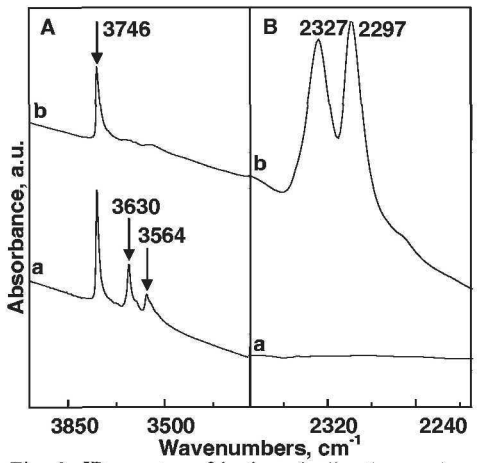

Fig. 3. IR spectra of hydroxyl vibration region of Al-MCM-58 with n_{Si}/n_{Al} = 26 before (a) and after (b) d_3-acetonitrile adsorption (A) and spectra of acetonitrile region before (a) and after (b) its adsorption (B).

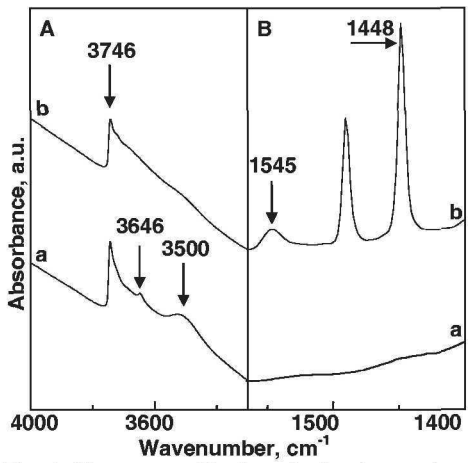

Fig. 4. IR spectra of hydroxyl vibration region of Fe-MCM-58 with n_{Si}/n_{Fe} = 26 before (a) and after (b) pyridine adsorption (A) and spectra of pyridine region before (a) and after (b) its adsorption (B).

Table 1
n_{Si}/n_{Al} and n_{Si}/n_{Fe} ratios of zeolites Al-MCM-58, Fe-MCM-58, and Al-MCM-68 in the initial gel and in the synthesized zeolite determined by XRF and FTIR and relative amount of Lewis and Broensted acid sites.

Zeolite	$(n_{Si}/n_{Al(Fe)})^{I}$	$(n_{Si}/n_{Al(Fe)})^{XRF}$	$(n_{Si}/n_{Al(Fe)})^{FTIR}$	BS, %	LS, %
Al-MCM-58					
A	20	16	16	57	43
B	30	19	17	62	38
C	40	26	21	61	39
Fe-MCM-58					
D	20	18	19	14	86
E	30	26	27	11	89
F	40	34	32	6	94
Al-MCM-68					
G	9	11	12	41	59
H	13	15	17	43	57
I	20	19	19	49	51

I – initial, XRF – X-ray fluorescent spectroscopy, FTIR – infrared spectroscopy, BS – Broensted sites, LS – Lewis sites

While about 50 % of the acid sites are of the Broensted type in the Al–containing MCM–58 samples, only about 8–16 % of the total acid sites are Broensted sites in Fe–MCM–58. On one side, the concentration of trivalent cations in the synthesized sample is larger for Fe than for Al, on the other side, the concentration of Broensted sites is significantly lower for Fe–MCM–58 than for Al–MCM–58. Due to the relatively large ionic radius of Fe^{3+} (0.063 nm) compared to Si^{4+} and Al^{3+} (0.040 nm and 0.053 nm, respectively), the incorporation of iron into the framework is expected to be much more complicated.

The toluene alkylation with isopropylalcohol was investigated over zeolites Al-MCM-58, Fe-MCM-58 and Al-MCM-68 possessing different $n_{Si}/n_{Al(Fe)}$ ratios. The main product of the isopropylation of the toluene is a mixture of cymenes. However, the reaction over aluminum zeolites is accompanied by competitive reactions yielding benzene, xylenes, ethyltoluenes, and *n*-propyltoluenes. The conversion of toluene was quite stable with T-O-S for all tested zeolites (Fig. 6). The toluene conversion was high for aluminum zeolites MCM-58 and MCM-68 (between 14 and 19 %) which possess relatively high amount of Bronsted sites. n-Propyltoluenes and xylenes (except cymenes) were formed in significant concentrations over aluminum containing zeolites. After 15 min the selectivity to xylene was 14 – 23 % and selectivity to n-propyltoluene between 6 and 9 % for alumosilicates. It was shown that the inner structure of zeolites controls the formation of *n*-propyl benzenes or *n*-propyltoluenes in alkylation reactions [6]. It was proposed that *n*-propyltoluene formation is taking place via a bimolecular reaction between isopropyltoluene and excess of toluene in the reaction mixture. The reaction between isopropyltoluene and toluene can take place on the channel intersection of zeolites with three dimensional channel systems as in ZSM-5 or MCM-68. On the contrary, this reaction is sterically hindered in zeolites with one dimensional channel system as mordenite [16,17].

However, a significant amount of *n*-propyltoluene is also formed in MCM-58 that has one dimensional channel system. It was explained by the size of the channel system (12 MR) and by the location and geometry of SDA used for the synthesis. The SDA structure is similar to

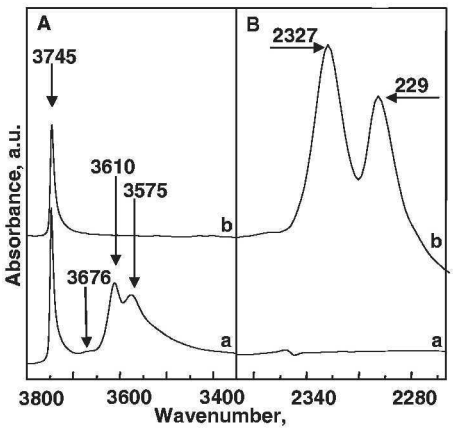

Fig. 5. IR spectra of hydroxyl vibration region of Al-MCM-68 with n_{Si}/n_{Al} = 9 before (a) and after (b) d_3-acetonitrile adsorption (A) and spectra of acetonitrile region before (a) and after (b) its adsorption (B).

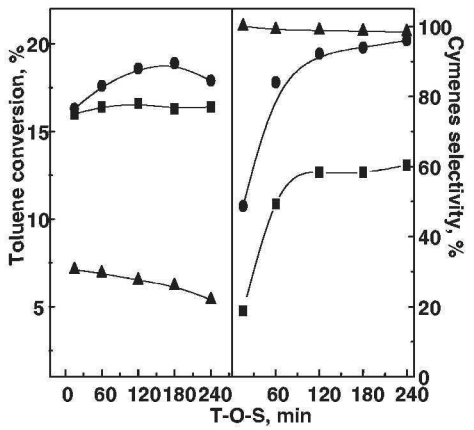

Fig. 6. T-O-S dependence of toluene conversion and cymenes selectivity over Al-MCM-58, n_{Si}/n_{Al} ratio = 26 (■), Fe-MCM-58, n_{Si}/n_{Fe} ratio = 26 (▲), and Al-MCM-68, n_{Si}/n_{Al} ratio = 19 (●).

the structure of bimolecular intermediate which is required for *n*-propyltoluene formation [18].

For the Fe-MCM-58 of OH groups of lower acid strength compared to aluminum analogues the conversion of toluene was lower. The lower acidity of iron zeolites suppressed competitive reactions and, thus, only cymenes were formed during the reaction. Selectivity to cymenes increased with longer T-O-S, while the selectivity to n-propyltoluenes decreased. This can be explained by an increasing deactivation of the catalysts.

From comparison of toluene conversion for different n_{Si}/n_{Al} ratios of zeolites was found that the toluene conversion was not dependent on the concentration and type of acid sites for Al-MCM-58, Fe-MCM-58 and Al-MCM-68. These results support the hypothesis of Čejka et al. that the controlling step of the reaction is transport and desorption of bulky molecules from the inner space of zeolites.

4. CONCLUSIONS

Zeolite MCM–58 be readily synthesized containing Al and Fe in the framework using N–benzylquinuclidinium bromide as the structure directing agent. Synthesis of Al–MCM–58 was accomplished at concentration the range of n_{Si}/n_{Al} ratios 16 to 26 under dynamic conditions at 170 °C for 7 days.

Incorporation of iron into the zeolite framework is more complicated. The synthesis requires a lower temperature and higher concentration of the template(SiO_2/BQ = 0.2). The synthesis was carried in the range of n_{Si}/n_{Fe} ratios from 18 to 34 under dynamic conditions at 155 °C for 5 days.

The novel zeolite Al-MCM-68 was synthesized with the n_{Si}/n_{Al} ratios = 11, 15 and 19 under static conditions at 160 °C. The optimum time for the synthesis was found to be 13 days. The acid forms alumosilicates contain significant amounts of Broensted acid 57 - 61 %

(Al–MCM–58) and 41 - 49 % (Al-MCM-68), respectively. Fe–MCM–58 contain nearly 90 % of Lewis acid sites.

The results of catalytic test show that for alumosilicate MCM-58 and MCM-68 the toluene conversion is not dependent on the amount and strengths of acid sites. Therefore, it was concluded, that the alkylation of toluene with isopropanol is controlled by the transport/desorption step of the bulky reaction products from the inner space of zeolites. Significant amount of *n*-propyltoluenes was confirmed during first 15 min over aluminum zeolites. It was found that the structure of these zeolites controls the reaction bimolecular process leading to n-propyltoluenes as products. The lower acid strength of Fe-silicates leads to the suppression of competitive reactions and, as a result, cymenes are predominately formed.

Acknowledgement

Financial support of the Grant Agency of the Academy of Sciences of the Czech Republic (B4040402). I would like to thank Dr. Libor Brabec for recording scanning electron micrographs and Dr. Jiří Čejka for motivation and helpful discussion.

REFERENCES

[1] M.C. Camblor, A. Corma and L.A. Villaescusa, Chem. Commun., 8 (1997) 749.
[2] W.W. Kaeding, L.B. Young and C.C. Chu, J. Catal., 89 (1984) 267.
[3] C. Perego and P. Ingallina, Catal. Today, 76 (2002) 87.
[4] J. Čejka, G.A. Kapustin and B. Wichterlová, Appl. Catal. A, 108 (1994) 187.
[5] C.S. Cundy and P.A. Cox, Chem. Rev., 103 (2003) 663.
[6] J. Čejka and B. Wichterlová, Catal. Rev., 44 (2002) 375.
[7] A. Corma, G. Sastre and P.M. Viruela, J. Mol. Catal. A, 100 (1995) 75.
[8] A. Corma, M.J. Diaz-Cabanas, F. Rey, S. Nicolooulas and K. Boulahya, Chem. Commun. (2004) 1356.
[9] A. Burton, S. Elomari, R.C. Medrud, I.Y. Chan, C.Y. Chen, L.M. Bull and E.S. Vittoratos, J. Am. Chem. Soc., 125 (2003) 1633.
[10] P. Prokešová, S. Mintová, J. Čejka and T. Bein, Microporous Mesoporous Mater., 64 (2003) 165.
[11] S. Ernst, M. Hunger and J. Weitkamp, Chem. Ing. Tech., 69 (1997) 77.
[12] D.C. Calabro, J.C. Cheng, R.A. Crane, C.T. Kresge, S.S. Dhingra, M.A. Steckel, D.L. Stern and S.C. Weston, US Patent No. 6 049 018 (2000).
[13] B. Wichterlová, Z. Tvarůžková, Z. Sobalík and P. Sarv, Microporous Mesoporous Mater., 24 (1998) 223.
[14] C.A. Emeis, J. Catal., 141 (1993) 347.
[15] G. Košová and J. Čejka, Collect. Czech. Chem. Commun., 67 (2002) 1760.
[16] J. Čejka, N. Žilková, J. E. Šponer and B. Wichterlová, Collect. Czech. Chem. Commun., 63 (1998) 1769.
[17] J. Šponer, J. Šponer, J. Čejka and B. Wichterlová, J. Phys. Chem. B, 102 (1998) 7169.
[18] J. Čejka, A. Krejčí, N. Žilková, J. Kotrla, S. Ernst and A. Weber, Microporous Mesoporous Mater., 53 (2002) 121.

Studies in Surface Science and Catalysis, volume 158
J. Čejka, N. Žilková and P. Nachtigall (Editors)

Fabrication of TS-1 via microwave and catalytic properties

Y.H. Lee, K.–M. Choi, S.–C. Han, and S.–E. Park*

Laboratory of Nano-Green Catalysis, Department of Chemistry Inha University, 253 Yonghyun-dong, Nam-Gu, Incheon 402-751, South Korea; separk@inha.ac.kr

Nanostacked zeolite having MFI-structure contained titanium metal ions on its framework, has been prepared via microwave irradiation. Nanofabrication of titanium containing MFI zeolitic materials under microwave irradiation was successfully implemented by the adhesion of crystallites through the condensation of hydroxyl groups on surface via selective adsorption of microwave energy onto high dielectric metal species including Ti species as a nanoglue. This microwave technique gave births of both the uniform size of hockey puck shaped crystals and the fibrous stacked morphology of MFI crystals. This material gave superior adsorption selectivity of linear hydrocarbons such as n- hexane, n-octane and both increased of activity and selectivity in the epoxidation of styrene into styrene epoxide.

1. INTRODUCTION

Microwave techniques have attracted growing attention for the rapid synthesis of nanoporous materials requiring several days to prepare under hydrothermal conditions [1-10]. Potential advantages include a rapid and more simultaneous nucleation and growth, homogeneous heating throughout the reaction vessel, superheating, and suppression of undesired phases compared with conventional hydrothermal techniques. To date, several types of mesoporous materials as well as microporous zeolites have been synthesized by microwave irradiation. Microwave techniques in the synthesis of inorganic materials are generally known to be faster and simpler than conventional methods [11]. Energy transfer from microwaves to the materials is believed to occur either through resonance or relaxation, which results in rapid heating. Furthermore, the employment of the microwave technique in the synthesis of nanoporous materials have been shown to provide versatile effects, for instance, short heating times, inductive heating through the conducting properties of the synthesis mixture, specific energy dissipation via microwave energization of the hydroxylated surface or associated water molecules in the boundary layer, and formation of the high potential of the active water molecules [2, 6, 8].

Zeolite molecular sieves are good candidates for designed microscopically and nanoscopically engineered materials due to their well-defined pore structures [12-13]. Among them, silicalites, zeolites having the MFI framework topology, have been studied extensively with regards to the selective separation of hydrocarbons [14] and the development of electrode materials [15], membranes [16], and catalysts [17]. Because many emerging applications of porous materials require precise control of crystal size, shape, and orientation [18, 19], the development of new synthesis strategies is increasingly important. For example, the properties of spherical mesoporous silica particles with a narrow particle size distribution as a material for column chromatography are superior to those of curved hexagonal rods with

the same structure [19]. Recently, it has been reported that the microwave synthesis method could provide an efficient way to control particle size distribution [20], phase selectivity [21], and macroscopic morphology [22] in the synthesis of porous materials as well as result in fast crystallization [23]. However, to our knowledge, there are few reports of microwave techniques being utilized to control the morphology of porous materials [22]. Here, we report on new applications of the microwave method for the fabrication of MFI-type zeolite crystals incorporating Ti and other metal species. By using the method, we prepared fibrous MFI zeolites that exhibited useful physicochemical properties due to their self-stacking. Pure and metal-incorporated MFI crystals were synthesized by microwave-heating precursor solutions at 438 K. Our recent results reveal that the TS-1 can be used as a convenient catalyst for the shape selective production of *p*-xylene [24].

In this report, nanostacked Ti-MFI zeolite was successfully prepared by microwave irradiation. It was demonstrated adsorption of linear aliphatic hydrocarbons such as n-hexane and n-octane in liquid phase as a superior catalyst in the selective epoxidation reaction of styrene into styrene epoxide.

2. EXPERIMENTAL

Nanostacked Ti-MFI zeolite was synthesized using tetrapropyl orthotitanate (TPOT, Aldrich, 98 %), TEOS (Tetraethyl orthosilicate, TCI, 98 %), isopropyl alcohol (IPA, TCI) and deionized water. Tetrapropylammonium hydroxide (TPAOH) was used as a structure-directing agent. Typically two kinds of different solution A and B were prepared respectively. The total molar ratio of gel composition is 0.1TEOS: 0.0014 TPOT: 0.02 TPAOH: 0.1IPA: 2.22H_2O. In case of A solution, firstly 20.35mL (0.02mol) of TPAOH was added in 22.2mL of deionized water and then 22.38mL (0.1mol) TEOS were added in this mixture with continuously stirring to give the homogeneously mixed sol-gel solution. In a separate vessel B, TPOT was dissolved in 6 mL of isopropyl alcohol by continuously stirring. Finally solution B was poured into the A with vigorous stirring and heated up to 80 ℃ to remove isopropyl alcohol for 1 hour. The precursor gel of 30–60 g was loaded in a 100 ml Teflon autoclave, which was sealed and placed in a microwave oven (CEM, Mars-5, maximum power of 1200 W). The precursor gel was heated to the reaction temperature of 180°C in less than 2 min (microwave power was 600 W) and kept for 1 or 2 h (microwave power was 300 W). After the reaction, the autoclave reactor was cooled to room temperature, and the solid product was separated with filtration and washed with deionized water for several times. It was dried overnight at 105 °C. There was no extra separation procedure to remove impurities or amorphous gel. The molecular sieves were calcined at 550°C in an electric furnace.

The crystallinity of stacked Ti-MFI sample was determined with an X-ray diffractometer (Tigaku, D/MAX IIIB) using Cu Kα radiation, and titanium contents were determined with an inductively coupled plasma (ICP, Jovin Yvon Ultima-C). FT-IR spectra were obtained with a Nicolet Impact 410 spectrometer in the range of 500-4000cm^{-1}. The measurement of chemisorption property upon these linear hydrocarbons was carried out with a Chemisorb 2705 Micromeritics.

Styrene epoxidation was carried out using a glass flask equipped with a reflux condenser, a magnetic stirrer, a thermometer and a septum to withdraw samples periodically for analysis. Catalyst of 0.35g, 18 mL acetone as solvent, 5 mL styrene (99%, Aldrich) and 1.3 mL aqueous hydrogen peroxide solution (30 wt%) were loaded into the flask. The molar ratio of styrene/H_2O_2 was 3.4. The reaction was performed at 70 °C under ambient atmosphere. The

liquid mixture was separated from catalyst, and analyzed using a gas chromatography (YoungLin GC, Korea) equipment with a flame ionization detector and a capillary column (DP-sil-5 CB). The column temperature was 100 °C and the carrier gas was helium. .

3. RESULTS AND DISCUSSION

MFI-type zeolite crystal incorporated with Ti species was prepared by microwave irradiation and applied to both the oxidative styrene epoxidation reaction and the length shape-selective sorption reaction with two kinds of linear hydrocarbons such as n-hexane and n-octane. The powder X-ray diffraction (XRD) patterns of Ti-MFI sample which is prepared by microwave and hydrothermal treatment show the characteristic peaks for the MFI structure without any impurities. The IR spectra of the calcined Ti-MFI samples exhibit an absorption band at 960 cm^{-1} for the stretching mode of a [SiO_4] unit bonded to a Ti^{4+} ion (O_3SiOTi). UV/Vis diffuse reflectance spectra, collected in vacua after evacuation ($\leq 10^{-5}$ torr) at 627 K, revealed a strong peak around 210-240 nm, assignable to the ligand-to-metal charge-transfer absorption band from the oxygen to tetrahedral titanium (IV) atom in the zeolite framework.

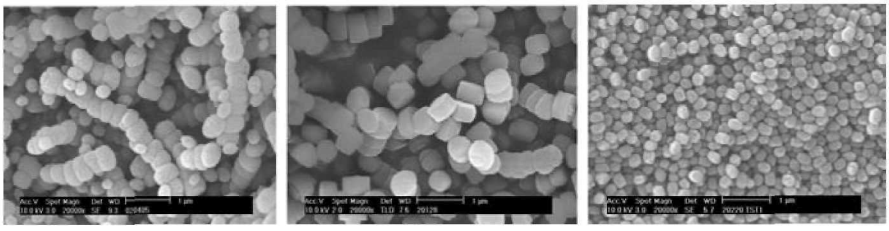

(a) (b) (c)

Fig. 1. SEM images of (a) fibrous Ti-MFI zeolite with microwave irradiation (stacked Ti-MFI-MW) and (b) Ti-MFI with microwave irradiation (non-stacked Ti-MFI-MW, nonstaking) (c) hockey-puck shape Ti-MFI zeolite with hydrothermal heating (Ti-MFI- HT).

Fig. 1a shows both the uniform size of hockey puck shaped crystals and the stacking of these crystals into fiber or rod types in the synthesis of zeolitic materials such as MFI type zeolites. The formation of these nanostacked MFI-type zeolite crystals having nanorod shape was ascribed to the presence of metal species, which selectively absorbed microwave irradiation. Self-assembled zeolite nanostructures can be also obtained by modification of the zeolite surface by putting metal species as nanoglue.

The nanofabricated materials like the stacked Ti-MFI zeolite showed significantly enhanced shape selectivity in adsorption. Fig. 2 shows the temperature-programmed desorption (TPD) profiles of linear hydrocarbons after vapor-phase adsorption of an equimolar mixture of n-hexane and n-octane over stacked Ti-MFI-MW and Ti-MFI-HT at 100 °C. The linear hydrocarbons TPD patterns are similar over the two adsorbents, that is, two peaks for n-hexane and n-octane, while the fibrous Ti-MFI-MW reveals a remarkably enhanced adsorption selectivity on n-hexane. Moreover, it is notable that stacked Ti-MFI-MW selectively desorbs n-hexane in the temperature range 100-200 °C (Fig. 2a), implying that this material can be applied in producing a selected n-hexane from a linear hydrocarbon mixture when combined with temperature swing desorption.

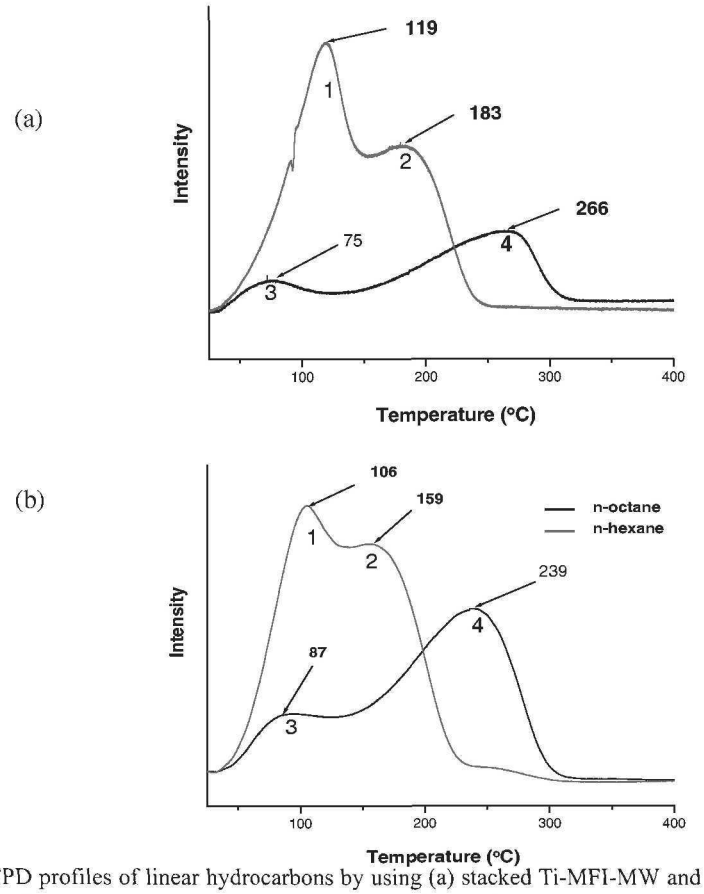

Fig. 2. TPD profiles of linear hydrocarbons by using (a) stacked Ti-MFI-MW and (b) non-stacked Ti-MFI-HT after vapor-phase competitive adsorption of an equimolar mixture of n-hexane (red full line) and n-octane (black full line). Adsorbent weight: 0.25g; carrier gas: nitrogen (flow rate = 30 $mLmin^{-1}$)

The MFI structure was known to offer three different sites for adsorption: straight and sinusoidal channels along the [010] and [100] directions, respectively, and their intersections. Thé diffusivity in the straight channel is reportedly much higher than in the sinusoidal channel. Because of the crystal stacking along the [010] direction, the straight channels of Ti-MFI-MW are longer and their openings are much fewer than those of the non- stacked Ti-MFI-HT [25]. Fig. 3 shows the rate of styrene conversion in oxidative epoxidation of styrene over Ti-MFI zeolite at 373K, which were prepared by microwave irradiation and hydrothermal treatment. All samples show initial induction periods in the first 30 min of the reactions, in which the Ti-MFI-HT catalyst has a relatively lower conversion rate than those of stacked or non-stacked Ti-MFI-MW. After this initial period, the oxidative styrene conversion rate over all samples gradually increases. The highest rate at about 3 hour: the conversion rate of styrene over Ti-MFI-HT and stacked Ti-MFI-MW is nearby 37% and 40% respectively, while stacked Ti-MFT-MW catalyst reaches around 150%. In addition, with the increase of reaction time, the

tendency of styrene conversion over these two samples, Ti-MFI-HT and non-stacked Ti-MFI-MW, is almost the same. In case of stacked Ti-MFI-MW, the conversion of styrene, however, gives higher value from 2 hours.

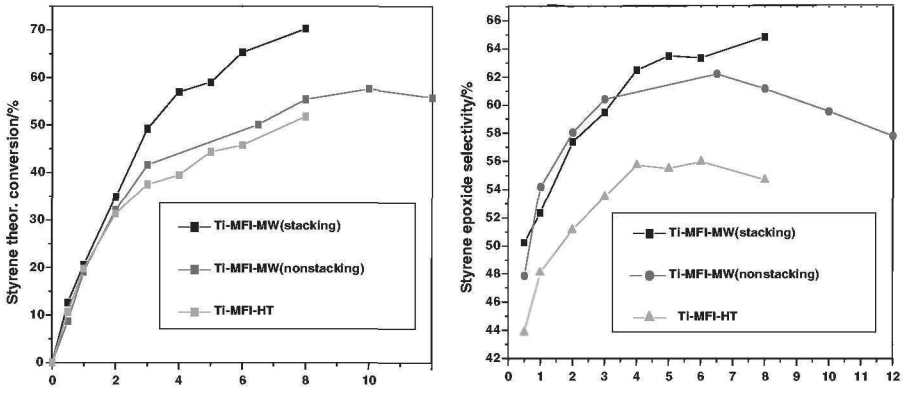

Fig. 3. Tendencies of (a) conversion and (b) selectivity for styrene epoxidation reaction with stacked and non-stacked Ti-MFI zeolite prepared by microwave (MW) and hydrothermal treatment (HT) respectively. Adsorbent weight: 0.35g ; molar ratio of styrene/H_2O_2: 3.4 ; carrier gas: helium (flow rate=30mL/min); reaction temperature: 373K.

At the same time the total selectivity on aromatic styrene epoxide through the stacked Ti-MFI-MW (65 %) is higher than non-stacked Ti-MFI-MW (62%) and Ti-MFI-HT (55%). Catalytic activities of the stacked Ti-MFI-MW are increased after catalytic reaction for 6 hours, while non-stacked Ti-MFI-MW and Ti-MFI-HT are gradually decreased at the same time. It is clear that the reason of high conversion of stacked Ti-MFI-MW in comparison with the other two samples is likely to induce from the nanofabrication such as nanostaking which was formed through hydration reaction between hydroxyl group existing on the surface of microporous material and adsorption of microwave energy. In addition, it seems that high surface area through crystal growth of c- direction and the metal incorporation at a suitable concentration level by selective adsorption of microwave energy will be able to enhance catalytic property.

In summary, metal elements, which are located on the surface of zeolite crystals, behave as a nanoglue between the crystals through selective absorption of microwave energy. Nanostacked Ti-MFI zeolite by microwave is of great interest for various applications, for example, in the oxidative epoxidation reaction between styrene and hydrogen peroxide as well as selective separation of linear hydrocarbon from a mixture. Nanofabrication of zeolite crystals show several interesting properties such as lower packing density, higher hydrophobicity, enhanced catalytic properties, and higher shape-selectivity in adsorption as compared to non-fabricated MFI zeolite.

REFERENCES

[1] A. Arafat, J.C. Jansen, A.R. Ebaid, H. van Bekkum, Zeolites 13 (1993) 162.
[2] C.S. Cundy, R.J. Plaisted, J.P. Zhao, Chem. Commun., (1998) 1465.
[3] Y.K. Hwang, J.-S. Chang, Y.-U. Kwon, S.-E. Park, Stud. Surf. Sci. Catal., 146 (2003) 101.
[4] S.H. Jhung, J.-S. Chang, Y.K. Hwang, S.-E. Park, J. Mater. Chem., 14 (2004) 280.
[5] S.H. Jhung, J.-S. Chang, J.S. Hwang, S.-E. Park, Microporous Mesoporous Mater., 64 (2003) 33.
[6] S.-E. Park, Y.K. Hwang, D.S. Kim, S.H. Jhung, J.S. Hwang, J.-S. Chang, Catal. Surv. Asia, 8 (2004) 91.
[7] C.G. Wu, T. Bein, Chem. Commun., (1996) 925.
[8] S.-E. Park, D.S. Kim, J.-S. Chang, W.Y. Kim, Catal. Today, 44 (1998) 301.
[9] H.M. Sung-Suh, D.S. Kim, Y.K. Park, S.-E. Park, Res. Chem. Intermed., 26 (2000) 283.
[10] D.S. Kim, J.M. Kim, J.-S. Chang, S.-E. Park, Stud. Surf. Sci. Catal., 135 (2001) 333.
[11] (a) J. Zhu, O. Polchik, S. Chen, A. Gedanken, J. Phys. Chem., B104 (2000) 7344; (b) K.J. Rao, B. Vaidhyanathan, M. Ganguli, P.A. Ramakrishnan, Chem. Mater., 11 (1999) 882.
[12] (a) G. A. Ozin, Adv. Mater. 1992, 4, 612; b) T. Bein, Chem. Mater., 8 (1996) 1636.
[13] M.E. Davis, Nature, 417 (2002) 813.
[14] (a)W. Yuan, Y. S. Lin, W. Yang, J. Am. Chem. Soc., 126 (2004) 4776; (b) .S. Li, C. Demmelmaier, M. Itkis, Z. Liu, R. C. Haddon, Y. Yan, Chem. Mater., 15 (2003) 2687.
[15] S. Li, X. Wang, D. Beving, Z. Chen, Y. Yan, J. Am. Chem. Soc., 126 (2004) 4122.
[16] G. Xomeritakis, Z. Lai, M. Tsapatsis, Ind. Eng. Chem. Res., 40 (2001) 544.
[17] (a) B. Notari, Adv. Catal. 41 (1996) 253; (b) V. Ramaswamy, B. Tripathi, D. Srinivas, A. V. Ramaswamy, R. Cattaneo, R. Prins, J. Catal., 200 (2001) 250.
[18] C. Thoelen, J. Paul, I. F. J. Vankelecom, P. A. Jacobs, Tetrahedron: Asymmetry, 11(2000) 4819.
[19] Z. Lai, G. Bonilla, S. Diaz, J.G. Nery, K. Sujaoti, M.A. Amat, E. Kokkoli, O. Terasaki, R. W. Thompson, M. Tsapatsis, D.G. Vlachos, Science, 300 (2003) 456.
[20] (a) C. S. Cundy, Collect. Czech. Chem. Commun., 63 (1998) 1699; (b) C. Gabriel, S. Gabriel, E. H. Grant, B. S. J. Halstead, D. M. P. Mingos, Chem. Soc. Rev., 27 (1998) 213.
[21] S. H. Jhung, J.-S. Chang, J.-S. Hwang, S.-E. Park, Microporous Mesoporous Mater., 64 (2003) 33.
[22] (a) S. H. Jhung, J.-S. Chang, Y. K. Hwang, S.-E. Park, J. Mater. Chem., 14 (2004) 280; (b) Y. K. Hwang, J.-S. Chang, Y.-U. Kwon, S.-E. Park, Microporous Mesoporous Mater., 68 (2004) 280.
[23] (a) B. L. Newalkar, S. Komarneni, H. Katsuki, Chem. Commun., 2389 (2000); (b) S. Mintova, S. Mo, T. Bein, Chem. Mater., 10 (1998) 4030.
[24] Y. K. Hwang, J.-S Chang, S. –E. Park, D. S. Kim, Y.-U. Kwon, S. H. Jhung, J.-S. Hwang, and M. S. Park, Angew. Chem. Int. Ed., 44 (2005) 557
[25] S. Nair, M. Tsapatis, J. Phys. Chem. B, 104 (2000) 8982.

Studies in Surface Science and Catalysis, volume 158
J. Čejka, N. Žilková and P. Nachtigall (Editors)

Room temperature synthesis: an efficient way for studying the zeolite formation

V.P. Valtchev[a*], K.N. Bozhilov[b], M. Smaihi[c], L. Tosheva[a]

[a] Laboratoire de Matériaux à Porosité Contrôlée, UMR-7016 CNRS, ENSCMu, Université de Haute Alsace, 3, rue Alfred Werner, 68093 Mulhouse Cedex, France, *V.Valtchev@uha.fr

[b] Central Faculty for Advanced Microscopy and Microanalysis, University of California, Riverside, CA 92521, USA

[c] IEM UMR-5635 CNRS, 1919 route de Mende, 34293 Montpellier, Cedex 5, France

The synthesis and the detail investigation of the formation of LTA- and FAU-type zeolites at room temperature (RT) are reported. The complete transformation of the amorphous precursors into zeolite A and X took place for 3 and 21 days, respectively. The events taking place at the nanometer scale were studied by high resolution transmission electron microscopy (HRTEM). The study was completed by small angle X-ray scattering (SAXS) and X-ray diffraction (XRD).The sluggish crystal growth kinetics at ambient conditions permitted to track down the entire sequence of crystallization events from the formation of the initial gel to the complete transformation into a zeolite-type material. Liquid inclusions denoted as "negative crystals" were found within the volume of the gel particles for both systems. Further, the crystal growth was followed by HRTEM, which revealed that the crystallization in the two systems is governed by different crystallization mechanism.

1. INTRODUCTION

There are continuous efforts in understanding the mechanism of zeolite crystallization [1-5]. The interest is driven from both fundamental and practical point of view [6]. The development of new powerful characterization techniques allows the constant acquisition of new data about the crystallization mechanism of different zeolite systems. However, the zeolite crystallization is complex and unique for a particular zeolite type and no universal mechanism could be proposed. Even for well-known zeolites like NaA and NaX, which are amongst the most studied zeolites, there are still uncertainties, regarding the mechanism of their formation [7-10].

The events in the early stages are of paramount importance in determining the course of the subsequent crystallization and it is clear that a detailed understanding of these phenomena should be obtained if the goal of a rational control of the synthesis of these materials is to be achieved. Different sets of complementary techniques have been used to gain an insight into the complex processes occurring during the nucleation [11, 12]. However, a serious obstacle in studying the zeolite formation are the invasive post-synthesis sampling procedures that may provoke redistribution of the (alumino)silicate species, particle growth, and possibly

nucleation. Part of these difficulties were circumvented by in situ investigations, for instance NMR [13,14] IR/Raman [15] EXAFS [16] optical and electron microscopy [17], light-scattering techniques [18,19] X-ray diffraction [20-22] and combinations of SAXS/SANS [23,24], SAXS/WAXS [25,26] and synchrotron X-ray radiation [27], which provided valuable information about the zeolite crystallization mechanism. Nevertheless, important questions like for instance where the first unit cells of zeolite structure are formed, their spatial arrangement in the gel system, and what are the species depositing on the growing crystals remain to be elucidated.

We have found a simple and effective way to study zeolite the crystallization by synthesizing zeolites at room temperature. The slow crystal growth kinetics at room temperature allows to discriminate the different stages of the zeolite formation and to study the products of crystallization with minimum invasive post-synthesis treatments. The present study reports on the synthesis and investigation of the nucleation and crystal growth mechanisms of LTA- and FAU-type zeolites under ambient conditions.

2. EXPERIMENTAL

2.1. Synthesis

In order to obtain LTA- and FAU-type zeolite in a reasonable period of time under ambient conditions, a very reactive systems were employed. A silica source containing low-mass silica species was used and further de-polymerized by adding sodium hydroxide so as to obtain a completely transparent initial solution. The latter was mixed with a clear aluminate solution where $Al(OH)^-_4$ is the dominant anionic species [1]. The zeolite precursor mixtures were produced by vigorous mixing of the alkaline silicate and aluminate solutions, prepared as described above, where all components were expected to be relatively homogeneously distributed. The compositions of the gels employed for the syntheses were as follows:

Zeolite A: $6Na_2O : 0.2Al_2O_3 : 1.0SiO_2 : 150H_2O$

Zolite X: $4Na_2O : 0.2Al_2O_3 : 1.0SiO_2 : 200H_2O$

The reactants used for the preparation of the gel were: sodium hydroxide pellets (97%, (Aldrich), sodium aluminate (54.3% Al_2O_3, 44.5% Na_2O, Riedel-de Haën), sodium silicate solution (14 % NaOH, 27% SiO_2, Fluka) and distilled water. The mixture kept its transparent character for several seconds and after that turned into a milky-white low viscosity gel. The initial mixtures were stirred for 90 min and transferred into polypropylene bottles. The sealed bottles were stored in an oil bath (T=25 ±1°C). The milky-white color and the observed sedimentation revealed that the gel comprised relatively large particles. Small aliquots of the mixtures were taken at different periods of time. Prior to taking aliquots, the samples were shaken in order to disperse the settled particles. During the first day, three samples were taken from the system yielding FAU-type material, immediately after homogenization of the gel (1.5 h), after 6 h and after 24 h. Thereafter, further samples were taken every 2-3 days. Samples from the zeolite A yielding system were taken after 0, 6, 21, 29, 44, 52, 67, 73 and 96 h. The solids were recovered by high speed centrifugation (g=50 000) and re-dispersion in distilled water under ultrasonic radiation. Part of each solid was dried at room temperature and the other part was kept as a suspension.

2.2. Characterization

The structural evolution of the gel species was tracked down with a high-resolution transmission electron microscopy (HRTEM), in a FEI-Philips CM300 microscope in low-dose mode operating at 300 kV accelerating voltage, equipped with a LaB_6 electron gun, and

EDAX energy dispersive X-ray spectrometer (EDS). Samples were prepared by diluting the suspension of the reaction products in distilled water, ultrasonicating them, and depositing a drop onto Cu grids coated with a thin (5 nm thickness) holey carbon support film. In order to verify that the zeolite crystals do not collapse under the high vacuum in the TEM, some of the samples were studied at liquid nitrogen temperature using Gatan Inc. cryo-system, model 626. No apparent increase in crystallinity or size distribution was observed, which allowed us to conclude that the utilization of low-dose technique at room temperature is an adequate method for characterization.

To complement this study, X-ray diffraction (XRD) and small angle X-ray scattering (SAXS) were performed. The XRD diagrams of the samples were recorded on a STOE STADI-P diffractometer in Debye-Scherrer geometry equipped with a linear position-sensitive detector (6° in 2θ) and employing Ge monochromated Cu $K\alpha_1$ radiation. SAXS measurements were done with a high resolution spectrometer (Bonse Hart Camera).

3. RESULTS AND DISCUSSION

The XRD studies of the product solids showed that zeolite A and X were successfully synthesized under RT conditions. The crystallization of zeolite X took much longer time than that of zeolite A. No changes in the X-ray crystallinity of the FAU-type material were observed after 3 weeks of RT synthesis, whereas zeolite A reached maximum crystallinity only after 3 days of treatment. On the other hand, the induction period for zeolite A was much longer in respect to zeolite X if we consider the ratio between the induction and crystallization time. Thus, the induction period for zeolite A was about 2/3 (44 h), while for zeolite X was 1/2 (ca. 10 days) of the total crystallization time. The difference in the relative induction times is surprising having in mind the higher alkalinity and lower water content of the zeolite A yielding system. These differences in the composition should provide a higher nucleation rate in the case of zeolite A. Besides the ratio between the induction and the total crystallization times, the two zeolites seem to differ in their particle size. As can be seen, the XRD peaks of the FAU-type material are relatively broad indicating that the product consists of very small crystallites (Fig. 1A). In contrast, the peaks of the LTA-type zeolite do not suggest very small particle size (Fig. 1B). Both systems were subjected to a detailed study in order to reveal the crystallization mechanism, which controls the formation of the two zeolites. The nanoscale events leading to the transformation of the amorphous precursors into zeolite X and A were followed by means of HRTEM.

Our previous investigation [28] showed that the gel yielding zeolite X had a grain-like structure (Fig. 2A). The grain-like appearance of the gel phase was due to the presence of

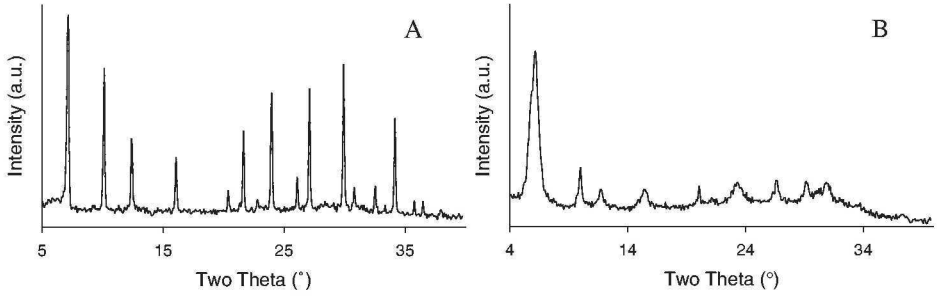

Fig. 1. XRD patterns of zeolite X (A) and A (B) synthesized at RT for 21 and 3 days, respectively.

brighter, relatively isometric areas, which were almost homogeneously distributed within the volume of the gel particles (Fig. 2B). Based on EDS analysis and contrast differences, these areas in the gel phase were attributed to silica-rich liquid inclusions trapped within the amorphous mass (Fig. 2B). The faceted shape of these structures observed in the TEM images at high magnification (not shown) suggests the presence of ordered structure at the interface dense gel/liquid inclusion. The bright areas in the gel phase were denoted as "negative crystals" [28], which is a term employed to describe faceted cavities inside solid materials or crystal filled with mother medium, which could be in the form of solution or gas [29].

The structure of the zeolite A precursor was somewhat different, namely the gel grain-like appearance characteristic for zeolite X was not observed (Fig. 2C). Careful inspection of the gel confirmed that the initial gel phase was relatively uniform and did not contain areas with different contrast (Fig. 2D). Such areas appeared after 6 h of RT synthesis. Their number gradually increased during the induction period and after 29 h all gel particles contained such spots. Besides the number, the structures of these areas changed with the

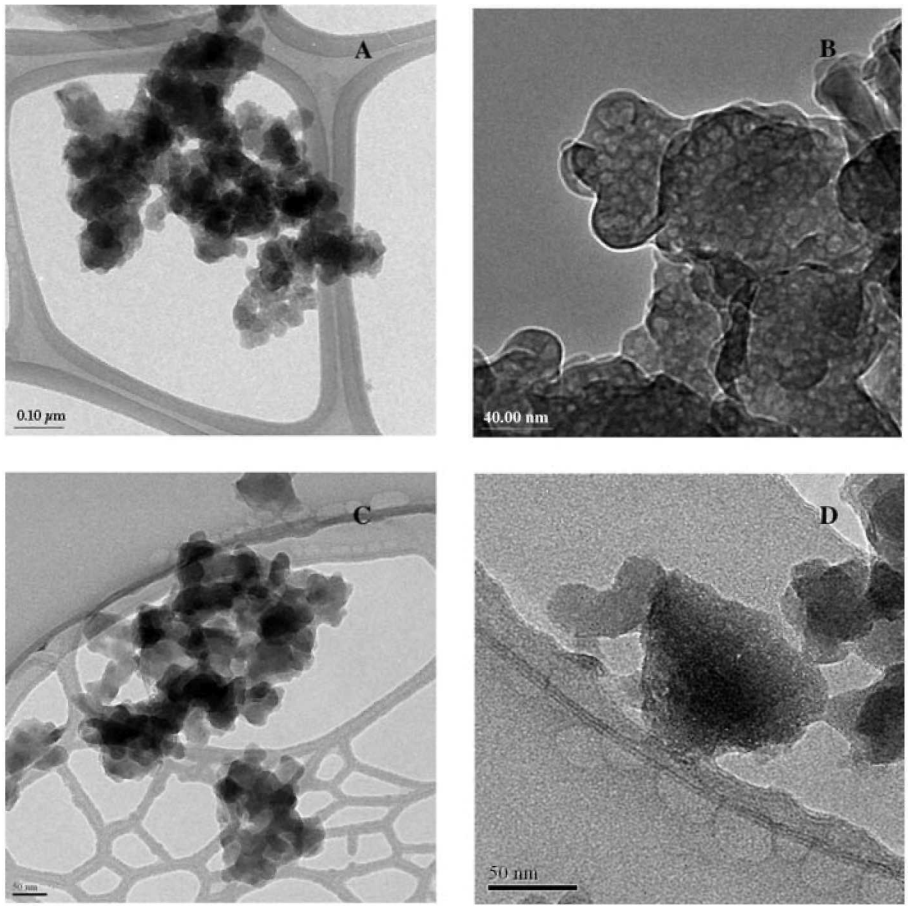

Fig. 2. TEM micrographs showing the structure of the gel material after 90 min mixing of the reactants: (A, B) zeolite X and (C, D) zeolite A precursors.

crystallization time. The round shape was typical for the bright spots at the beginning of the induction period, while at the end of the process these spots contained straight edges suggesting some level of organisation in these areas. This evolution is obviously a part of the gel transformation, which precedes the onset of the crystallization. Hence, the "negative crystals" observed in the solid amorphous precursors are related with the process of nucleation. Something more, the fact that their structure changes along the induction period suggests that important processes take place in these areas. These findings make us think that the "negative crystals", in particular at the interface solid/liquid, are most likely the places for zeolite nucleation.

It is somewhat strange, however, that the negative crystals were observed in the gel yielding zeolite X just after 90 min of mixing of the reactants, whereas these structures appeared during the long induction period in the case of zeolite A. These differences in the evolution of the systems suggest different mechanisms of formation or at least different duration of the crystallization events. Indeed, the combined TEM/synchrotron XRD analysis at the initial stage of crystallization revealed that zeolite nuclei were formed during the homogenization (90 min) of the initial reactants [28]. The zeolite A yielding system, was carefully inspected by means of HRTEM supported by XRD and SAXS analyses and no evidences for any nuclei were found. Obviously, the nucleation takes place during the long induction period and the first crystalline particles were detected both by XRD and HRTEM after about 40 h of RT synthesis. Therefore, the time interval when the "negative crystals" and the zeolite nuclei appeared match well, which is another proof that these events are related.

The evolution of the zeolite A yielding system includes the following main stages. After the homogenization of the reactants, a gel composed of aggregates with globular form was obtained (Fig. 2C and D). These aggregates maintained their form all over the induction period. After 44 h of RT synthesis the structure of the gel changed, i.e., became more open and angular particles could be observed. Together with the amorphous zeolite A precursor particles, crystallites with a size of 10-15 nm were detected in the lattice images with a d-spacing of 12 Å. The presence of X-ray crystalline LTA-type material at this stage was confirmed by XRD. Samples taken after 52, 67 and 73 h of RT synthesis showed continuing reorganization of the solid and decreasing of the amount of the material with amorphous appearance. The material synthesized for 73 h contained mainly single crystals with sizes between 100 and 400 nm. Limited number of aggregates built of smaller zeolite crystal was also observed.

Further, the morphology and interface of the zeolite A precursor gel and the samples obtained after 1, 2, 3 and 4 days of treatment were characterized by SAXS. For all samples, the scattering curves present a similar feature in two parts, where the slow decrease of the scattering intensity is followed by a marked decrease (Fig. 3). The linear slopes obtained for the first decrease were similar for all the samples (around –2). The value of the second slope varies from –3.3 for the initial gel to –4 for the sample synthesized for 4 days. The values of the slope at high q values (Porod domain) are indicative of the surface roughness of the particles. The particles obtained after one and two days had rough surfaces, while those synthesized for 3 and 4 days were smooth. This behaviour is confirmed by plotting the $I(q)*q^4$ data as a function of q. Fig. 4 shows the scattering curves in the Porod domain plotted under the form $I(q)*q^4$ vs. q. The curves corresponding to 3 and 4 days treated samples exhibited oscillations in the intensity around the Porod law, whereas the curve corresponding to the sample treated for 2 days did not show such oscillations. The oscillations clearly indicate that thes particles are well-defined in size and shape. In contrast, for the samples treated for less